Institut für Geodäsie und Geoinformation

VLBI observations
of the Chang'E-3 lunar lander

Dissertation

zur

Erlangung des akademischen Grades

Doktor der Ingenieurwissenschaften (Dr.–Ing.)

der

Landwirtschaftlichen Fakultät

der

Rheinischen Friedrich–Wilhelms–Universität Bonn

vorgelegt von

M.Sc. Zhongkai Zhang

aus Jilin, Volksrepublik China

Bonn 2019

Summary

This thesis deals with the concept and the analysis of geodetic VLBI observations of the Chang'E-3 lunar lander. VLBI as a high accuracy measuring technique, is widely used in geodesy, astrometry and deep space explorations. In recent years, tracking artificial sources with geodetic VLBI has gained more and more importance. However, the actual state of the art is only at the starting stage of a full establishment. With the development of the VLBI Geodetic Observing System (VGOS), tracking artificial sources with VLBI will be an important aspect of future geodetic VLBI activities. Consequently, research and development in this area are desired in the community.

The Chang'E-3 lunar lander is equipped with an X-band transmitter enabling VLBI observations of the Moon from Earth. In a project called *Observing the Chang'E-3 Lunar Lander with VLBI* (OCEL), the lunar lander was observed with global VLBI radio telescopes of the International VLBI Service for Geodesy and Astrometry (IVS). It opened a new window for applying geodetic VLBI to artificial radio sources. The main task of the OCEL study is separated in two parts, the determination of the group delays of the lunar lander observations and the position estimation of the lunar lander.

Starting the geodetic VLBI processing workflow with the determination of the group delays, investigations have been carried out to process Differential One-way Ranging (DOR) tones with an improved fringe fitting scheme. With these investigations, a complete chain of processing of the VLBI data for the OCEL sessions with proper methods were newly developed. The performance is assessed by triangle closure delay analysis as a main criterion. Thus, group delays of VLBI observations of DOR tones can now be obtained routinely which is the first achievement of this thesis.

The second part is the estimation of the position of the lunar lander with these group delays. New is that a near-field model was designed for VLBI delays of observations of the lunar lander and that the corresponding partial derivatives were derived and implemented. Compared with the most up-to-date near field model, the performance of our model is consistent at the picosecond level for the lunar lander. The position estimated with a constraint of the radial component is about 10 meters different from the values determined by the photogrammetric Lunar Reconnaissance Orbiter (LRO) mission. The results of the current study in terms of achieved accuracy are compatible with those of other recent results related the position of the Chang'E-3 lunar lander with VLBI. Besides that, due to the contribution coming from the globally distributed IVS network, respectively the long observing arc and delay referencing calibrations, the OCEL results show a better performance in terms of uncertainties compared to short-duration VLBI and VLBI plus range and range rate from Doppler measurements with a network of a few regional stations.

In 2018, a second beacon on the lander was switched on for a few hours and the lunar lander was observed again with the Chinese deep space network in same-beam VLBI mode. In a preliminary investigation, we used a number of these VLBI observations on the Jiamusi-Kashi baseline to estimate the relative position of the two antennas on the lunar lander. Differential phase delays were used as observables. The geometric delay model and the corresponding partial derivatives were derived and applied using the near field model developed for OCEL. The estimated relative position vector differs from the a priori vector by about 0.02 to 0.04 m. In addition, the relative angles (polar angle and azimuth angle) in a Moon-fixed system PA between the two antennas on the Chang'E-3 lunar lander are estimated. The accuracy achieved is compatible with the relative positioning between the lunar lander and the rover.

The experiences gained and results obtained from VLBI observations of the OCEL project and of the same-beam VLBI session reveal the potential of VLBI for observing artificial targets. In the meantime, the tools developed here were already applied in further lunar target positioning, lunar motion monitoring and lunar reference frame realization with VLBI.

Zusammenfassung

Diese Dissertation beschäftigt sich mit dem Konzept und der Analyse geodätischer VLBI-Beobachtungen des Chang'E-3-Mondlanders. VLBI ist eine hochpräzise Messtechnik, die in der Geodäsie, Astrometrie und bei Weltraumerkundungen weit verbreitet ist. In den letzten Jahren hat die Beobachtung künstlicher Quellen mit geodätischen VLBI immer mehr an Bedeutung gewonnen. Der aktuelle Stand der Technik befindet sich jedoch erst in der Anfangsphase einer vollständigen Etablierung. Mit der Entwicklung des VLBI Geodetic Observing System (VGOS) wird die Beobachtung künstlicher Quellen mit VLBI ein wichtiger Aspekt zukünftiger geodätischer VLBI-Aktivitäten sein. Folglich sind Forschung und Entwicklung in diesem Bereich in der Gemeinde erwünscht.

Das Chang'E-3-Mondlandegerät ist mit einem X-Band-Sender ausgestattet, der die VLBI-Beobachtungen des Mondes von der Erde aus ermöglicht. In einem Projekt namens Öbserving the Chang'E-3 Lunar Landermit VLBI (OCEL) wurde der Mondlander mit globalen VLBI-Radioteleskopen des Internationalen VLBI-Dienstes für Geodäsie und Astrometrie (IVS) beobachtet. Es öffnete sich eine neue Möglichkeit für die Anwendung der geodätischen VLBI mittels künstlicher Funkquellen. Die Hauptaufgabe der OCEL-Studie besteht aus zwei Teilen: der Bestimmung der Gruppenlaufzeitverzögerungen der Mondlander-Beobachtungen und der Positionsschätzung des Mondlanders. Ausgehend vom geodätischen VLBI-Verarbeitungsworkflow mit der Ermittlung der Gruppenlaufzeitverzögerungen wurden Untersuchungen durchgeführt, um DOR-Töne (Differential One-Way Ranging) mit einem verbesserten Randanpassungsschema zu verarbeiten. Mit diesen Untersuchungen wurde eine vollständige Kette der Verarbeitung der VLBI-Daten für die OCEL-Sessionen mit geeigneten Methoden neu entwickelt. Die Leistung wird durch eine Dreiecksschlussanalyse der laufzeitdifferenzen als Hauptkriterium bewertet. Somit können Gruppenlaufzeitverzögerungen von VLBI-Beobachtungen von DOR-Tönen routinemäßig erhalten werden, was die erste Hauptkomponente dieser Dissertation ist.

Der zweite Teil ist die Schätzung der Position des Mondlanders mit diesen Gruppenverzögerungen. Neu ist, dass ein Nahfeldmodell für VLBI-Beobachtungsverzögerungen des Mondlanders entwickelt und die entsprechenden partiellen Ableitungen abgeleitet und implementiert wurden. Ein Vergleich mit dem aktuellsten Nahfeldmodell liefert für unser Modell für den Mondlander eine Übereinstimmung im Pikosekundenbereich. Die mit einer Bedingungsgleichung für die Radialkomponente geschätzte Position unterscheidet sich um etwa 10 Meter von den durch die LRO-Mission (Photogrammetric Lunar Reconnaissance Orbiter) ermittelten Werten. Die Ergebnisse der aktuellen Studie hinsichtlich der erreichten Genauigkeit sind mit denen anderer neuerer Ergebnisse in Bezug auf die Position des Chang'E-3-Mondlanders mit VLBI vergleichbar. Darüber hinaus zeigen die OCEL-Ergebnisse aufgrund des Beitrags des weltweit verteilten IVS-Netzwerks bzw. der Kalibrierungen in Bezug auf die langen Beobachtungsbögen eine bessere Stabilität verglichen mit kurzzeitigen VLBI-Beobachtungen eines Netzwerks einiger regionaler Stationen, die noch mit Entfernungsmessungen und Messungen der Entfernungsrate aus Dopplermessungen ergänzt wurden.

Im Jahr 2018 wurde für einige Stunden ein zweiter Senderer am Lander eingeschaltet und der Mondlander erneut mit dem chinesischen Weltraumnetz im VLBI-Modus im sog. Same-Beam-Modus beobachtet. In einer vorläufigen untersuchung haben wir eine Reihe dieser VLBI-Beobachtungen an der Jiamusi-Kashi-Basislinie, mit dem Ziel verwendet, die relative Position der beiden Antennen auf dem Mondlander zu schätzen. Als Observable wurden differentielle Phasenverzögerungen verwendet. Das geometrische Verzögerungsmodell und die entsprechenden partiellen Ableitungen wurden abgeleitet und unter Verwendung des für OCEL entwickelten Nahfeldmodells angewendet. Die geschätzte relative Vektor der Position unterscheidet sich von der a priori-Entfernung um 0.02 zu 0.04 m. Die erreichte Genauigkeit ist mit der relativen Position zwischen dem Mondlander und dem Rover kompatibel.

Die Erfahrungen und Ergebnisse der VLBI-Beobachtungen des OCEL-Projekts und der VLBI-Sessionen im Same-Beam-Modus zeigen das Potenzial der VLBI für die Beobachtung künstlicher Ziele. In der Zwischenzeit wurden die hier entwickelten Tools bereits in einer weiteren Mondpositionsbestimmung für die Mondbewegungsüberwachung und für die Mondreferenzrahmenrealisierung mit VLBI eingesetzt.

Contents

1. Introduction

1.1   Motivation

As a geometric technique, geodetic VLBI measures the time difference of the arrival of a radio wavefront emitted by a distant quasar at two Earth-based radio telescopes. The technique is used to precisely determine a) the directions to compact extra-galactic radio sources such as quasars realizing the International Celestial Reference Frame (ICRF), b) the coordinates of the radio telescopes determining a reference frame on Earth such as the International Terrestrial Reference Frame (ITRF), and c) the Earth orientation parameters (EOP) reflecting the instantaneous orientation between the two reference frames. For some time, radio telescopes are also widely used by space agencies in deep space explorations, e.g., for tracking artificial spacecraft. Typically, in spacecraft tracking, the VLBI technique is applied in a special setup with only a few baselines formed by deep space stations, and the observing sessions are scheduled in short periods with intensive observations, e.g., one observation each second over a few hours. In recent years, tracking artificial sources in a genuine geodetic VLBI mode has become of greater interest in the geodetic research community. However, the actual state of the art is only at the starting stage of a full establishment. With the development of the VLBI Global Observing System (VGOS), tracking artificial sources with VLBI maybe become a more important part of geodetic VLBI. Consequently, research and development in this area are desired in the community. The current prime issues in this area are to routinely apply the VLBI technique to observations of artificial targets and achieve potential scientific goals in this way.

As the only natural permanent satellite of the Earth, the Moon is a prime object for deep space study and it is explored with numerous deep space missions. The Chang'E-3 lunar lander, which is equipped with X-band transmitters, was deployed on the Moon in December 2013 enabling VLBI observations of the Moon represented by the transmitter antenna. In a project called *Observing the Chang'E-3 Lunar Lander with VLBI* (OCEL), the Moon was observed with globally distributed VLBI stations of the International VLBI Service for Geodesy and Astrometry (IVS) for periods of up to 24 hours in each session. This opened a new window of research on geodetic VLBI with artificial signal sources. A complete chain of processing and analysis of the VLBI observations of the Chang'E-3 lunar lander, as developed in this thesis, will provide the basis for further such missions and other related projects. Since the lunar lander is fixed on the Moon, the estimation of the position of the Chang'E-3 lunar lander with VLBI also has the potential and capability for further investigations on the movements of the Moon in space.

In addition, for the purpose of achieving the best possible accuracy, typically the differential VLBI method is applied, where a quasar nearby the artificial target (in an angular sense) is observed for calibrations. Through the differential approach, common errors along the similar signal paths can be eliminated. A special case is same-beam interferometry (SBI), where two radio sources are so close to each other that they appear in the beam together and can be observed simultaneously with a single pointing. With this technique, an even higher accuracy for the relative position of the two targets can be obtained. By applying the SBI technique on the transmitter antennas of the Chang'E-3 lunar lander and of the lunar rover, but also to two transmitters on the lander, the relative positions of the two targets were obtained, and used for further investigations. This relative distance monitoring of the two artificial targets with SBI within a short period is of great importance for any lunar or planetary landing mission with more than one transmitter. Considering that further artificial spacecraft are deployed on the Moon nearby, the relative positions of these spacecraft can be used for investigations of the movements and structure of the Moon.

1.2   Previous Investigations

In 1970s, VLBI as a radio measuring technique, was used in deep space explorations, e.g., in Apollo projects to determine the motion tracks of Apollo 16 and 17 on the lunar surface [Salzberg, 1973]. In the Apollo

16 mission, the motion track of the lunar rover was determined by phase variations from differential VLBI observations, with which the final results of the rover position was within 30 meters of the a priori position, corresponding to 15 mas (milliarcseconds) angular resolution [Salzberg, 1973]. From the analysis it turned out that equipment instabilities lead to most of the uncertainties. It was, therefore, suggested to apply differential VLBI to determine the relative positions, lunar libration, etc.. The relative distance between the Apollo 12 and Apollo 14 sites was then determined by differential VLBI and main errors were supposed to be the atmosphere, terrestrial sites coordinates, and the lunar libration model [Counselman et al., 1973].

With the Apollo program, the Apollo Lunar Surface Experiments Package (ALSEP) [Perkins, 1973] was carried to the Moon which comprised a set of scientific instruments placed at the landing sites including S band (2.3 GHz) transmitters for each of the 5 ALSEP sites [King Jr, 1975; Counselman III, 1975; Bates et al., 1979]. The analysis of the differential ALSEP phases by the Massachusetts Institute of Technology (MIT) group yielded the relative ALSEP positions and physical librations from over 16 months of observations making use of 6 radio telescopes [King Jr, 1975]. The uncertainties were less than 0.005" of geocentric arc which is about 9.2 m on the surface of the Moon [King Jr, 1975]. Combined with Lunar Laser Ranging (LLR) [Chapront & Francou, 2006] data, the uncertainties in the relative coordinates of the 5 ALSEP transmitters were 30 meters in the radial coordinates and 10 meters in the two transverse coordinates [King Jr, 1975]. Values determined for the libration parameters have uncertainties smaller than the uncertainties obtained only with LLR. A program of differential ALSEP-Quasar VLBI observations was planned and carried out around 1977 at the NASA Jet Propulsion Laboratory. The general scientific goals of the ALSEP-Quasar program were to obtain high accuracy observations to tie the lunar ephemeris to the inertial reference frame of extra-galactic radio sources, to test gravitational theories, and to measure the Earth-Moon tidal friction interaction. However, soon afterwards, on September 30, 1977, the ALSEP operations ended with the termination of support [Slade et al., 1977].

In the late 70s of the 20th century, Delta Differential One-way Ranging (delta-DOR or ΔDOR), was used in the Voyager-1 and -2 deep space exploration missions [Smith et al., 1979; Brown et al., 1980; Border et al., 1982; Hildebrand et al., 1982]. In 1990 and 1991, the spacecraft Magellan and the Pioneer 12 orbiter were observed with the Same Beam Interferometry (SBI) technique, and 34 hours of observations were obtained. Combined with Doppler data, the SBI observations produced final orbit results which were better than only using Doppler and differential Doppler data [Folkner et al., 1992a,b, 1993]. In 1998, the Mars Climate Orbiter (MCO) experienced a loss of control due to large tracking errors caused by the lack of delta-DOR information [Lloyd & Writer, 1999; Oberg, 1999; Sauser et al., 2009]. Since then, the delta-DOR technique has been in use as a standard tracking technique besides range and range rate. In follow-on Mars exploration missions, including Odyssey [Christophe et al., 2009], Spirit (MER-A) [Portock et al., 2004; Potts et al., 2004], Opportunity (MER-B) [Martín-Mur et al., 2006; Lanyi et al., 2005], Mars Reconnaissance Orbiter [Shambayati et al., 2006; You et al., 2007], delta-DOR was widely used for tracking.

Japanese colleagues also used VLBI to determine the orbits of the Mars exploration spacecraft Nozomi [Kikuchi et al., 2004]. In 2007, the Selenological and Engineering Explorer (SELENE) was launched [Liu et al., 2006, 2007]. SBI observations of the Japanese VLBI network were used to track the two satellites of SELENE, R-star and V-star. With the high precision differential delays obtained, the accuracy of the estimated orbit parameters had an uncertainty of up to 10 m. At the same time, a more accurate lunar gravitational field model was derived from these data [Goossens et al., 2011].

In 2006, the European Space Agency (ESA) used the delta-DOR technique to track the spacecraft of the Venus Express mission [Svedhem et al., 2007]. Here, the resulting height of the orbit-insertion point of Venus Express was only about 3 km higher than the anticipated value of 386 km [Maddè et al., 2006] confirming the height of Venus' atmosphere.

In 2007, Chang'E-1 was launched as the first Chinese lunar exploration spacecraft [Ouyang et al., 2010]. In 2009, the differential VLBI technique was used for observations of the Chinese VLBI Network (CVN) tracking Chang'E-1. The RMS (Root Mean Squared) error of the time delays was 3.5 ns (nanoseconds) and an orbit determination accuracy of about 100 m was achieved [Jianguo et al., 2010]. In 2010, Chang'E-2 was launched successfully, travelled close to the Earth-Moon Lagrange L2 points in 2011, and flew even further up to 7 million km away from the Earth in 2012 [Huang et al., 2013]. Besides differential VLBI, a tracking

test with X-band delta-DOR was performed and group delays with an RMS error at the 1 ns level were obtained [Li et al., 2012; LI et al., 2011].

Chang'E-3 is an unmanned lunar exploration mission operated by the China National Space Administration (CNSA), incorporating a robotic lander and China's first lunar rover [Ip et al., 2014; Li et al., 2015]. It was launched in December 2013 as part of the second phase of the Chinese Lunar Exploration Program (CLEP) [Zheng et al., 2008]. Chang'E-3 reached lunar orbit on December 6, 2013 and landed on December 14, 2013 [Sun et al., 2013; Xiao, 2014] becoming the first spacecraft to soft-land on the Moon since the Soviet Union's Luna 24 in 1976 [Pieters et al., 1976]. The deployment of the Chang'E-3 lander on the Moon and its capability to transmit weak DOR tone signals opened up the window for a new era of lunar observations from Earth. With an initial VLBI observing session of one hour duration on December 14, 2013 with 4 radio telescopes carrying out unified X-band (UXB) observations (including range and range rate from Doppler measurements) and with two-hour UXB observations of 3 telescopes on December 17, 2013, the position of the Chang'E-3 lander was estimated at the Beijing Aerospace Control Center (BACC) [Cao et al., 2016]. Compared with positioning results of NASA Goddard Space Flight Center (GSFC) employing observations of the Lunar Reconnaissance Orbiter (LRO) [Vondrak et al., 2010; Zhao et al., 2014], the differences in a Mean Earth System are about 2.4 meters in altitude, and 0.002° (7.2 arcseconds) in latitude and longitude which is about 85 meters on the surface of the Moon.

During 2014 to 2016, twelve so-called OCEL (*Observing the Chang'E-3 Lunar Lander with VLBI*) sessions were conducted. Haas et al. [2016] reported on a preliminary status of the research and development in project OCEL with basic information of the observing sessions including signal characteristics, scheduling strategies, frequencies setups, etc.. Various approaches of frequency setups were tested during the different OCEL sessions. Following the experience within the observing series, the most suitable frequency setup was developed and used in the last two OCEL sessions. In the same publication, the algorithms, models and methods for processing the data of OCEL as available at that time based on the classic geodetic VLBI mode were discussed Haas et al. [2016]. The correlation of the lunar lander observations was done with the standard software correlator in geodetic VLBI. The necessary a priori delays were computed with (at that time) state-of-the-art near-field delay models. Due to the special signal structure of the Chang'E-3 lunar lander and to deal with the DOR tones properly, several fringe-fitting software packages were used for tests. Despite that optimizations and modifications are still necessary, a preliminary chain of processing the data in OCEL was developed in Haas et al. [2016], which presents a clear structure of OCEL and the clues for the further investigations.

Cao et al. [2016] and Li et al. [2016] used a number of hours of VLBI observations of the Chang'E-3 lunar lander by the Chinese VLBI Network together with Unified X-band (UXB) range and range rate observations to determine the position of the lunar lander. The results were ten to several tens of meters away from the values of LRO.

In Klopotek et al. [2019], besides the lunar lander observations and delay-referencing quasar observations, the geodetic quasar observations observed during the gaps between the blocks of the lunar observations were also used. These observations were used to determine (a priori) the calibrations for clock variations and troposphere corrections. With this analysis strategy, two OCEL sessions (OCEL-08 and OCEL-09, which were identified as the best-performing among the twelve OCEL sessions in Klopotek et al. [2017]) were analyzed. The estimation results differ from the results from LRO by about 6 m.

1.3   New Developments and Outline

The goal of the thesis is to analyze the VLBI observations of the Chang'E-3 Lunar Lander and then to estimate its position on the Moon as well as the relative positions of the two transmitters on the lander. In this thesis, new developments are :

First, an efficient chain of processing has been developed and set up to determine the group delays from VLBI raw data of the Chang'E-3 lunar lander emitted as DOR tones. This ensures suitability and the best possible accuracy of the group delays serving as the input for the subsequent data analysis.

After that, a VLBI time delay model for the near field target has been developed and the corresponding partial derivatives have been derived. The model and the partial derivatives have been used in a newly written software program optimized for dealing with VLBI observations of the Chang'E-3 lunar lander. All geophysical modeling is according to the IERS Conventions 2010 [Petit & Luzum, 2010]. The estimation of the position of the lunar lander with constrained least-squares adjustment was implemented. Thus, with the group delays of the Chang'E-3 lunar lander in OCEL as input, the program produces estimation of the position of the lunar lander.

At last, a model for the observations of the SBI technique for the two transmitter antennas of the Chang'E-3 lunar lander has been developed and the corresponding partial derivatives have been derived and implemented. With several hours of phase delays of the two transmitter antennas on the Chang'E-3 lunar lander on a single baseline, the relative positions of the transmitter antennas have been estimated. A method for relative distance monitoring was applied.

The outline of the thesis is as follows:

- In Chapter 2, the basic principles and definitions of time scales are introduced. The coordinates frames used to measure the stations and targets motions are described.

- In Chapter 3, the basic principles of geodetic VLBI and delta-DOR are introduced.

- Chapter 4 is related to the group delay determination, containing the algorithms and software parts used in correlation and fringe-fitting.

- On the basis of the previous studies a new near-field VLBI time delay model is developed in Chapter 5.

- In Chapter 6, the characteristics of OCEL sessions are described.

- In Chapter 7, with the observations from OCEL, analysis about fringe-fitting are comprehensively and accurately performed for a reliable strategy of fringe-fitting the OCEL sessions.

- In Chapter 8, the position estimation of the Chang'E-3 lunar lander is performed and discussed in view of the OCEL observations.

- In Chapter 9, the relative position of two antennas on the Chang'E-3 lunar lander is estimated.

- SBI, as a special case of VLBI, is discussed contrasted with VLBI in Chapter 10.

- The conclusions of all investigations are given in Chapter 11 together with an outlook for further studies.

2. Theoretical Components

To describe objects or events in space and time with coordinate and time system, four coordinates are required, three for identifying the position in space, the fourth providing time. In classic Newtonian mechanics, time is absolute and independent from the three coordinates in space, but not in relativity, which should be considered to achieve necessary level of accuracy. The computation of the observables in VLBI requires the time and coordinate information of the target and stations. There are a number of different time scales and coordinate systems involved in VLBI. In this Chapter, introductions of the time scales (Sec. 2.1) and coordinate systems (Sec. 2.2) used in VLBI are given. For time scales, the definitions and relationships are described. In terms of coordinate systems, besides the respective theoretical definitions and the practical transformations between ICRS and ITRS, in particular, these information about the lunar reference systems (Sec. 2.2.4) and ephemeris are given.

2.1 Time Scales

In Geodetic VLBI, a number of time scales are involved in all parts: scheduling, observing, correlation, fringe-fitting, post analysis. Typically, time is used in two ways, one is as an epoch and the other is for a duration. For different events, different time scales may have to be used. The relevant time scales are introduced as follows. The links between these time scales are depicted in Fig. 2.1.
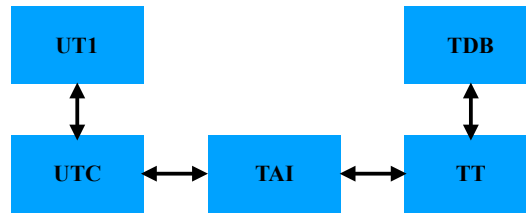

Figure 2.1: Block diagram of transformation between time scales.

2.1.1 Universal Time

Earth rotation is a continuous periodic and aperiodic movement, on which the time scales of Universal Time (UT) are based. It is a modern continuation of Greenwich Mean Time (GMT), i.e., the mean solar time on the Prime Meridian at Greenwich, London, UK.

UT1 is the principal form of Universal Time. It is proportional to the rotation angle of the Earth with respect to distant quasars, specifically, the International Celestial Reference Frame (ICRF), neglecting some small adjustments. The observations allow the determination of a measure of the Earth's angle with respect to the ICRF, called the Earth Rotation Angle (ERA, which serves as a modern replacement for Greenwich Mean Sidereal Time). UT1 is required to follow the relationship [Standish et al., 1992]

$$
\begin{aligned}
\text{ERA} &= 2\pi \left(0.7790572732640 + 1.00273781191135448 \cdot \text{Tu}\right) \quad \text{[radians]} \\
\text{where Tu} &= \text{ Julian UT1 date } - 2451545.0
\end{aligned}
$$

(2.1)

2.1.2   Coordinated Universal Time

UTC (Universal Time Coordinated) is an atomic timescale that approximates UT1. It is the international standard on which civil time is based. It ticks with SI seconds, in step with TAI. It usually has 86,400 SI (International System of Units) seconds per day but is kept within 0.9 seconds of UT1 by the introduction of occasional integer leap seconds. As of 2016, these leaps have always been positive (the days which contained a leap second were 86,401 seconds long). Whenever a level of accuracy better than one second is not required, UTC can be used as an approximation of UT1. The difference between UT1 and UTC is known as DUT1 [Standish et al., 1992; McCarthy & Seidelmann, 2018].

2.1.3   International Atomic Time

The International Atomic Time (TAI) is measured in the unit of SI second and is defined as the duration of 9,192,631,770 periods of the radiation corresponding to the transition between the two hyperfine levels of the ground state of the cesium 133 atom [Standish et al., 1992; Moyer, 2005]. TAI is a laboratory time scale, independent of astronomical phenomena apart from having been synchronized to solar time. TAI is obtained from a worldwide system of synchronized atomic clocks. It is calculated as a weighted average of times obtained from the individual clocks, and corrections are applied for known effects. TAI is ahead of UTC by an integer number of seconds. The value of TAI minus UTC can be extracted from the International Earth Rotation and Reference Systems Service (IERS) and it is given as Eq. 2.2, in which ΔTAI is also named as leapsecond. Fig. 2.2 shows the historical value of the difference between TAI and UTC time scales since 1972.
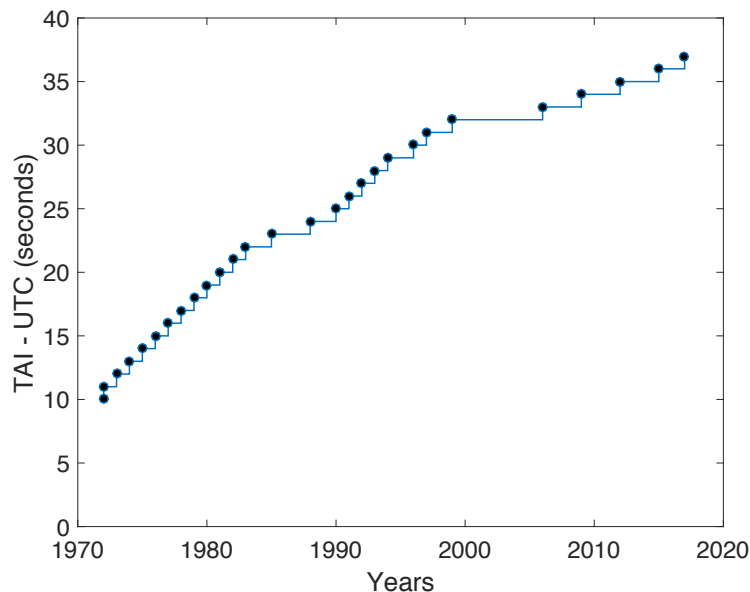
$$\Delta\text{TAI} = \text{TAI} - \text{UTC} \tag{2.2}$$

Figure 2.2: The historical value of TAI - UTC since the year of 1972.

2.1.4 Terrestrial Time

TT is the theoretical time scale for clocks at sea-level. In a modern astronomical time standard, it is defined by the IAU as a measurement time for astronomical observations made from the surface of the Earth. TT runs parallel to the atomic time scale TAI and it is ahead of TAI by a certain number of seconds which is given as 32.184 s.

$$TT - TAI = 32.184s \tag{2.3}$$

TT was formally defined by the IAU in conjunction with Geocentric Coordinate Time (TCG) on the same occasion. TCG is appropriate for theoretical studies of geocentric ephemerides and differs from TT by a constant rate with a linear transformation [McCarthy & Petit, 2004].

$$TCG - TT = L_G \times (JD - T_0) \times 86400 \tag{2.4}$$

where $L_G = 6.969290134 \times 10^{10}$, $T_0 = 2443144.5003725$, and JD is the TAI time scale in Julian days. T_0 is JD at January 1st, 00:00:00 TAI. Barycentric Coordinate Time (TCB) is the analog of TCG, used for calculations relating to the solar system beyond the Earth's orbit. TCB is defined by a different reference frame than TCG, such that they are not linearly related [Klioner, 2008]. The transformation between TCG and TCB involves a full 4-dimensional general relativity transformation as published in [McCarthy & Petit, 2004].

2.1.5 Barycentric Dynamical Time

Barycentric Dynamical Time (TDB, from the French Temps Dynamique Barycentrique) is a relativistic coordinate time scale. TT and TCG are the geocenter time scales to be used in the vicinity of the Earth, while TCB and TDB are the solar system barycentric time scales to be used for planetary ephemerides or interplanetary spacecraft navigation.

$$TCB - TDB = L_B (JD - T_0) \times 86400 - TDB_0 \tag{2.5}$$

where $T_0 = 2443144.5003725$, $L_B = 1.550519768 \times 10^{-8}$, $TDB_0 = -6.55 \times 10^5$s and JD is the TCB Julian date.
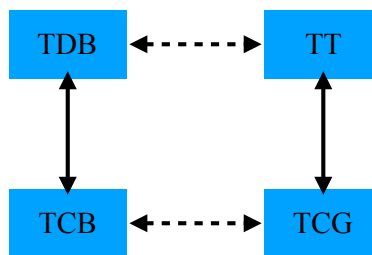

Figure 2.3: A schematic diagram of transformations between TDB, TT, TCB and TCG. The solid line stands for linear transformation and the dotted line stands for non-linear transformation.

The transformation between TT and TDB is frequently used in VLBI and deep space explorations. With the relationships between TDB, TCB, TCG and TT, the transformations can be performed with corresponding equations as in Fig. 2.3. Besides that, the difference between TT and TDB can be extracted at any time from the planetary ephemeris, in which the related equations are precisely modelled and the numerical integration has been performed. Fig. 2.4 shows a series of historical value of TT minus TDB, in which TDB stays close to TT by less than 2 ms.
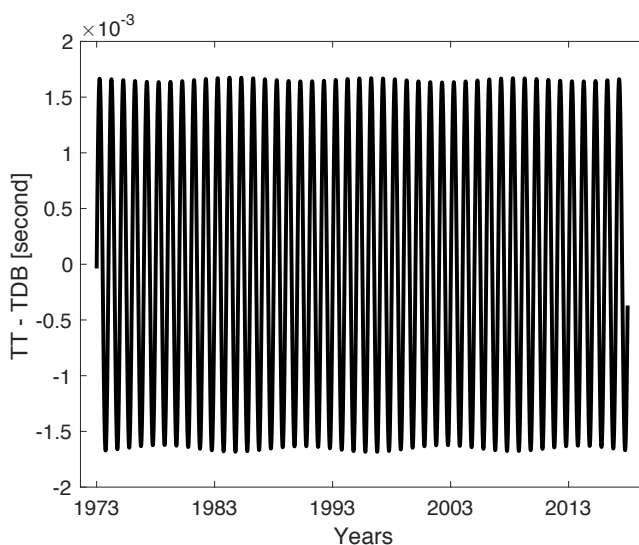
Figure 2.4: Historical values of TT - TDB since the year of 1973.

2.2   Coordinate Systems

Coordinate systems are necessary to describe the movements of objects in space with positions, velocities and trajectories. Celestial systems describe positions or directions of objects in space, terrestrial systems describe positions and velocities of objects or sites on the Earth, and dynamic systems describe positions and velocities of spacecraft cycling planets. In this subsection, the coordinate systems involved in VLBI and their transformation relationships are introduced.

2.2.1   ICRS

At its 23rd General Assembly in August 1997, the International Astronomical Union (IAU) decided that, as from 1 January 1998, the IAU celestial reference system shall be the International Celestial Reference System (ICRS). Its origin is the solar system barycenter and its axes are defined in close agreement with its predecessor, FK5 [Fricke et al., 1988] catalog of star positions and proper motions. The ICRS is realized by the International Celestial Reference Frame (ICRF), which consists of a set of precise positions of compact extragalactic radio sources. The International Earth Rotation and Reference Systems Service (IERS), created in 1988, was tasked to establish and maintain the (ICRF).

The positions of targets, which are observed by VLBI, are typically those described in the solar system barycentric coordinate system. However, if the target is a spacecraft within the solar system, the distance from the VLBI station to the target should be taken into account. Therefore, geocentric and planetocentric coordinate systems are used to express the positions of targets and stations.

2.2.2   ITRS

The International Terrestrial Reference System (ITRS) is a global spatial reference system co-rotating with the Earth in its diurnal motion in space. In particular, it defines the origin, the direction of the axes and many more conventions and parameters. The ITRS was formally adopted by the International Union of Geodesy and Geophysics (IUGG) through its Resolution 2 at its General Assembly in Perugia in 2007.

The ITRS is realized through the International Terrestrial Reference Frame (ITRF) computed by the IERS in irregular intervals. A terrestrial reference frame, such as the ITRF, provides a set of coordinates of points

located on the Earth's surface and information on its kinematics such as continental drift through annual displacement vectors. It can be used to measure plate tectonics, regional subsidence or loading and/or used to represent the Earth when measuring its rotation in space. This rotation is measured with respect to a frame tied to stellar objects, a celestial reference frame. The Earth Orientation Parameters (EOPs) connect ICRF and ITRF. The frames provide a common reference to compare observations and results from different epochs and locations.

2.2.3 Transformations

The reduction of VLBI observations of celestial targets from ground stations requires coordinates of the celestial targets and ground stations in a common reference system. As the coordinates of the celestial targets are referred to a celestial reference system and the ground stations are referred to a terrestrial reference system, the transformation between the ICRS and the ITRS is required. The transformation between the ICRS and the ITRS depends on the Earth's rotation, which can be represented by the time-dependent Earth Orientation Parameters (EOPs). In the framework of general relativity, ICRS represents a four-dimensional BCRS whereas ITRS represents a local four-dimensional geocentric system rotating with the Earth [Bretagnon & Brumberg, 2003]. For the transformation between BCRS and ITRS, it is necessary to introduce another local geocentric system with the TCG time scale as used for the ITRS and the directions of the spatial axes as for the BCRS. Therefore, the Geocentric Celestial Reference System (GCRS) is introduced by IAU Resolution B1.3 (2000). The GCRS represents a system kinematically non-rotating with respect to the BCRS and rotating dynamically with respect to the BCRS. The transformations to be used between ITRS and GCRS at the date t of the observation can be written as [Petit & Luzum, 2010]:

$$[\text{GCRS}] = Q(t)\, R(t)\, W(t)\, [\text{ITRS}] \tag{2.6}$$

where $Q(t)$, $R(t)$ and $W(t)$ are the rotation matrices arising from the motion of the celestial pole in the celestial reference system, from the rotation of the Earth around the axis associated with the pole and the from polar motion, respectively. More detailed explanations about the relevant concepts, software and IERS products corresponding to the IAU 2000 resolutions can be found in IERS Technical Note 29 [Capitaine et al., 2002].

2.2.4 Lunar Reference System

In solar system planetary computations, a planetocentric system (or planetocentric body-fixed system) is commonly used for the study of a planet, which has an origin at the center of mass of the body and in which the radius is the distance from the planetary body's center of mass to the point of interest. For the Moon, there are two slightly different reference systems commonly used to define the lunar body-fixed coordinates. One is the Principal Axis (PA) system, which is usually used in lunar gravitational studies, lunar laser ranging and other dynamics studies. The other one is the Mean Earth (ME) system, which is usually used to express the coordinates and positions for targets on the lunar surface. Both reference systems are right-handed Cartesian coordinates and have the same origin at the center of mass of the Moon. Here, the general definitions of these two systems and transformations between them are described.

2.2.5 Mean Earth Lunar Reference System

In the Mean Earth system, the mean rotational pole is used to define the z-axis. The Prime Meridian (0 degree Longitude) is defined by the mean Earth direction. The intersection of Prime Meridian and the lunar equator is at the mean sub-Earth point, which is a mean intersection of the vector from the Earth's center of mass to the Moon's center of mass and the lunar surface as shown with red color in Fig. 2.5.

2.2.6   Principal Axis Lunar Reference System

The axes of the Principal Axis system are defined by the principal axes of the Moon as shown with blue color in Fig. 2.5, which are slightly different from those of the Mean Earth system due to the fact that the Moon is not truly a synchronously rotating triaxial ellipsoid. Thus, there are small angles between the axes of ME and PA shown as *aa*, *ab* and *ac* in Fig. 2.5. The difference between these two systems is about 1 km on the lunar surface.

2.2.7   Transformations of Lunar Body-fixed Systems

As described above, the prime meridian of the Moon is the line passing from the lunar north pole through the average point on the lunar surface directly facing the Earth to the lunar south pole. In a selenographic coordinate system, the longitude gives the position east or west of the Moon's prime meridian, and the latitude gives the position north or south of the lunar equator. Both of these coordinates are given in degrees. With a certain radius and an altitude, any position on the lunar surface can be referenced by specifying two numerical values, which are comparable to the latitude and longitude of the Earth. Every point that is expressed in ellipsoidal coordinates can be expressed in Cartesian coordinates x, y, z.

Coordinates in the lunar body-fixed reference systems can be expressed in the Cartesian coordinates or lunar geodetic coordinates, between whom the transformation can be formulated as:

$$
\begin{cases}
X = (N + h)\cos\varphi\cos\lambda \\
Y = (N + h)\cos\varphi\sin\lambda \\
Z = (N(1 - f^2) + h)\sin\varphi
\end{cases}
\tag{2.7}
$$

$$
\begin{cases}
\lambda = \arctan(\frac{Y}{X}) \\
\varphi = \arccos\frac{\sqrt{X^2+Y^2}}{N+h} \\
h = \frac{\sqrt{X^2+Y^2}}{\sin\varphi} - N(1 - f^2)
\end{cases}
\tag{2.8}
$$

where

X, Y, Z : 3D Cartesian coordinates,

φ, λ, h : geodetic coordinates: latitude, longitude and ellipsoidal height, respectively,

a, b : semi-major and semi-minor axes of the ellipsoid, respectively,

f : oblateness factor,

$$
f = \frac{a - b}{a}
\tag{2.9}
$$

N : radius of curvature in the prime vertical,

$$
N = \frac{a}{\sqrt{1 - f^2\sin^2\varphi}}
\tag{2.10}
$$

Coordinates in PA and ME can be transformed into each other with the transformations being different depending on the epoch and the chosen ephemeride.

According to Folkner et al. [2008] and Williams et al. [2008], the transformations between the PA and ME systems applying the DE421 ephemeris can be expressed as:

$$
\mathbf{M} = \mathbf{R}_x(aa)\mathbf{R}_y(ab)\mathbf{R}_z(ac)\mathbf{P}
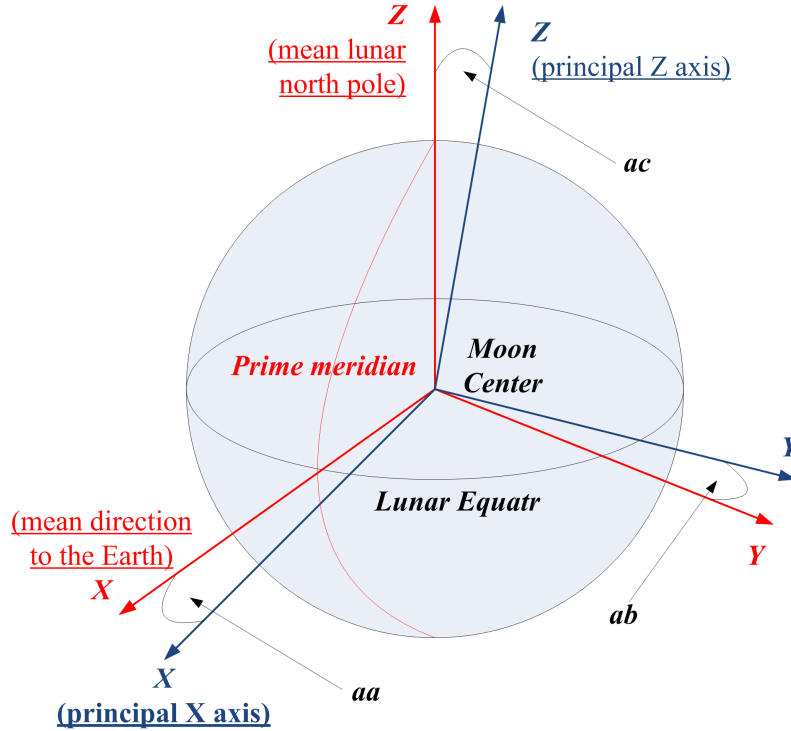\tag{2.11}
$$

Figure 2.5: The schematic diagram of the lunar fixed coordinate systems of ME and PA (not to scale).

$$\mathbf{P} = \mathbf{R}_z(-ac)\mathbf{R}_y(-ab)\mathbf{R}_x(-aa)\mathbf{M} \tag{2.12}$$

where $\mathbf{M}$ and $\mathbf{P}$ are the coordinate vectors in the ME and PA systems; aa, ab and ac as shown in Fig. 2.5 are the rotation angles. These are equal to -0.30, -78.56 and -67.92 seconds of arc, respectively, for the DE421 ephemeris.

The lunar physical librations can be described by three Euler angles that rotate from the space- to the body-fixed axes. The equations of motion for lunar Euler angles are based on the PA system and the JPL ephemerides provide the lunar libration parameters related to this system. For a target in the lunar body fixed reference system, to transform the coordinates of the target from body fixed reference system to International Celestial Reference System, the coordinates in PA system are firstly computed. Then obtain the lunar libration parameters from the ephemeris and transform to Moon-centered ICRS (or Lunar Celestial Reference System, LCRS) with formulation as:

$$\boldsymbol{r}_{PA} = \mathbf{M}_{pa2lcrs}\boldsymbol{r}_{LCRS} \tag{2.13}$$

$$\mathbf{M}_{pa2lcrs} = \mathbf{R}_z(-\varphi_l)\mathbf{R}_x(-\theta_l)\mathbf{R}_z(-\psi_l) \tag{2.14}$$

where $\boldsymbol{r}_{PA}$ and $\boldsymbol{r}_{LCRS}$ are the vectors in PA and LCRS respectively; φ_l, θ_l and ψ_l are the Euler angles obtained from ephemeris, which are defined as the inclination.

It should be noted that when we apply the transformation matrices from the GCRS (or LCRS) to BCRS, the Lorentz Transformation [Godard et al., 2012] has to be performed. Despite GCRS (or LCRS) and BCRS

both being CRSs, these systems do not just differ from each other by a geometric translation, but also by a generalized Lorentz transformation. When propagating the coordinates of a spacecraft in the BCRS, this is often convenient for numerical computations and modeling. For the targets on the Moon and the station on Earth, coordinates are described in the LCRS and GCRS, these systems are only suitable in the immediate vicinity of their centers. For convenience and practice, the calculations are usually performed in the BCRS. This requires that space-time events at a ground station on the Earth appearing in the modeling of the observables are Lorentz-transformed from the geocentric to the barycentric system and for a target on the Moon from the lunarcentric to the barycentric system.

2.3   Ephemerides

Typically, an ephemeris provides planetary positions, reference system definitions and necessary constants. The JPL Solar System Ephemeris specifies the past and future positions of the Sun, Moon, and nine planets in three-dimensional space. Many versions of this ephemeris have been produced to include improved measurements of the positions of the Moon and planets and to conform to new and improved coordinate system definitions. In this work, we use JPL ephemerides to obtain the positions of the Earth and the Moon. The lunar libration angles and positions of other planets are used in theoretical delay model calculation. There are different values of the constant angles for each JPL ephemeris because the procedures of calculating the constant rotation angles were changed several times. The comparison of the angles of DE403(same as DE405) and DE421 yield differences between them which cause displacements in the PA frame from DE421 of 5.1,-1.0 and 2.6 m in the three coordinate components. The constant rotation angles for DE421 and DE430 are close to each other. The difference in the coordinates of a point on the surface of the Moon between the ME frame and the PA frame is approximately 860 meters.

3. Very Long Baseline Interferometry

Shortly after invented, at the end of the 1970s, Very Long Baseline Interferometry (VLBI) started to be used for geodetic purposes (e.g., [Shapiro et al., 1974; Campbell & Witte, 1978]). The original principle of radio interferometry, based on a classical interferometer theory, dates back to 1890 [Michelson, 1894]. The VLBI principle is based on simultaneous observations of an radio source by two or more radio telescopes that are far apart. As distinguished from a classical radio interferometer, the telescopes receiving signals are not connected and form a very long baseline interferometer. Therefore, a precise method of timing the receiving signals is required for each of the telescopes, which is realized by highly precise atomic clocks [Vanier, 1982; Rogers et al., 1984]. With the received signal sent to a correlator for establishing coherency, the difference of the arrival times of the signal at both VLBI telescopes is determined as the primary geodetic observable [Whitney, 2000].

The International VLBI Service for Geodesy and Astrometry (IVS) [Nothnagel et al., 2017], as an international collaboration of organizations, which operate or support VLBI components, has worldwide members and form a global VLBI network, as shown in Fig. 3.1. Besides providing the ICRF, Earth orientation parameters (EOP) and its contribution to the ITRF, IVS also has the objectives to provide a service to support geodetic, geophysical, and astrometric research and operational activities and promote research and development activities in all aspects of the geodetic and astrometric VLBI technique.

In this section, the basic principle of VLBI, relevant definitions and principles are introduced.
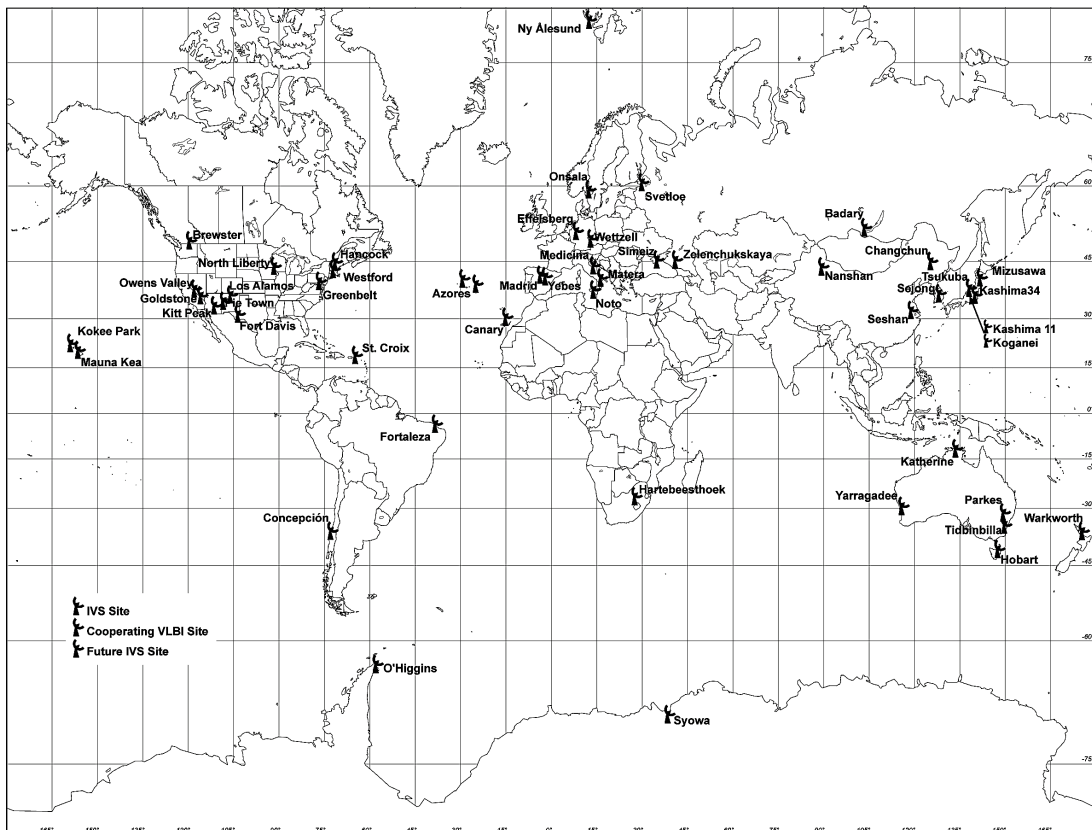

Figure 3.1: The globally distributed IVS VLBI network stations. (https://ivscc.gsfc.nasa.gov/stations/ns-map.html)

3.1 Basic Principle

An interferometer typically consists of two or more radio telescopes. A baseline represents the vector between two telescopes. As shown in the left part of Fig. 3.2, two telescopes simultaneously observe a quasar and receive the radio signals at different arrival times. The VLBI observable is the time difference of the arrival times. Since quasars are very far away, the radio signals arrive on Earth as plane wave fronts. The case shown in the right part of Fig. 3.2 is for VLBI observing a near field target, e.g. spacecraft. Since the distance to the emitter is short, the radio signal propagation is regarded as a spherical wave instead of a plane wave and the VLBI time delay model for near field targets is different to that of quasars (Sec. 5.1).
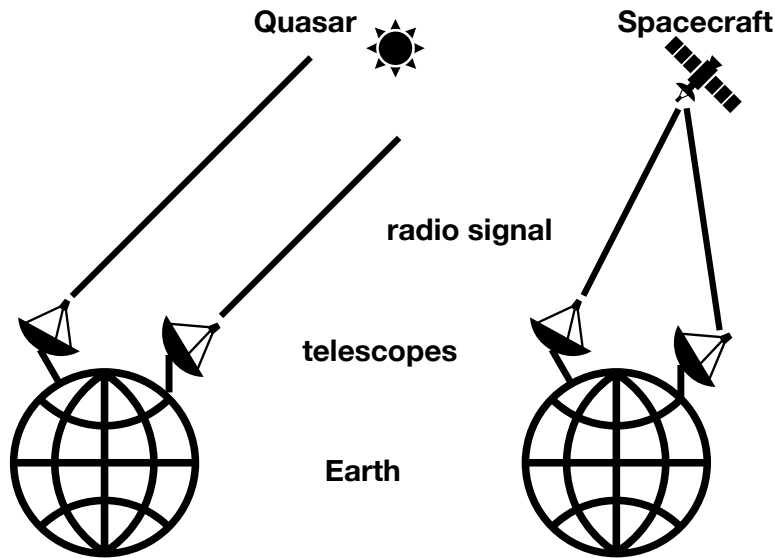

Figure 3.2: VLBI basic measuring principle.

In the following, we describe the procedures to obtain the theoretical time delay and the observed time delay.

3.1.1 Theoretical time delay

The biggest contribution in the total delay comes from the geometric delay. The geometric time delay is referred to the time difference caused by the geometric relationship of the target and the two telescopes. A simplified geometric VLBI relationship is shown in Fig. 3.3, in which we have two stations 1 and 2, the corresponding geocentric coordinate vectors are $\boldsymbol{r}_1$ and $\boldsymbol{r}_2$, and the corresponding signal receiving times are t_1 and t_2. The difference in time is the geometric time delay τ_g. According to the geometric relationship shown in Fig. 3.3, the geometric time delay can be calculated approximately as:

$$\tau_g = t_2 - t_1 = \frac{-\boldsymbol{b} \cdot \boldsymbol{k}}{c} \tag{3.1}$$

where the baseline vector is $\boldsymbol{b} = \boldsymbol{r}_2 - \boldsymbol{r}_1$, the unit vector $\boldsymbol{k}$ points in the direction of the radio source and c is the velocity of light. The unit vector pointing in the direction of the radio source $\boldsymbol{k}$ can be computed from

the right ascension α and declination δ of the source described in the CRS.

$$\boldsymbol{k} = \begin{pmatrix} \cos(\alpha) \cdot \cos(\delta) \\ \sin(\alpha) \cdot \cos(\delta) \\ \sin(\delta) \end{pmatrix} \tag{3.2}$$

The accurate calculation of the geometric delay is a complex procedure of various coordinate transformations connecting the celestial system, in which the sources are determined, with the terrestrial system of the station coordinates. The IERS Conventions [Petit & Luzum, 2010] quote a model to calculate the theoretical delay, called the Consensus model, which is the result of a dedicated workshop on the relativistic models for use in space geodesy [Eubanks, 1991]. As for our work, especially in Sec. 5.1.2, it is of importance to understand this model in detail. The vacuum delay in the barycentric frame is

$$T_2 - T_1 = -\frac{1}{c}\boldsymbol{k} \cdot (\boldsymbol{X}_2(T_2) - \boldsymbol{X}_1(T_1)) + \Delta T_{grav} \tag{3.3}$$

where T_2 and T_1 are the TCB times of arrival of a radio signal at each antenna; $\boldsymbol{X}_1$ and $\boldsymbol{X}_2$ are the barycentric radius vectors of the antennas; $\mathbf{k}$ is the unit vector from the barycenter to the source in the absence of gravitational bending; ΔT_{grav} is the differential gravitational delay [Klioner, 1991], described in details in Sec. 5.1.2.

The related transformation between barycentric and geocentric time can be used to derive another equation relating $T_2 - T_1$ and $t_2 - t_1$, and the total geocentric delay in terms of the geocentric baseline vector $\boldsymbol{b}$ is given by [Petit & Luzum, 2010]:

$$t_2 - t_1 = \frac{\Delta T_{grav} - \frac{\boldsymbol{k}\cdot\boldsymbol{b}}{c}\left[1 - \frac{(1+\gamma)U}{c^2} - \frac{|\boldsymbol{V}_\oplus|^2}{c^2} - \frac{\boldsymbol{V}_\oplus\cdot\boldsymbol{w}_2}{c^2}\right] - \frac{\boldsymbol{V}_\oplus\cdot\boldsymbol{b}}{c^2}\left(1 + \boldsymbol{k}\cdot\boldsymbol{V}_\oplus/2c\right)}{1 + \frac{\boldsymbol{k}\cdot(\boldsymbol{V}_\oplus+\boldsymbol{w}_2)}{c}} \tag{3.4}$$

where $\boldsymbol{V}_\oplus$ is the barycentric velocity of the geocenter; U stands for the gravitational potential at the geocenter; $\boldsymbol{w}_2$ is the geocentric velocity of the 2nd antenna; γ is the parameterized post-Newtonian (PPN) parameter, equal to 1 in general theory of relativity [Klioner, 1991].

Considering that VLBI observations are affected by various effects during the propagation and that variables are described in different coordinate systems, we need to add various corresponding influencing terms to the geometric time delay expression to give a complete theoretical time delay formulation:

$$\tau_t = \tau_g + \tau_{rela} + \tau_{inst} + \tau_{clc} + \tau_{trop} + \tau_{iono} + \dots \tag{3.5}$$

where

delay terms	variables
relativistic correction	τ_{rela}
instrumental correction	τ_{inst}
clock offset correction	τ_{clc}
tropospheric delay	τ_{trop}
ionospheric delay	τ_{iono}

Table 3.1: The terms affecting the VLBI time delay.

Apart from the terms list above, the station coordinate corrections, Lorentz transformations between BCRS and GCRS etc. are also involved in the computation of theoretical time delay. The general principle and theoretical time delay model of VLBI has been described by many authors. Detailed descriptions of the general principles and the various effects can be found in, e.g., Petit & Luzum [2010]. The radio signal propagates through the troposphere and ionosphere of the Earth, whose effects on the radio signal are discussed in Sec. 3.2.1 and Sec. 3.2.2.
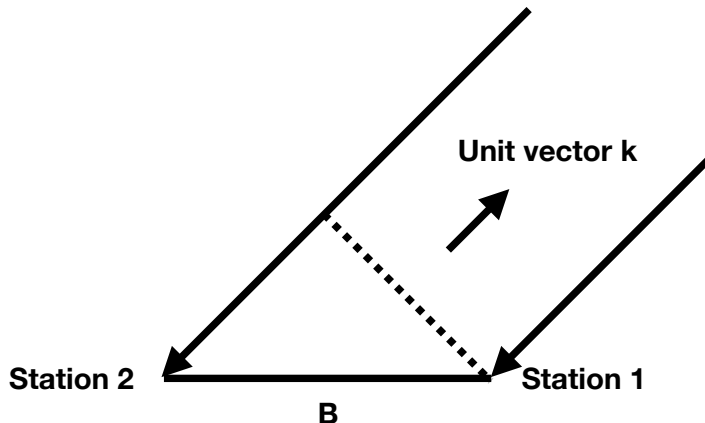
Figure 3.3: General geometric relationship of VLBI.

3.1.2 Observed Time Delay

To deduce the delay observable from the raw radio signals, a series of signal processing steps is necessary. Fig. 3.4 is a block diagram of the essential elements of a basic VLBI system. The radio signals (radio frequency, RF) impinging on the antenna and amplified by amplifiers are mixed with a local oscillator (LO) signal which is phase-locked to a frequency standard provided by an atomic clock. Then the signal is down-converted to an intermediate frequency (IF) signal which effectively decreases the transmission losses of signal propagation through the cables. The IF signal is separated into a number of channels and down-converted to baseband frequency by a baseband converter with multiple channels. The atomic clock is usually a hydrogen maser, which provides stable frequency standard and time. With the time provided by the atomic clock and the time code generator, the sampled signals are reformatted and recorded.

With these reformatted signals of two stations as input to the correlator, correlation is performed to output the visibility or cross-power spectra (amplitudes and phases across all channels). The detailed algorithm and theory of correlation can be found in [Thompson et al., 1986; Thompson, 1999; Takahashi, 2000; Nothnagel, 2019]. To obtain the time delay observables from the cross power spectra, fringe-fitting (or post-correlation) has to be performed, which is introduced and discussed in detail in Sec. 4.2. The main procedures in fringe-fitting to process the correlator output includes normalization of the correlator output, a coarse search of the peaks in the spectrum and a fine search for the final delay and delay rate.

3.2 Atmospheric Delay Model

The Earth's atmosphere consists of a number of layers that differ in properties such as composition, temperature and pressure. Usually based on altitude it can be divided (called atmospheric stratification) into five main layers, which from lowest to highest are troposphere, stratosphere, mesosphere, thermosphere and exosphere. As for the influences on radio signals, only troposphere and ionosphere affect radio propagation through refraction. The ionosphere is the part of Earth's upper atmosphere ionized by solar radiation, reaching from about 60 km to 1,000 km altitude, a region that includes the thermosphere and parts of the mesosphere and exosphere. It plays an important role in atmospheric electricity and forms the inner edge of the magnetosphere.
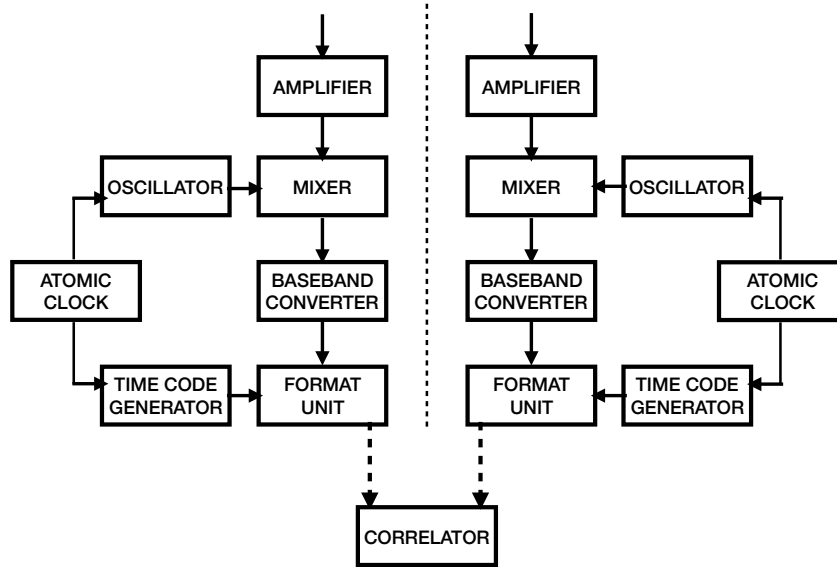
Figure 3.4: Block diagram of the essential elements of a basic VLBI system.

3.2.1   Troposphere

To build up an accurate model for the tropospheric refractive delay is one of the key problems for VLBI and other radio measurements observing from Earth and is one of the major error sources in the analysis of VLBI observations. The tropospheric delay is separated into a hydrostatic part and wet part [Davis et al., 1985; Böhm et al., 2006].

$$\Delta L(e) = \Delta L_h \cdot mf_h(e) + \Delta L_w \cdot mf_w(e) \tag{3.6}$$

where assuming the troposphere is symmetric around the sites the delay $\Delta L(e)$ at an elevation angle e is separated into a hydrostatic part (with the index of h) and a wet part (with the index of w). Each part is the product of the zenith delay (L_h, L_w) and the corresponding mapping function ($mf_h(e)$, $mf_w(e)$).

The hydrostatic zenith delay is determined from the pressure readings at the site and the station coordinates with an a priori model following standard VLBI analysis [Saastamoinen, 1973]. The wet zenith delay is usually estimated within the least-squares adjustment of VLBI analysis. The corresponding mapping functions for the hydrostatic and the wet part are determined separately by fitting related coefficients to standard atmospheres [Marini, 1972] or numerical weather models [Niell, 1996, 2000; Boehm & Schuh, 2004].

3.2.2   Ionosphere

Since the radio waves are affected by the ionosphere in a dispersive manner, VLBI observations are recorded at two frequencies, at X-band (8.4 GHz) and at S-band (2.3 GHz), to calibrate the ionospheric refraction [Lohmar, 1985; Petit et al., 1989]. With the corresponding delays τ_S and τ_X, the corrections for ionospheric refraction on the delay X-band delay can be computed with:

$$\Delta \tau_{X,ion} = \frac{f_S^2}{f_X^2 - f_S^2} \left(\tau_X - \tau_S \right) \tag{3.7}$$

where f_S and f_X are the frequencies of S-band and X-band respectively.

Ionospheric corrections can also be achieved through GPS observations, which also utilize two frequencies: L1 at 1575.42 MHz and L2 at 1227.60 MHz. A linear combination of observations at two frequencies provides an estimation of the total electron content (TEC) [Mannucci et al., 1998]. Global ionosphere maps (GIM) [Schaer, 1997] are generated on a daily basis at the Center for Orbit Determination in Europe (CODE) [Schaer, 1997] using data from about 200 GPS/GLONASS sites of the IGS and other institutions. The vertical total electron content (VTEC) is modeled in a solar-geomagnetic reference frame using a spherical harmonics expansion up to degree and order 15. Piece-wise linear functions are used for representation in the time domain. The time spacing of their vertices is 2 hours, conforming with the epochs of the VTEC maps.
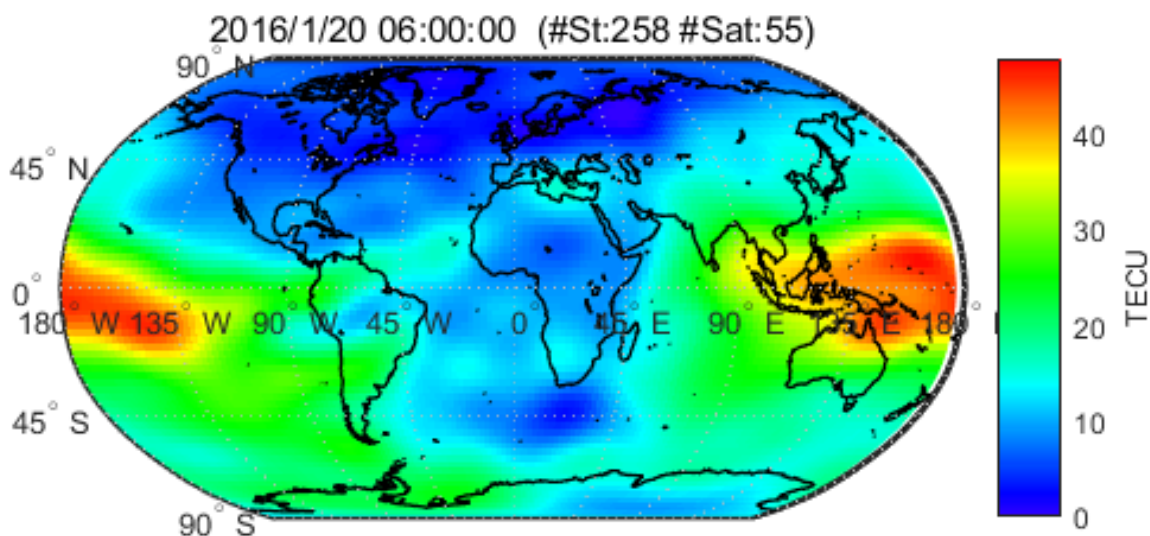

Figure 3.5: Global Tec map of Jan. 20th 2016 06:00:00.

Figure 3.5 shows the global TEC distribution plotted with GIM data from CODE at the epoch of 2016/1/20 06:00:00, in which 258 stations and 55 satellites are involved. For one station at a certain epoch, we can interpolate the GIM data in longitude, latitude and time to obtain the VTEC value.

Since the observations of the lunar lander in project OCEL were only possible at X band, the ionospheric corrections for these observations can be deduced from the TEC maps, which are available regularly. The ionosphere is modelled as a spherical layer with a certain height H, which is typically 450 km. The procedures to calculate the ionospheric delay corrections are: Firstly find the coordinates of the Ionospheric Pierce Point (IPP), at which the ray path pierce the ionospheric layer. Then do the interpolation of VTEC for the IPP from GIM. At last, with the vertical TEC value calculate the slant TEC value using the mapping function for the ionosphere [Petit & Luzum, 2010].

3.3 Least squares adjustment

In VLBI, there are usually large numbers of observations, but the unknown parameters to be determined are only a small number respectively. Thus, unknown parameters are estimated in an over-determined system of equations and the solution will not be exactly correct for each equation of the observation. Therefore, the least-squares adjustment is necessary for the estimation which provides the solution minimizing the squared sum of the residuals.

The application of least-squares adjustment in geodetic sciences dates back to Gauss, who discovered the least-squares principle in 1794 and published theory in 1809 [Gauss, 1809], translated into the English

language in [Davis, 1857]. Since Gauss devoted a significant amount of time to geodetic surveying and mapping, least-squares adjustments started to be widely used in applied geodesy [Dunnington et al., 2004]. Besides the classic applications, investigations of least-squares adjustments were conducted in the prediction of gravity, determination of satellite orbits etc. ([Kaula, 1963; Krarup, 1968, 1969; Moritz, 1970b,a, 1972; Ash, 1972]). Since the VLBI technique produces over-determined equation systems, least-squares adjustments are standard processes at all levels of VLBI data analysis [Cannon, 1978; Langley, 1980; Shapiro, 1976; Davidson, 1980].

3.4 Delta-DOR

Delta-DOR, as an interplanetary radio-tracking and navigation technique, is widely used in deep space explorations. Delta-DOR is derived from VLBI and can be used in conjunction with Doppler and ranging data to improve spacecraft navigation by more efficiently determining the spacecraft's position. A number of space missions have used Delta-DOR measurements in their orbit determination such as Mars Odyssey [Christophe et al., 2009], Mars Exploration Rovers [Oberg, 1999; Potts et al., 2004; Portock et al., 2004; You et al., 2007] and the Chang'E series [Li et al., 2015; Jianguo et al., 2010].
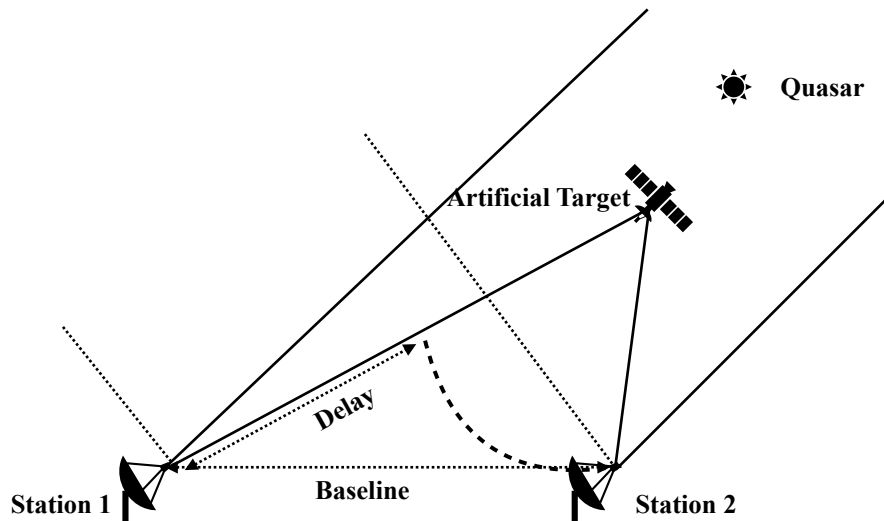

Figure 3.6: Schematic diagram of Delta-DOR observation geometry.

The name, Delta-DOR, can be divided into two parts. One is differential one-way ranging (DOR) which is defined by the fact that with only a one-way downlink signal transmitted and received at two locations, a range difference rather than an absolute range is determined [BOOK, 2013]. The basic principle of Delta-DOR is to use the differential one-way ranging technique to determine the angular position of a target relative to a reference source (or several sources) whose position is well known. This is the origin of the other part, Delta, in the name Delta-DOR. A schematic diagram of the Delta-DOR observation geometry is shown in Fig. 3.6.

Natural radio sources, such as quasars, typically emit broadband radiation with nearly flat spectrum spread over a number of gigahertz. Contrary to this, the signals of spacecraft are usually band-limited (e.g., about 40 MHz at X-band) and modulated with a number of narrow-band tones, which are utilized for VLBI (Fig. 3.7). The degree to which the spectral characteristics of the signals match each other is an important factor for using quasar sources to calibrate spacecraft targets in VLBI [Thornton & Border, 2003].

The spacecraft signal normally consists of a carrier and one or more tone frequencies modulated onto the carrier producing an upper and a lower fundamental harmonic for each modulation. In the processing and

analysis for convenience the harmonics of a tone frequency are usually just regarded as two different tones instead of being sorted as one tone frequency (in the following a DOR tone is referred to a single tone). Due to the way DOR tones are generated, they are symmetric around a carrier frequency (Fig. 3.7). According to these frequencies, the channels of the receiving systems are tuned. The Chang'E-3 lunar lander transmits two tones on both sides of the carrier frequency channel.
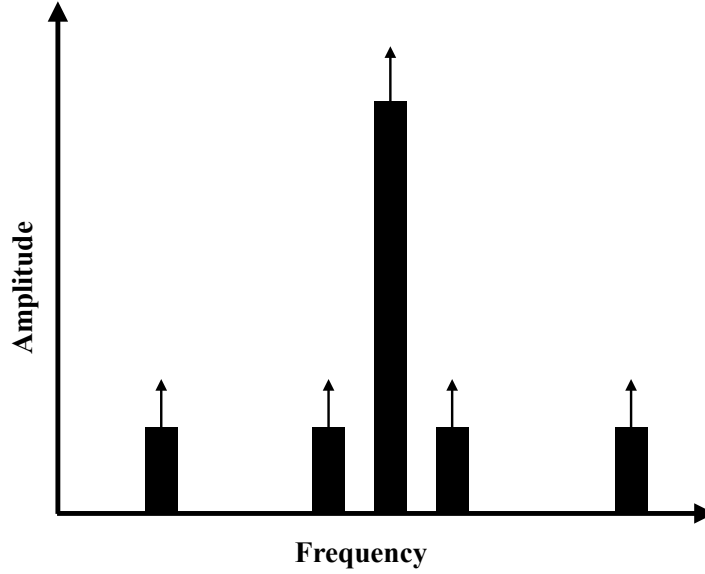

Figure 3.7: Theoretical Downlink DOR Tone Spectrum (monocromatic, represented by arrows) and VLBI Frequency Channels (not to scale).

The concept of DOR is based on the fact that the group delay (e.g., of a spacecraft) τ_{SC} is actually the phase slope over frequency according to:

$$\tau_{SC} = \frac{\Delta\phi}{\Delta f} \tag{3.8}$$

where ϕ is the phase and f is the corresponding frequency [Berry & Broder, 2005; Maddè et al., 2006]. After the raw data of VLBI is recorded and correlated, the search for delay and delay rate residuals are preceded by normalization of correlation output. With a coarse search, a fine search (bandwidth synthesis) is performed using phase information from each of the channels of the normalized correlation data. The delay obtained from a fine search is represented as the phase slope of frequency. With ϕ_j^i denoting the individual phase, for station i, tone j and the corresponding frequency j, a differential phase measurement is made for each of two tones for determining a delay according to eq. 3.8:

$$\tau_{SC} = \frac{(\phi_2^1 - \phi_2^2) - (\phi_1^1 - \phi_1^2)}{f_2 - f_1} \tag{3.9}$$

Therefore, with only two DOR tones, the group delay can be determined theoretically. The purpose of additional DOR tones is to resolve the phase ambiguity which is inherent in concept [BOOK, 2013]. According to the basic theory of the determination of group delays, the two outermost channels have the largest frequency separation referring to as the spanned bandwidth and have the most strength to determine the group delay observable. The two inner channels are used primarily for the resolution of the integer cycle phase ambiguity.

To explain this, we first look at the case of two DOR tones. In Fig. 3.8, a plot of the fringe phase for each tone is illustrated with frequency as the horizontal axis and phase as the vertical axis. There two columns of points representing the phases of the two DOR tones. The horizontal separation between the two columns of

phases is the spanned bandwidth. The columns are formed by 2π ambiguities of the phases. Without knowing the correct number of full cycles between the two frequencies, any slope may be possible. In Fig. 3.8, the solid line may be the true slope and the dashed line is one possible false slope from which the time delay may be inferred. Of course, there are also other possible false slopes but they are not shown here. According to the basic theory and purpose of DOR measurements, as shown in Eq. 3.8, it is not necessary to determine a certain point in each column to represents the true phase, but the true slope, which stands for the rate of phase over frequency, is necessary for the determination of the actual group delay. The difference between the time delay from a false and true slope is the integer cycle ambiguities.
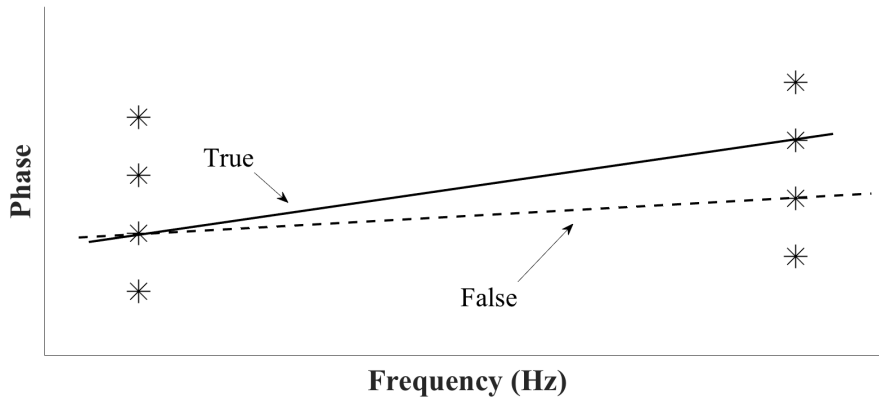

Figure 3.8: Phase Ambiguity with two DOR Tones.

To find the true slope and determine the delay, more DOR tones are to be applied. Fig. 3.9 illustrates a plot of phases for each of four tones. The additional two columns of points are the phases corresponding to the two added DOR tones. The slopes of true and false cases from the two-tone case are reproduced. It is immediately obvious that the false slope is not supported by phase values of the inner frequencies while the true slope is formed with points in each of the four columns connected. By this, the true slope can be distinguished from any false slopes.
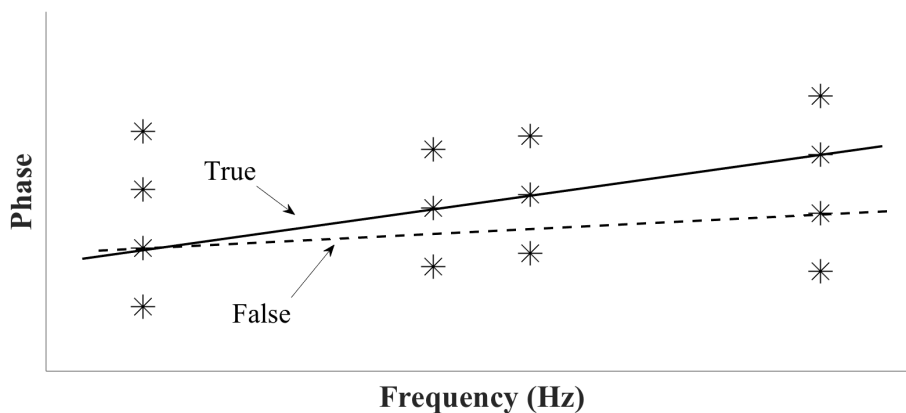

Figure 3.9: Phase Ambiguity Resolution with four DOR Tones.

It is of importance to use as large as possible a spanned bandwidth for the DOR tones but it is also necessary to take into consideration the problem of ambiguity resolution. Besides adding two tones for the resolution of ambiguity as shown in Fig. 3.7, the ambiguity can also be resolved by including more tones for redundancy purposes. However, including more tones will affect the link power.

Turning to the delta in delta-DOR, the reference source is typically a quasar whose angular position in the sky is well known and cataloged, having been previously measured and studied. For measuring the quasar, each station is configured to acquire the signals in frequency channels centered on the spacecraft tone frequencies. The choice of the receiver frequency channels ensures that the spacecraft-quasar mode eliminates the effects of ground station clock offsets and instrumental delays. By selecting a quasar target that is close to the spacecraft in an angular sense and observing the quasar at nearly the same time as the spacecraft target, the effects of transmission media delays can be reduced as well. A spacecraft target with positions more accurately known than the target, sometimes can also be a reference. As for receiving the downlink signals, deep space stations as well as common radio telescopes can do these observations.

A Delta-DOR experiment normally consists of a number of scans with each of them having a duration of a few minutes. A scan consists of pointing multiple antennas to the same radio source (the spacecraft or the reference quasar source). The observing sequence of Delta-DOR is typically spacecraft-quasar-spacecraft (SQS) or quasar-spacecraft-quasar (QSQ) [Berry & Broder, 2005]. The received signals are recorded and brought to a correlator. The observed quantity in a Delta-DOR session is the time delay for the corresponding radio source, natural or artifical, on a single baseline. A scan of n telescopes thus normally produces $n \cdot (n-1)/2$ observations.

4. Group delay determination

As we introduced above, the determination of the group delays from raw VLBI data is an important part of VLBI, which produces observables as input for further analysis. The group delay observables needed for estimating geodetic parameters are determined by a correlation process and a level-1 data analysis referred to as fringe fitting process [Nothnagel, 2019]. Although the signal processing algorithms and procedures are established for extra-galactic radio sources in geodetic VLBI and space agencies have long experience dealing with DOR tones, applying DOR tones in geodetic VLBI mode has just started. For this to work, the processing algorithms and procedures have to be adapted. In this section, the general work flow of correlation processing for the OCEL project is described. The algorithms and processing pipelines of fringe-fitting are introduced and discussed corresponding to fringe-fitting software tools.

4.1   Correlation of OCEL data

The correlation process is an important part and necessary step of geodetic VLBI. With technical developments especially in digital computation and following the need for ever higher accuracy, constant progress has been made in the capabilities of geodetic VLBI correlators [Nothnagel, 2019]. In this respect, DiFX [Deller et al., 2007, 2011] has become a widely used software correlator in geodetic VLBI. With the basic theory of correlation being the same for geodetic DOR tone and quasar observations, the relevant parts of the correlation of the OCEL data with the DiFX software correlator are discussed in the following paragraphs, starting from preparing the control file, including all preprocessing tasks and producing the final correlation outputs for later analysis. Apart from using a near field model computed with the ephemerides of the target, the other parts of the correlation workflow for the OCEL sessions stay the same as for pure quasar observation sessions. A description of the complete correlation process in VLBI including the concept and some of the important practical aspects can be found in Nothnagel [2019].

To start the correlation process, the correlation control file .v2d has to be set up containing five types of information, EOPs, VEX file paths, data paths, antenna clocks and some control parameters. The VEX file is short for VLBI Experiment Definition Data file, which stores the VLBI experiment definition including the schedule and all the frequency settings. The control parameters must include integration time (tInt) and number of channels per spectral window (nChan). The number of channels per spectral window is related to the frequency resolution of the Fast Fourier Transform (FFTSpecRes). In theory, the more channels per spectral window, the more accurate the results will be. However, larger numbers of channels per spectral window will lead to more FFT calculations. Considering the calculation work and expected accuracy, a proper number of channels per spectral window should be determined and used. For the OCEL data, we performed an analysis with different numbers of channels per spectral window and selected a proper number, which is discussed in Sec. 7.5.

With the control file as input, the program vex2difx produces the four output files (i.e., .calc file, .input file, .joblist file and .flag file). Taking the information in the .calc file, the program difxcalc (or calcif2) generates the .im file which contains the a priori geometric delays and atmospheric delays required by the correlation program DiFX. The delays are also called the interferometry model. If the target is not a quasar, we have to feed target ephemerides into the .calc file as a priori information in specific formats.

In the correlation process, the time tag of the observations is usually shifted to the moment when the wavefront reaches the geocenter, and the corresponding group delay is called the geocentric delay. The delay model of the DiFX software correlator is computed as a sum of a fifth-order polynomial fit to the geocentric delay, linear clock offset, and the coarse atmospheric model delay over intervals of 120 seconds. The a priori geocentric delay of the reference station τ_{ag}^{rf} related to the time tag of the wavefront arrival to its phase center can be expressed from the fifth-order polynomials as

$$\tau_{ag}^{rf} = \sum_{k=0}^{k=5} p_k^{rf}(t_{srt} - t_0 - (\tau_{ag}^{rf} - \tau_{cl}^{rf} - \dot{\tau}_{cl}^{rf}\tau_{ag}^{rf} - \tau_{atm}^{rf}))^k \tag{4.1}$$

where p_k^{rf} stands for the polynomial coefficients and k is the order of the polynomial; t_0 is the polynomial start time; τ_{cl}^{rf} and τ_{atm}^{rf} are the clock offset and atmospheric dela, respectively. Eq. 4.1 is solved by iterations. With the value τ_{ag}^{rf}, we compute the a priori delay for the remote station of the baseline

$$\tau_{ag}^{rm} = \sum_{k=0}^{k=5} p_k^{rm}(t_{srt} - t_0 - (\tau_{ag}^{rm} - \tau_{cl}^{rm} - \dot{\tau}_{cl}^{rm}\tau_{ag}^{rm} - \tau_{atm}^{rm}))^k \tag{4.2}$$

The a priori delay rate is computed with an expression similar to Eq. 4.1 and Eq. 4.2. Then we can compute the total delay by extrapolating the residual delay to the SRT

$$\tau_{tot} = \tau_{ag}^{rm} - \tau_{ag}^{rf} + \tau_{res} + \dot{\tau}_{res}(t_{srt} - t_{frt}) \tag{4.3}$$

where τ_{res} is residual delay and $\dot{\tau}_{res}$ is residual delay rate. It should be noted that the delays involved here are geocenter delays.

Depending on the scan duration, a number of a priori delay model points are needed. The number of model points in a single scan follows the relationship:

$$NMP = integer(\frac{SD + inc - 1}{inc} + 1) \tag{4.4}$$

where NMP stands for the number of model points; SD is the duration of the scan; inc presents the increment, which is here the default interval 120 seconds. In one model point, there is one set of polynomials for the 120 seconds duration. For reasons of convenience and coverage, the start epoch of the model point of a single scan is usually not the very start time of the scan, but a few seconds ahead of the scan. For instance, the followings are some information related to the time tag in a common .calc file:
JOB START TIME: 57034.3164815
JOB STOP TIME: 57034.3175231
START MJD: 57034.3164815
START YEAR: 2015
START MONTH: 1
START DAY: 12
START HOUR: 7
START MINUTE: 35
START SECOND: 44
SCAN 0 START (S): 0
SCAN 0 DUR (S): 90

where the interval is by default 120s seconds. The corresponding .im file contains the information of start epoch of a priori delay model listed as:
SCAN 0 POLY 0 MJD: 57034
SCAN 0 POLY 0 SEC: 27240

The integer day part of the start epoch MJD stays the same, and the START HOUR and START MINUTE are converted into seconds as the START SEC. If the scan length is longer than half an interval, then the START SEC is shifted backwards by half an interval. In the case above, the start epoch is 44 (START SECOND in .calc file)+60(half interval) seconds ahead of the actual scan start time. The number of model points are two. With this setup, the a priori delay model covers the whole scan. These relationships and setups are important to be clear, when we insert the ephemeris of the Chang'E-3 lunar lander in the .calc file and generate the corresponding a priori delay models in .im file.

With the pre-correlation files set up and broadband data, the core of DiFX software correlator called mpifx-corr can produce the visibilites, which reflect the cross-power spectra (amplitudes and phases across frequency bands). The visibilities produced by mpifxcorr are written to a directory with extension .difx. Typically there will be a single file in this directory, but it is possible that the output data will be split into multiple smaller files if the first output file gets too large or if correlation is continued from a point midway through correlation. Each record contains the visibility spectrum for one polarization of one baseband channel of one baseline for one integration time. With the visibilities, we can use either difx2mark4 or difx2fits to generate an output in different formats as input for further processing.

4.2 Fringe Fitting

As described above, the correlator integrates the observation data with an a priori model of delay and delay rate. Applying an a priori model with a correction reduces the computational costs and makes the correlation more efficient. As a consequence, the calculations needed for the correlation have to be performed only in the vicinity of the expected group delay observable. The a priori model is based on the a priori information of the target position, the telescopes coordinates, atmospheric refraction delays, Earth orientation parameters and the offset of the two station clocks at the time of the observation. Due to uncertainties remaining in these parameters, there are never absolutely accurate values in the a priori delay model, which leads to a residual delay and delay rate in the interferometer phase.

As a first-order approximation, the linear phase model by the correlator can be expressed as [Cotton, 1995]:

$$\Delta\phi_{t,\nu} = \phi_0 + \frac{\partial\phi}{\partial\nu}\Delta\nu + \frac{\partial\phi}{\partial t}\Delta t \tag{4.5}$$

where ϕ_0 is the interferometer phase at the reference time and reference frequency, $\frac{\partial\phi}{\partial\nu}$ is the phase slope w.r.t. frequency and represents a residual delay, $\frac{\partial\phi}{\partial t}$ is the phase slope w.r.t. time and represent the residual fringe rate, and Δt and Δv are the values relative to the reference time and frequency.

The fringe frequency f is the rate of variation of the fringe phase, typically in Hz or mHz. It is the differential Doppler-shift. The delay rate $\dot\tau$ is the rate of the variation of the delay, which is dimensionless. The relationship between delay rate and fringe rate is expressed as:

$$\frac{d\tau}{dt} = \frac{1}{\nu} \cdot \frac{d\phi}{dt} \tag{4.6}$$

In VLBI, the task at hand now consists of finding the phase where the amplitude has its maximum depending on the delay τ and the delay rate $\dot\tau$, which relates to the fringe rate only by multiplying it with the observing frequency.

$$A(\tau, \dot\tau) = \quad \text{max!} \tag{4.7}$$

This can be achieved by basically searching the two dimensional array of visibilities for the maximum value of the amplitude which is equivalent to accommodating for the inaccuracies in the a priori model. Since the grid points of the arrays have too course a resolution, the delay and delay rate residuals are estimated from the arrays of visibilities over all accumulation periods and trial lags in the fringe-fitting process [Cappallo, 2017].

There are multiple ways to do fringe-fitting. It is easiest to explain a fringe-fitting algorithm along the lines of well established procedures. In the following, we thus introduce the fringe-fitting software packages (*fourfit*), which is part of the Haystack Observatory VLBI Processing Software (HOPS)[1], and the package PIMA [Petrov et al., 2011]. The basic algorithms and the workflow are described and discussed. Owing to the special features of DOR tone signals, a new fringe-fitting algorithm dealing with DOR tone signals had to be developed which was realized by an augmentation of HOPS/*fourfit* called *fourfit*-DOR [Han et al., 2019] making use of experiences also gained with PIMA. The algorithm and features of the *fourfit*-DOR package are described and discussed at the end of this chapter.

---

[1]https://www.haystack.mit.edu/tech/vlbi/hops.html

4.2.1 PIMA

PIMA is a fringe-fitting software taking visibilities in the FITS-IDI format as input. The output of the fringe-fitting procedure is written either in a plain ascii file or a binary database. PIMA uses a control file to place all control parameters that are needed for processing and has a flexible command-line interface.

A general work-flow including a number of processing steps, related basic theory and algorithms are described as follows:

- Load the data

  After preparation of the PIMA control file, as the first operation, load the FITS-IDI data. PIMA extracts information about stations, sources, frequencies, a priori models, phase calibration, etc.. It then splits the data into scans and observations. The relevant information of data according to scans and observations are written as tables into .pim binary files.

  PIMA reads the data and information and makes index tables for the visibilities. During the operation, many checks are performed, which check the control file, stations names, sources names, frequencies, etc. Wrong key-words in control file, unlisted stations names and source names will lead to a termination. Visibilities as identified as incorrect are listed in a log file. After loading the visibilities, parsing the log files is an optional step which extracts system temperature, cable calibration and meteorological information into tables. With or without information in log files, it has no influence on fringe-fitting and is just preparation for analysis.

- Examine raw data and calibration information

  After loading the data, examining the data and calibration information is necessary. A successful load will generate a series of relevant files which contain basic information of the data in table formats. In particular, PIMA looks at the phase calibration information which the DiFX software correlator extracts. In order to avoid applying arbitrary values, the data are flagged if phase calibration information is not available.

- Coarse fringe-fitting

  With data loading completed, a coarse fringe search is performed on all data of an observation. The results of the coarse search are used to mask bad data. The correlator output provides a cross-correlation spectrum for each baseline and each scan. The cross-correlation spectrum is computed at a two-dimensional(2D) grid of accumulation periods and frequencies. Then the program searches for the maximum amplitude and the respective group delay τ_{gr}, its derivation $\dot{\tau}_{gr}$, phase delay τ_p and phase delay rate $\dot{\tau}_p$ in the time and frequency domain. These delays and delay rates are rough corrections w.r.t. the a priori correlator interferometry model values.

  $$C(\tau_{gr}, \dot{\tau}_{gr}, \tau_p, \dot{\tau}_p) = \sum_k \sum_j c_{kj} w_{kj} \times e^{i(\omega_0 \tau_p + \omega_0 \dot{\tau}_p (t_k - t_0) + (\omega_j - \omega_0)\tau_{gr} + \omega_0 \dot{\tau}_{gr}(t_k - t_0))} \qquad (4.8)$$

  where C is a function of the complex cross-correlation spectrum; k is the discrete time, and j stands for frequencies; c_{kj} are the complex cross-correlation samples; ω_0 and t_0 are the reference frequency of the band and the reference time within the scan; w_{jk} is weight. The amplitude of the function 4.8 has a global maximum and the corresponding values of the peak are the expected delays and delay rates.

  For the search of the maximum, the first step of the coarse fringe search is to compute the 2D fast Fourier transform (FFT) of the matrix of the cross correlation spectrum. The two dimensions are time and frequency. The FFT produces estimates of $|C|$ at a discrete grid of group delays and delay rates. The group delay and delay rate corresponding to the maximum of the discrete Fourier transform of the cross correlation matrix provide the coarse estimates of group delay and delay rate. Then an iterative procedure to compute $|C|$ in the vicinity of the maximum with a discrete 3D Fourier transform is performed. The third dimension is the group delay rate. With iterations, group delay, phase delay rate and group delay rate are obtained.

- Data pre-reduction

  To reduce the influence of radio-frequency interference (RFI) and improve the SNR, PIMA allows to pre-reduce the data by masking out specified spectrum channels of the correlator output. RFI influences the auto-correlation spectrum with forming more peaks. These peaks should be eliminated or ignored by certain rules. At the same time, the cross-correlation spectrum can be distorted by external RFI. Besides RFI, weak or no signal in certain given spectral channels will lead to a low SNR. For these two problems, if there isn't signal or only weak signal or RFI exists in given spectral channels,a pre-reduction of masking out these specified spectrum channels is applied. On the other hand, when we only need to include specified spectral channels, we can mask out all other spectral channels to achieve that.

- Fine fringe search

  In order to find the final delays, a fine fringe search is the main step. After coarse fringe search and masking data, the fine fringe search is performed. With masking data applied, bad data masked out and some control parameters changed, the algorithms and procedures of fine fringe search are the same as coarse fringe search.

- Export data

  After the fine fringe search, the fringe-fitting results are stored and exported. The task *mkdb* reads all fringe information and visibility from intermediate binary *.pim* files, computes the final results and writes them into database files in either binary Geo VLBI Format (GVF) or ascii (TEXT) format [Petrov et al., 2011]. The results of the fringe search are residual phases and group delays as well as their time derivatives with respect to the a priori delay model used in the correlation.

  Very important is to compute the total path delay corresponding to a certain epoch of time for all observations of a scan, called scan reference time (SRT). The task computes the SRT, computes a priori geometric delay and atmospheric delay referred to the SRT, and computes the total group delays and related observables referred to the SRT. Since fringe searching for different baselines is performed independently, each observation has its own reference time, called fringe reference time (FRT). Usually, the FRT is computed as the weighted mean epoch of a given observation. Due to different starts or ends of stations observing the target, the durations are different for different baselines, and the FRT is different at different baselines. PIMA allows three options for setting the SRT, the middle of scan, the same as FRT and other certain values. If setting the SRT as the same as the FRT, the SRT may be different for each observation within one scan; If setting the SRT in the middle of the scan, it applies in two ways. One is for the case of that all stations started and ended observing at the same time, which means all observations have the same length of duration, the SRT for each observation is the middle epoch of the scan duration. However, the other way is for the case of that if it finds observations that are not in the common range, it splits the scan into sub-arrays that are treated as separate scans. At last, for each remaining sub-array, PIMA assigns the scan reference time that is in the middle of the common range. If setting the SRT at a specified value, it is an offset from the start of scan, usually it is used after a coarse search, with information of the start of scan.

  Having a common SRT for all baselines within one scan is desirable, which help the further computation and analysis e.g. triangle closure delays. But in practice it is difficult to set a common SRT for all baselines within one scan, and the only way is to set a common SRT for as many baselines as possible.

  At the same time, the uncertainty of group delay estimate is minimal at corresponding FRT. And the uncertainty transfers to a group delay at SRT expressed as

  $$\sigma_\tau^2(t_{srt}) = \sigma_\tau^2(t_{frt}) + 2Cov(\tau, \dot{\tau})(t_{srt} - t_{frt}) + \sigma_{\dot{\tau}}^2(t_{srt} - t_{frt})^2 \qquad (4.9)$$

  where σ_τ is the uncertainty of a group delay, t_{srt} and t_{frt} are the epoch of SRT and FRT; $\dot{\tau}$ is a delay rate. According to the Eq. 4.9, the uncertainty increases with the difference between t_{srt} and t_{frt}.

4.2.2   HOPS/$fourfit$

Besides PIMA, the Haystack Observatory Post-processing System (HOPS) is another software package handling the correlator output. As a component of HOPS, $fourfit$ is the tool for fringe fitting. It reads the correlator output in Mark4 format as input and generates group delays and other relevant observables. In the following, special aspects of input and output data format, time tags and the basic theory of $fourfit$ are described.

Input and output data format   The input and output data of $fourfit$ are both in Mark4 format, which is modeled according to the MkIII data formats [Rogers et al., 1983]. The MkIII system uses three file types, numbered 0, 1 and 2, which are the root, core and fringe files, respectively. All of them are binary format. A fileset consists of a single root file, and multiple type-1 and type-2 files all of which belong to one type-0 root file. The root files contain global information about the scan, while the type-1 and type-2 files contain the raw correlation counts plus minimal identification information, and the results of a fringe-fitting operation, respectively. The concept of root, core and fringe files remains from the MkIII era, but two additional file types have been added. These are the type-3 (station data) files, and the type-4 (log) file. The type-3 files, one per station, contain model spline coefficients, phasecal data, state count information, and tape error statistics (in MkIII, some of this information was embedded in the type-1 file records). The type 4 file, one per root, contains generalized ASCII log information both from the field system and from the correlator, specific to the fileset. It is worth to mention that in type-2 files, besides the final observables such as the group delays, some other intermediate observables are stored. For instance, the final group delay as output is baseline based, but the geocentric group delay is also generated and stored in type-2 files, which will be used in triangle closure delay analysis in Sec. 7.2.

Time tag in $fourfit$ Similar to PIMA, $fourfit$ uses SRT and FRT as time tags. However, the definitions and selections of SRT and FRT in $forufit$ are different from PIMA. Normally, the observations in a scan have the same start time. In $fourfit$, the integer part of the middle point of the shortest duration observation in the scan is taken as the SRT of the scan. And the FRT in $fourfit$ is set to be equal to SRT. According to the definition and selection rules, compared with PIMA, the advantage is that all the observations in a scan share the same SRT, which leads to the same reference time for the output group delays in a scan. What's more is that the observations' structure keeps consistent with the correlator output, and a single observation will not be cut into several new observations or even a scan into several new scans. This is more convenient for data checks and later analysis. However, at the same time, if in some cases the observations in a scan have different starting time and duration, there may be the possibility that the SRT is not within the duration of some of the observations in the scan. In addition, since the FRT is set the same as the SRT, a very short duration observation may lead to a fringe reference time far away from the middle points of the other observations' duration. That will affect on the results of fringe fitting. This is an important reason that $fourfit$ has problems with processing certain VLBI sessions.

Basic theory and algorithm in $fourfit$ Starting with the basic theory of fringe-fitting, the generic expression of fringe-fitting input visibilities for a single baseline with two antennas is a function of frequency and time. Considering the two complex parts in the formulation, it can be written into a simplified equation, with merging the two amplitudes [Cotton, 1995; Cappallo, 2017],

$$V(t, \nu) = S \, e^{i\phi(t,\nu)} \tag{4.10}$$

where S is a new single product combining two amplitudes, t is time, ν is frequency and ϕ is phase.

With discarding the time dependence in Eq. 4.10, regarding it as 1-D and linearizing the phase with some reference frequency, we find

$$\phi_\nu \approx \phi_{ref} + (\nu - \nu_{ref}) \, \dot{\phi}_{ref} \tag{4.11}$$

where ϕ_{ref} is the reference phase, ν_{ref} is the reference frequency and $\dot{\phi}_{ref}$ is the reference phase rate.

After Eq. 4.11 is multiplied by a weight function $w(\nu)$, a Fourier transform of the results is expressed as:

$$B(\tau) = Se^{(i[\phi_{ref} - \dot{\phi}_{ref}v_{ref}])}\delta(\dot{\phi}_{ref} - 2\pi\tau) * \epsilon(\tau) \qquad (4.12)$$

where τ is the lag time. The function $\epsilon(\tau)$ is the Fourier transform of the weight function:

$$\epsilon(\tau) = \frac{1}{\int_{-\infty}^{\infty} dvw(v)} \int_{-\infty}^{\infty} dvw(v)e^{2\pi iv\tau} \qquad (4.13)$$

Then the calculation of the power spectrum of $B(\tau)$ is performed and the result is:

$$q(\tau) = B(\tau)B(\tau)^* = S^2\delta(\dot{\phi}_{ref} - 2\pi\tau) * \epsilon(\tau)\epsilon(\tau)^* \qquad (4.14)$$

According to Eq. 4.14, firstly find the peak in the power spectrum $q(\tau)$ and corresponding τ_{max}; with the relationship, $\dot{\phi}_{ref}$ can be obtained; then ϕ_{ref} can be deduced from the phase of $B(\tau)$ at τ_{max}.

Over a short enough time interval, a linear variation of phase with frequency and time can be analyzed by a 2-D extension of the Fourier Transform. The linear variation in the frequency direction is proportional to the delay as before, whereas the variation with time now is associated with the fringe rate, which is measured in frequency units.

Then, the basic processing flow of fringe-fitting in $fourfit$ is:

- Fourier transformation from frequency domain to delay domain to find the delay and from time domain to delay rate domain to find the fringe/delay rate for each channel separately;

- Coarse grid search of peaks in the delay and delay rate domain. The coarse search procedure corrects residual delay errors only in separate bands instead of across all frequency bands;

- 3D fine search in the single band, multi-band and delay rate box and refinement of the parameter estimates. The fine search is used to solve the residual errors of the delay by making corrections over all frequency channels with adjustments made to phase rotation.

4.2.3 $fourfit$-DOR

The standard fringe fitting tool used in geodetic correlators is the program $fourfit$. This software is in use, e.g., at Haystack Observatory and the Bonn Correlator Center for processing geodetic correlation output of observations of natural extra-galactic radio sources. The DOR tones emitted by the Chang'E-3 lunar lander were observed in a standard geodetic VLBI mode with a network of observatories of the IVS. Considering the features of the DOR tones, the new algorithm is applied in the frame of $fourfit$ for the fringe-fitting of the DOR tones signal, which is named as $fourfit$-DOR [Han et al., 2019]. The new processing scheme is realized by modifying the existing $fourfit$ routine for processing DOR tone data. The input to $fourfit$-DOR is the same as $fourfit$, which is the output of the DiFX correlator in the form of complex visibilities. Besides that, in each scan folder of the input, a file containing a priori information for the nominal tone frequency and the Doppler effect is added. $fourfit$-DOR was designed to keep the processing workflow and the output the same as in $fourfit$.

The need for addressing the issue of DOR tone fringe fitting arose in the OCEL project. The Chang'E-3 lunar lander transmits DOR tones signal and it was observed with channels of 4 or 8 MHz bandwidth. Compared with the case for quasar targets, the spectrum and delay resolution function are quite different.

The DOR tones produce a narrow main peak with some small ones close to it in the frequency spectrum. After transforming this into the delay domain, a rather flat delay resolution function is produced.

For quasar targets, the spectrum of the interferometer response is fairly flat through a similar level of amplitudes in the visibility array. As a consequence, there is an obvious main lobe with some side-lobes in the delay resolution function.

Furthermore, to perform fringe fitting for DOR tones with standard fringe fitting software brings the negative effect that all the amplitude variations of the frequency spectrum of a channel from any type of correlated interference will be carried over from the frequency domain to the delay domain with the Fourier Transform. For instance, the $fourfit$ algorithm performs a three dimensional fit over all delays and accumulation periods by transforming the visibilities from the frequency domain into the delay domain through a Fourier transformation. This ignores some of the information content and inevitably induces more noise which then distributes over the whole frequency band within the channel. The idea behind $fourfit$-DOR is that the correlator output is pre-processed in the frequency domain firstly to identify the frequency of the DOR tone in the cross-power spectrum. Normally, this is identical to the nominal transmission frequency but may have been corrupted easily by noise contributions. The time series of amplitudes and phases per accumulation period for each channel are then used for a 2-dimensional search of the residual multi-band delay and residual delay rate. More details about $fourfit$-DOR can be found in Han et al. [2019].

The general algorithm in $fourfit$-DOR is:

- Search the cross-power spectrum for the location of the maximum amplitude in the vicinity of the nominal DOR tone frequency.

- Fourier transformation over all accumulation periods (APs) from the time domain to the fringe rate domain to produce visibilities $V(f, \nu)$ in the fringe rate domain for each channel independently.

- Perform Fourier transformation of the visibilities $V(f, \nu)$ from the frequency domain to the delay domain. Coarse grid search the peak and obtain the values of f and τ corresponding to the maximum magnitude of the peak.

- Correct phases for frequency dislocation. The local oscillator frequencies are normally applied for the relationship between frequencies and phases for the computation of the multi-band group delay according to $\tau = d\phi/d\nu$. However, the DOR tone has a specific frequency somewhere in the band and is thus different from that of the local oscillator frequency.Consequently this frequency has to be applied. This is done through correcting the phases according to

$$V_r(t, \nu) = V(t, \nu)\mathrm{e}^{-\mathrm{j}2\pi\{C_f t f_{\mathrm{res}} + (C_f - C_{\mathrm{ref}})\tau_{\mathrm{mbd}}\}} \tag{4.15}$$

where C_f is the DOR signal frequency value of each channel, C_{ref} is the reference frequency set in bandwidth synthesis while f_{res} and τ_{mbd} are residual fringe rate and residual delay derived from the coarse search, respectively.

- The last step of this process is a parabolic interpolation about the maximum visibility. With a fine search, we obtain the multi-band delay and delay rate more accurately [Han et al., 2019].

5. Estimation of position on the Moon

5.1   Near-field VLBI Time Delay Model

The establishment of a precise VLBI delay model is one of the essential parts to make the full use of the power of VLBI. For sources at infinite distances such as extra-galactic radio sources, various models have been proposed (e.g., [Hellings, 1986; Soffel et al., 1991; Shahid-Saless et al., 1991]). A consensus model of Eubanks [1991] was introduced with 1 ps precision for Earth-based VLBI observations of extra-galactic radio sources. IAU Resolution B1.3 (in 2000) recommends to use the BCRS and GCRS in the framework of general relativity [Soffel et al., 2003]. The consensus model was adapted to the BCRS and has been used in IERS Conventions [McCarthy & Petit, 2004] as the standard VLBI delay model for a long time already. However, it should be noted that the model was designed for extra-galactic radio sources and was based on the plane-wave approximation by ignoring the effect of finite source distances [Eubanks, 1991].

For targets within the solar system, the consensus delay model is not applicable. In the finite distance case (near-field), a curved wave-front has to be used instead of a plane one. Besides that, the motion of the target needs to be considered. The developments of a VLBI delay model for finite distance radio sources have gone through various develoment steps by Klioner [1991], Moyer [2000], Fukushima [1994], Sekido & Fukushima [2006] and Duev et al. [2012]. In Moyer [2000] and [Klioner, 1991], the VLBI delay model for spacecraft observation were introduced introducing numerical iterations. In Fukushima [1994], Sekido & Fukushima [2006] and Duev et al. [2012], the VLBI model was given in a similar form as the consensus model with vector formula. The models by Sekido & Fukushima [2006] and Duev et al. [2012] have been primary choices for the analysis of near field VLBI observations in recent years. The difference between the two of them is that Sekido & Fukushima [2006] uses one light time equation while Duev et al. [2012] uses two of them.

An analytical expression of the VLBI delay for satellite targets with the Earth as a central body and observed by Earth-based stations was presented quite recently in Jaron & Nothnagel [2019]. With double light time equations applied in the model and linearizing of the target orbit, a compatible accuracy level was achieved in this analytical VLBI delay model as compared to the ones using numerical integrations. One of the differences between the two is that the model of Jaron & Nothnagel [2019] is for the targets orbiting the Earth, while our model is designed for the lunar lander. According to the basics of near field models and related tests, we know that a model is usually sensitive to the distance from a target to the stations. A different distance and central body of a lunar lander w.r.t a satellite orbiting the Earth might lead to quite different results. Whether the two models are applicable to the cases of each other needs further investigations. The other difference is that the model of Jaron & Nothnagel [2019] analytically solves the light time equation in GCRS with certain simplification and approximation for the the special case of satellites orbiting the Earth.

Since this model was not yet available when we needed it for the analysis of the OCEL observations, we had to derive an independent VLBI delay model and had to develop the corresponding partial derivatives for a near field target, especially for a lunar artificial target observed by Earth-based stations based on the former investigations. In our model, the light time equation is solved in BCRS with numerical iterations.

5.1.1   Light Time Equation

The light time equation (or light time solution) is used to compute the one-way light travel time of the signal propagating from the moving target to the tracking station on Earth from the time of arrival of the signal. In order to compute the theoretical delay observable, solving the light time equation is necessary. As shown in fig. 5.1 for a single station and one-way signal, with transmitting epoch t_e and receiving epoch t_1 , the light time equation can be modelled. Usually the receiving epoch t_1 is recorded, and the transmitting epoch t_e can be computed with iterations.
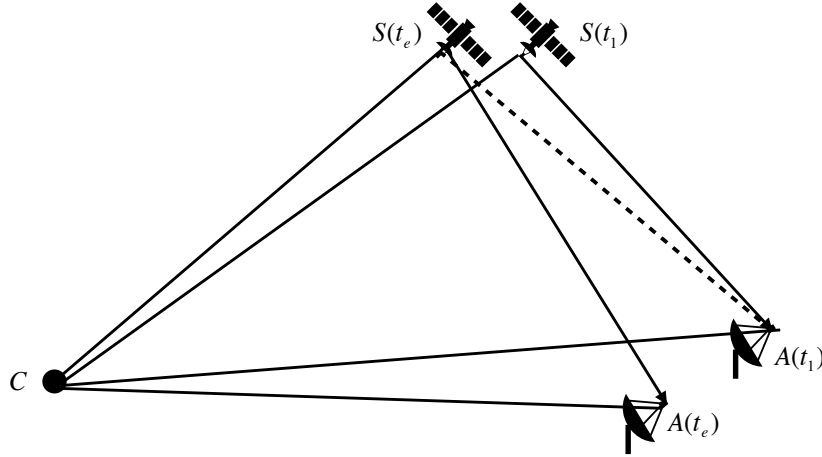
Figure 5.1: Geometric relationship of the vectors involved in the computation of the light time solution, where C is the solar system barycenter; A is the antenna receiving signals; S is the spacecraft transmitting signals

Figure 5.1 shows the schematic diagram of the state vector relationship between target, stations and intermediate planets. $S(t_e)$ and $S(t_1)$ are the position of the spacecraft in BCRS at time t_e and t_1 in TDB respectively. Similarly, $A(t_e)$ and $A(t_1)$ are the position of the antenna in BCRS at time t_e and t_1 respectively.

The procedure for modeling the spacecraft light time solution can be divided in several steps as discussed below:

Firstly, the spacecraft observations are given in the receiving time t_1 of the UTC time scale. However, the state vectors of target, stations and intermediate planets must be computed in TDB. Therefore, the given receiving time t_1 (UTC) is converted into receiving time t_1 (TDB).

The state vector of antenna A w.r.t the solar system barycenter C at time t_1 (TDB) can be expressed as $\boldsymbol{r}_{CA}(t_1)$. The transmitting time t_e (TDB) and the corresponding state vectors of the target are computed by iterations. As a start, the first approximation of transmitting time t_e (TDB) is usually taken as the receiving time t_1 (TDB). The state vector of the spacecraft target w.r.t the solar system barycenter C at time t_1 (TDB) can be expressed as $\boldsymbol{r}_{CS}(t_1)$. Then using a geometric relationship, the difference in time between the transmitting time t_e and the receiving time t_1 can then be approximated as:

$$\Delta t_{1e} = t_1 - t_e \approx \frac{1}{c}[\boldsymbol{r}_{CS}(t_e) - \boldsymbol{r}_{CA}(t_1)]_{t_e=t_1} \tag{5.1}$$

An updated transmitting time t_e is obtained as:

$$t_e = t_1 - \Delta t_{1e} \tag{5.2}$$

With the updated transmitting time t_e and the relationship of formulation 5.1, the improved value of the difference in time between t_e and t_1 can be estimated as:

$$\Delta t_{1e} = \frac{1}{c}[\boldsymbol{r}_{CS}(t_e) - \boldsymbol{r}_{CA}(t_1)] + \delta\tau_{rel} \tag{5.3}$$

where $\delta\tau_{rel}$ is the relativistic light time correction. Then an iteration loop from Eq. 5.2 to eq. 5.3 is performed until the latest estimate of Δt_{1e} differs from the previous estimate only by a certain threshold.

With this we obtain the transmitting time t_e in TDB.

The radio signal travelling between the target and the antenna on Earth encounters path bending when it passes by the massive celestial bodies, which increases the travelling path and causes a special time delay, known as Shapiro delay or gravitational delay. The relativistic time delays caused by the gravitational attraction of the bodies can be expressed as:

$$\delta\tau_r el = \frac{(1+\gamma)GM_{sun}}{c^3} ln \frac{R_0^S + R_1^S + R_{0,1}^S + \frac{(1+\gamma)GM_{sun}}{c^2}}{R_0^S + R_1^S - R_{0,1}^S + \frac{(1+\gamma)GM_{sun}}{c^2}} + \sum_{j=1}^{10} \frac{(1+\gamma)GM_j}{c^3} ln \frac{R_0^j + R_1^j + R_{0,1}^j}{R_0^j + R_1^j - R_{0,1}^j} \qquad (5.4)$$

where S stands for the Sun and j for the planets of solar system and the Moon. For the calculations, the coordinate vectors of the Sun, the Earth, the Moon and other planets are expressed in BCRS. R_0^S, R_1^S and $R_{0,1}^S$ are the distance between the target and the Sun S, the station and the Sun, and the target and the station, respectively. Similarly, R_0^j, R_1^j and $R_{0,1}^j$ are the distance between the target and the planet j, the station and the planet, and the target and the station, respectively.

5.1.2 Delay Model

As shown in Fig. 5.2, in the BCRS, the signal is emitted by a source at t_e, arriving at antenna 1 and 2 at t_1 and t_2 in TDB, respectively. Then the time delay w.r.t a source at finite distance can be seen as the corresponding time of the differences between the distances from the source to the antennas:

$$\tau = \frac{|\boldsymbol{R}_2(t_2)| - |\boldsymbol{R}_1(t_1)|}{c} \qquad (5.5)$$

where c is the vacuum speed of light, $\boldsymbol{R}_1(t_1)$ and $\boldsymbol{R}_2(t_2)$ are the coordinate vectors from the source to the two antennas, respectively.

With the following procedure, the theoretical time delay can be obtained :

1. Calculation of signal emission time t_e with light time equation solved iteratively.

$$t_e = t_1 - \frac{|\boldsymbol{r}_1(t_1)| - |\boldsymbol{r}_s(t_e)|}{c} - RLT_{1,e} \qquad (5.6)$$

where $\boldsymbol{r}_1(t_1)$ and $\boldsymbol{r}_s(t_e)$ are the coordinate vectors of antenna 1 and the source in BCRS at time t_1 and t_e respectively; $RLT_{1,e}$ is the relativistic light time delay due to the Sun, the Earth, the Moon and other influencing planets which is calculated according to Eq. 5.4 as:

$$RLT_{0,1} = \frac{(1+\gamma)GM_{sun}}{c^3} ln \frac{R_0^S + R_1^S + R_{0,1}^S + \frac{(1+\gamma)GM_{sun}}{c^2}}{R_0^S + R_1^S - R_{0,1}^S + \frac{(1+\gamma)GM_{sun}}{c^2}} + \sum_{j=1}^{10} \frac{(1+\gamma)GM_j}{c^3} ln \frac{R_0^j + R_1^j + R_{0,1}^j}{R_0^j + R_1^j - R_{0,1}^j} \qquad (5.7)$$

Then the signal transmission time from the source to antenna 1 $t_{1,e}$ can be calculated as:

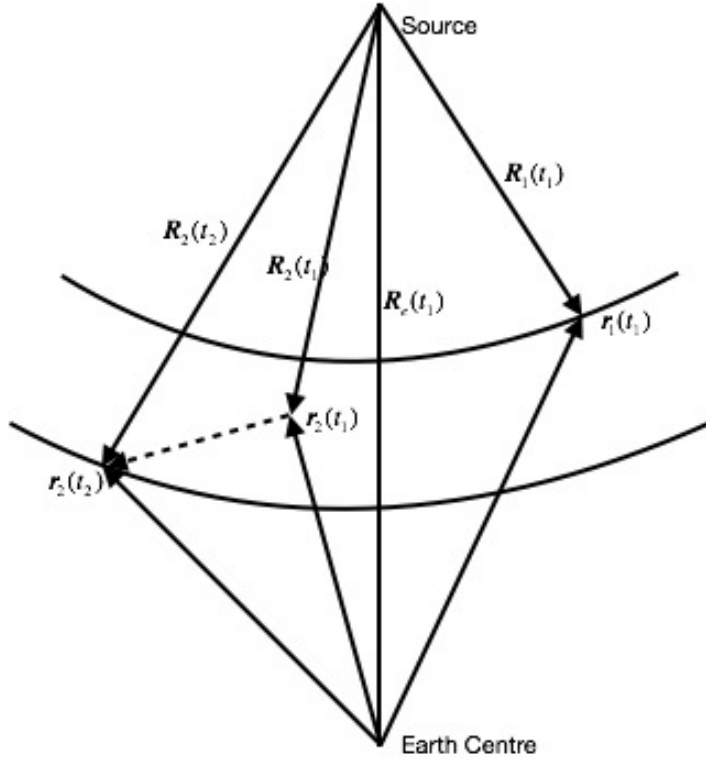$$t_{1,e} = t_1 - t_e \qquad (5.8)$$

Figure 5.2: Geometric delay for near field targets with curved wavefront.

2. Calculation of the time delay of baseline with iterations.

$$t_2 = t_e + \frac{|\boldsymbol{r}_2(t_2)| - |\boldsymbol{r}_s(t_e)|}{c} + RLT_{2,e} \tag{5.9}$$

$$t_2 - t_1 = \frac{|\boldsymbol{r}_2(t_2)| - |\boldsymbol{r}_s(t_e)|}{c} - t_{1,e} + RLT_{2,e} \tag{5.10}$$

where $RLT_{2,e}$ is in the same form as $RLT_{1,e}$.

Then we convert the time delay observables from barycentric TDB to TT as:

$$\tau = t_2 - t_1 - (\delta_{t2} - \delta_{t1}) \tag{5.11}$$

where δ_{t1} and δ_{t2} and are the values of $t_{TBD} - t_{TT}$ for each antenna at the signal emitting epochs, and t_{TBD} is the time in TDB and t_{TT} is the time scale of TT.

The difference between our model and the near field model in Duev et al. [2012] is evaluated numerically for some practical cases. The numerical comparison results are shown in Fig. 5.3. With our near field model and the Duev near field model implemented, the theoretical delays were calculated respectively with the

Chang'E-3 lunar lander as the target source at a number of baselines used in the OCEL sessions. The theoretical delays were calculated once per second and for a period of several minutes corresponding to the scan lengths used. The results of the numerical comparisons to the Duev [Duev et al., 2012] model for one scan show a general level of agreement at the picosecond level (Fig. 5.3).

It should also be noted that the primary factor that affects the geometric delay for near field targets is how far the target is away from the stations. We have also implemented the Sekido near field model [Sekido & Fukushima, 2006] for comparisons. A series of tests and investigations were conducted with the three near field models and targets at different distances to the Earth-based stations. The distance from the target to the stations is involved as an important factor in the calculation of light time equations and the geometric delay. This is the reason why the Sekido near field model agrees with the Duev near field model at the picosecond level with a target around the Venus, but the difference between them for the target of the Chang'E-3 lunar lander is tens of nanoseconds or even larger.

The Duev near field model is currently the most commonly used for spacecraft tracking with VLBI. The accuracy of the model and achieved accuracy of related results with the model are well checked and compatible with those of the other recently well-established VLBI spacecraft tracking projects. The difference between our model and the Duev near field model for the Chang'E-3 lunar lander as the target at global baselines are at the picosecond level. Compared with the accuracy of the observed group delays of the Chang'E-3 lunar lander which is about sub-nanosecond level, the accuracy of our near field model is more than sufficient for our further analysis and investigations.
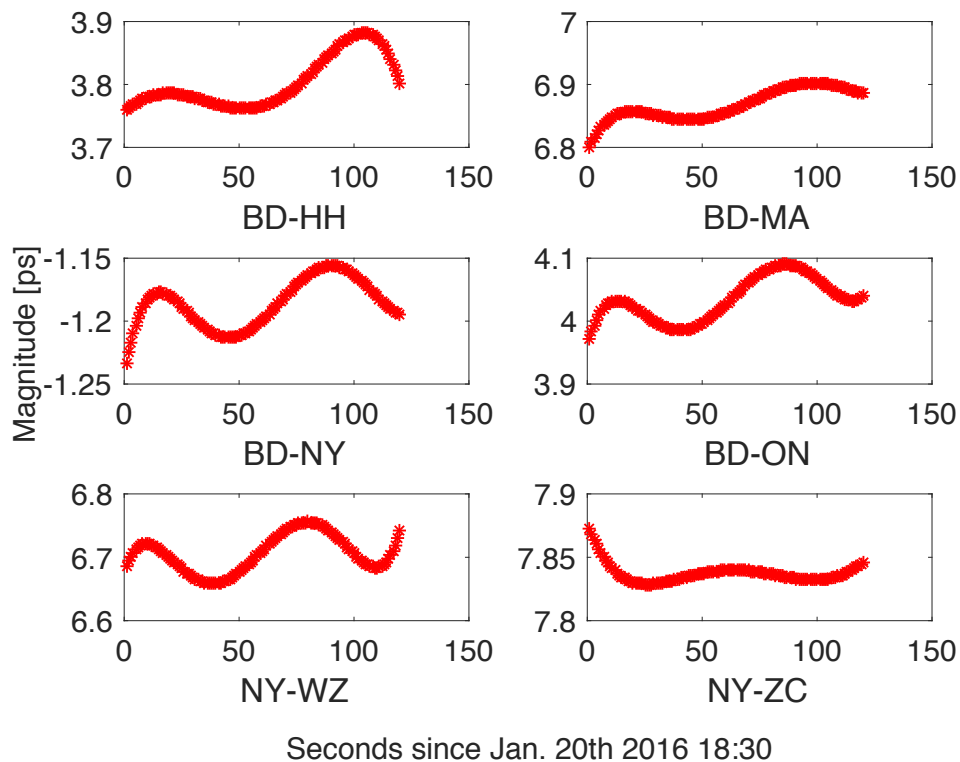
Figure 5.3: Difference in time delay between this near field model and the Duev near field model.

5.2   Partial Derivatives

One of the main purposes of VLBI observing a near-field target is to estimate the position of the target or the state vector as a function of time. Since the lunar lander is on the surface of the Moon, the mean coordinates are considered to be constant in the Moon-fixed coordinate systems with tidal effects being considering a priori. Then its equations of motion only involve the transformation between the Moon-fixed coordinate system(s) and the inertial system.

As recommended by International Astronomy Union (IAU), for high precision applications such as spacecraft operations involving the orientation of the Moon, a lunar ephemeris should be used to obtain the libration angles for the Moon, which define the rotation from the PA system to the inertial ICRS. There are no equations of the motion for Euler angles referenced to the ME system in any ephemeris. The Euler angles provided by JPL ephemeris are numerically integrated and inherently more accurate than knowledge of the mean axes. The constant three-angle rotation from the PA system to the ME system is less accurately known than the integrated Euler angles in the ephermeris, yet enough for meters or lower level accuracy. This is the reason why the coordinates of the lunar lander in the PA system are chosen as the parameters to be estimated.

Since the PA system is a moon-fixed system and the coordinate vectors in our geometric delay model are described in BCRS, the moon centered inertial system is used as a bridge to relate the coordinates vectors in the PA system and the BCRS. This is done because there is only a shift of coordinates from the moon centered inertial system (LCRS) to the BCRS. Then we can formulate the partial derivatives as a chain rule as:

$$\frac{\partial \tau}{\partial \boldsymbol{X}_{pa}} = \frac{\partial \tau}{\partial \boldsymbol{X}_{lcrs}} \frac{\partial \boldsymbol{X}_{lcrs}}{\partial \boldsymbol{X}_{pa}} \tag{5.12}$$

where $\boldsymbol{X}_{lcrs}$ stands for the coordinate vector of the lunar lander coordinates in LCRS and $\boldsymbol{X}_{pa}$ is the vector in the PA system.

$$\frac{\partial \tau}{\partial \boldsymbol{X}_{lcrs}} \frac{\partial \boldsymbol{X}_{lcrs}}{\partial \boldsymbol{X}_{pa}} = \frac{\partial \tau}{\partial \boldsymbol{X}_{lcrs}} \mathbf{M}_{lcrs2pa} \tag{5.13}$$

$$\frac{\partial \tau}{\partial \boldsymbol{X}_{pa}} = \frac{\partial \tau}{\partial \boldsymbol{X}_{lcrs}} \mathbf{M}_{lcrs2pa}$$

here $\mathbf{M}_{lcrs2pa}$ is the transformation matrix from the LCRS to the PA system, obtained from equation 2.13.

To derive the partials of the time delay w.r.t the coordinates in the LCRS, the relationships between time delay and the distances from target to antennas are used. In the next step, the partial derivatives of the delay w.r.t the lander coordinates in the LCRS can be converted to the partial derivatives of distance w.r.t lander coordinates in the LCRS:

$$\frac{\partial \tau}{\partial \boldsymbol{X}_{lcrs}} = \frac{1}{c} c \frac{\partial \tau}{\partial \boldsymbol{X}_{lcrs}} \tag{5.14}$$

$$\frac{1}{c} c \frac{\partial \tau}{\partial \boldsymbol{X}_{lcrs}} = \frac{1}{c} \frac{\partial c\tau}{\partial \boldsymbol{X}_{lcrs}} = \frac{1}{c} \frac{\partial \rho}{\partial \boldsymbol{X}_{lcrs}} \tag{5.15}$$

where c is the velocity of light and ρ is the metric distance corresponding to the time delay.

$$\rho = \rho_2 - \rho_1 \tag{5.16}$$

where ρ_1 and ρ_2 are the distances from the source to each antenna, respectively. They can be expressed in the BCRS as:

$$\rho_1 = \sqrt{(\boldsymbol{D}_1)^2} \tag{5.17}$$

$$\rho_2 = \sqrt{(\boldsymbol{D}_2)^2} \tag{5.18}$$

$$\boldsymbol{D}_1 = \boldsymbol{X}_e - \boldsymbol{X}_1 \tag{5.19}$$

$$\boldsymbol{D}_2 = \boldsymbol{X}_e - \boldsymbol{X}_2 \tag{5.20}$$

where $\boldsymbol{X}_e, \boldsymbol{X}_1$ and $\boldsymbol{X}_2$ are the coordinate vectors of the source and the two antennas in the BCRS, respectively, which are obtained after iterations and applied with gravitational bending. $\boldsymbol{D}_1$ and $\boldsymbol{D}_2$ are the vectors from each antenna to the source.

Then the partial derivatives of the distances w.r.t the lunar lander coordinates in the lunar PA system are:

$$\frac{\partial \rho_1}{\partial \boldsymbol{X}_{lcrs}} = \frac{\boldsymbol{D}_1}{\rho_1} \tag{5.21}$$

$$\frac{\partial \rho_2}{\partial \boldsymbol{X}_{lcrs}} = \frac{\boldsymbol{D}_2}{\rho_2} \tag{5.22}$$

$$\frac{\partial \rho_1}{\partial \boldsymbol{X}_{pa}} = \mathbf{M}_{lcrs2pa} \frac{\boldsymbol{D}_1}{\rho_1} \tag{5.23}$$

$$\frac{\partial \rho_2}{\partial \boldsymbol{X}_{pa}} = \mathbf{M}_{lcrs2pa} \frac{\boldsymbol{D}_2}{\rho_2} \tag{5.24}$$

$$\frac{\partial \rho}{\partial \boldsymbol{X}_{pa}} = \frac{\partial \rho_2}{\partial \boldsymbol{X}_{pa}} - \frac{\partial \rho_1}{\partial \boldsymbol{X}_{pa}} \tag{5.25}$$

5.3 Constraints used in Least Square Adjustments

Since VLBI is an angular measurement technique and has poor accuracy in radial direction compared to the tangential directions, we take advantage of a priori information of the radial component to help estimating the coordinates of the lunar lander accurately. This can be don either by combining the VLBI observations with ranging observations or by adding a constraint to the design matrix. As for the constraint method, three different constraint models were set up and tested.

Constraint 1

The distance between the lunar lander and the Earth's center is a suitable parameter to fill the role as a constraint in radial direction. For a certain epoch, the distance from the Earth's center to the lunar lander, which is calculated with JPL ephemeris and a priori coordinates of the lunar lander, is fixed as the a priori value. The distance between the lunar lander and the Earth center as a constraint in radial direction is:

$$|\boldsymbol{r}_{LE}| = |\boldsymbol{r}_{LE0}| \tag{5.26}$$

where $|\boldsymbol{r}_{LE}|$ is corresponding to the distance between the lunar lander and the Earth center at a certain epoch, and $|\boldsymbol{r}_{LE0}|$ is the a priori value obtained from ephemeris and a priori coordinates of the lunar lander.

Linearizing eq. 5.26 with a Taylor series expansion, we can write

$$\frac{x_{LE0}}{|\boldsymbol{r}_{LE0}|} dx + \frac{y_{LE0}}{|\boldsymbol{r}_{LE0}|} dy + \frac{z_{LE0}}{|\boldsymbol{r}_{LE0}|} dz = 0 \tag{5.27}$$

where x_{LE0}, y_{LE0} and z_{LE0} are the a priori vector components from the Earth center to the lunar lander in the PA system at a certain epoch obtained from the ephemeris and the a priori coordinates of the lunar lander. dx, dy and dz are the estimated parameter corrections to the a priori values.

Constraint 2

The distance between the lunar lander and the Moon center is a fixed distance on the Moon. Using the distance between the lunar lander and the Moon center as a constraint, we can write:

$$\sqrt{(x_L)^2 + (y_L)^2 + (z_L)^2} = \sqrt{(x_0)^2 + (y_0)^2 + (z_0)^2} \tag{5.28}$$

where x_L, y_L and z_L are the coordinates of the lunar lander in the PA system. x_0, y_0 and z_0 are the a priori coordinates of the lunar lander in the PA system.

Linearizing eq. 5.28 with a Taylor series expansion, we find

$$\frac{x_0}{\sqrt{(x_0)^2 + (y_0)^2 + (z_0)^2}} dx + \frac{y_0}{\sqrt{(x_0)^2 + (y_0)^2 + (z_0)^2}} dy + \frac{z_0}{\sqrt{(x_0)^2 + (y_0)^2 + (z_0)^2}} dz = 0 \tag{5.29}$$

Constraint 3

Using the altitude of the lunar lander in the PA system as a constraint, and estimate the parameters latitude and longitude is the third type of constraint.

$$H_L = H_0 \tag{5.30}$$

where H_L is the altitude of the lunar lander on the lunar surface; H_0 is the a priori altitude of the lunar lander on the lunar surface by LRO. And both of these two altitudes are based on that the Moon is a sphere with radius of 1737.4 km.

What should be noted is that for the latitude and longitude estimated parameters, the corresponding partial derivatives are different and should be recalculated with the relationships as:

$$x = (R + H)cos\varphi cos\lambda \tag{5.31}$$
$$y = (R + H)cos\varphi sin\lambda \tag{5.32}$$
$$z = (R(1 - f) + H)sin\varphi \tag{5.33}$$
$$R = a/\sqrt{1 - fsin^2\varphi} \tag{5.34}$$
$$\frac{\partial \tau}{\partial(sin\varphi, sin\lambda)} = \frac{\partial \tau}{\partial \boldsymbol{X}} \frac{\partial \boldsymbol{X}}{\partial(sin\varphi, sin\lambda)} \tag{5.35}$$

where f is the oblateness factor of the Moon; a is the semi-major axis of the Moon; φ, λ and H are latitude, longitude and altitude of the lunar lander; x, y and z are the Cartesian coordinates of the lunar lander; R is the radius of the Moon.

With these derivations, the relationships between the Cartesian and the geodetic coordinates are obtained as:

$$\begin{pmatrix} dx \\ dy \\ dz \end{pmatrix} = \begin{pmatrix} -xz/\sqrt{(x^2 + y^2)} & -y & x/(R + H) \\ -yz/\sqrt{(x^2 + y^2)} & x & y/(R + H) \\ \epsilon * \sqrt{(x^2 + y^2)} & 0 & z/(R + H) \end{pmatrix} \begin{pmatrix} d\varphi \\ d\lambda \\ dH \end{pmatrix} \tag{5.36}$$

where $d\varphi$, $d\lambda$ and dH are the estimated parameter corrections to the a priori values. ϵ is $(1 - Rf/(R+H))$. If the oblateness factor is set to 0, then $\epsilon = 1$.

To avoid a singularity problem during the calculations, two components in trigonometric functions formats of latitude and longitude are used as the estimated parameters corrections, specifically $dsin\varphi$ and $dsin\lambda$. The relationships between $dsin\varphi$, $dsin\lambda$ and $d\varphi$, $d\lambda$ are easily derived.

We performed a number of tests with least-squares adjustment using the different constraints and found only insignificant differences in the results. The reason is that the same coordinates of the lunar lander are used in each equation, although the constraint equations are based on different geometric relationships. In the analysis, the three are almost equivalent. In our analysis, the second constraint is used, as it is a simple and direct way.

6. OCEL session description

In 2013, the Chang'E-3 landing module was deployed on the Moon successfully. Considering that the lander is equipped with a radio frequency transmitter at X-band, a project called *Observing the Chang'E-3 Lander with VLBI* (OCEL) was initiated. Since the transmitter emits a faint modulated signal, which can be detected on the Earth by geodetic radio telescopes, joint VLBI observations of the Lander and of natural compact extra-galactic radio sources (mostly quasars) were envisaged [Haas et al., 2016]. Following an observing proposals to the Observing Program Committee (OPC) of the International VLBI Service for Geodesy and Astrometry, four 24 h observing sessions each in the three years of 2014 to 2016 were scheduled with subsets of the IVS observing network.

OCEL Sessions											
01	02	03	04	05	06	07	08	09	10	11	12
Bd	Bd	Bd	-	Bd	Bd	Bd	Bd	Bd	Bd	Bd	Bd
-	-	-	-	Ft	Ft	-	Ft	Ft	Ft	Ft	Ft
Hh	Hh	-	-	Hh	Hh	Hh	-	Hh	Hh	Hh	Hh
Ho	-	Ho	Ho	Ho	Ho	Ho	Ho	Ho	Ho	Ho	Ho
-	-	Ht	Ht	-	-	-	Ht	-	-	-	-
-	-	-	Kk	Kk	Kk	Kk	Kk	Kk	-	Kk	Kk
-	-	-	-	-	-	-	-	-	-	Km	-
-	Ma	Ma	Ma	Ma	Ma	Ma	Ma	Ma	-	-	Ma
-	-	-	-	-	-	-	-	-	Mc	Mc	-
Ny	Ny	Ny	Ny	Ny	Ny	Ny	Ny	Ny	Ny	Ny	Ny
On	-	-	-	On	On	On	On	On	-	On	On
Sh	Sh	Sh	-	Sh	Sh	-	-	-	Sh	-	-
-	Ur	Ur	Ur	-	-	-	-	-	Ur	Ur	Ur
Wz	Wz	Wz	Wz	Wz	Wz	Wz	Wz	Wz	Wz	Wz	Wz
Zc	Zc	Zc		Zc	Zc	Zc	Zc	Zc	Zc	Zc	Zc
number of participating stations											
8	8	9	7	11	11	9	10	10	10	12	11

Table 6.1: Overview of the stations participating in the 12 OCEL sessions observed in 2014 through 2016. The IVS 2-character station abbreviations are used to indicate the individual stations: Bd – (Badary 32 m), Ft – (Fortaleza 14.2 m), Hh – (HartRAO 26 m), Ho – (Hobart 26 m), Ht – (HartRAO 15 m), Kk – (Kokee Park 20 m), Km – (Kunming 40 m), Ma – (Matera 20 m), Mc – (Medicina 32 m), Ny – (Ny-Ålesund 20 m), On – (Onsala 20 m), Sh – (Shanghai 25 m), Ur – (Urumqi 25 m), Wz – (Wettzell 20 m), Zc – (Zelenchukskaya 32 m). [Haas et al., 2016]

In tab. 6.1, the global IVS stations participating in the 12 OCEL sessions in 2014 through 2016 are listed. The stations distribute densely in Europe and Asia and there are also four stations on other continents (Fig. 6.1).

6.1 Observation Mode

As we described in Sec. 3.7, a sequence of QSQ or SQS is used in normal Delta-DOR observations. This is also applied in OCEL in a similar way. In a single OCEL session, three sorts of observation modes were conducted, which are lunar lander observations, delay-referencing quasar observations and common geodetic quasar observations. The last two groups differ by the selection of sources and by the frequency setup. In Fig. 6.2, the small blocks are the lunar lander observations and the delay-referencing observations, and the
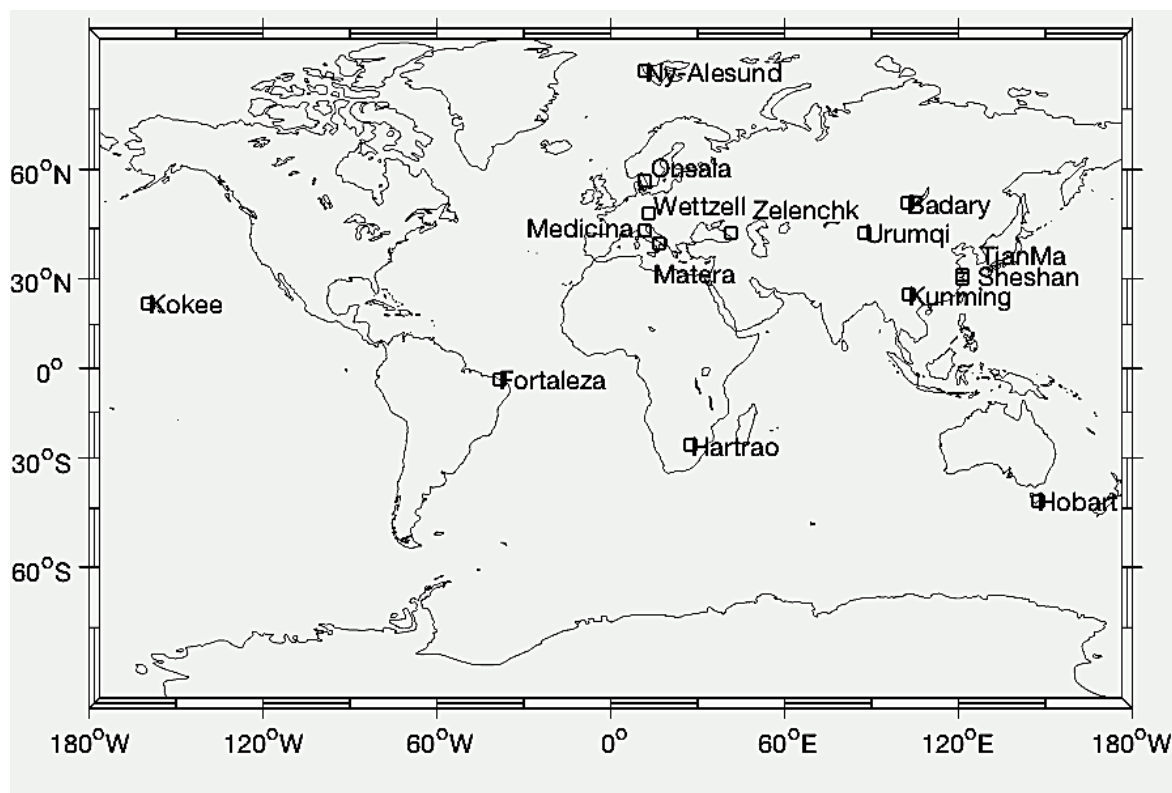
Figure 6.1: Global stations participated in OCEL sessions.

larger blocks are the geodetic observations. The lunar lander observations and the delay-referencing quasar observations are in blocks of primarily half an hour length. The targets of delay-referencing observations are radio sources nearby the lunar lander in terms of angular separation, usually a few degrees of arc length.

In Fig. 6.3, the sky plot of station Ny-Ålesund observing the lunar lander and reference quasars in OCEL-09 is shown. The red points are the positions of the lunar lander, and the others are reference quasars. In Fig. 6.4, the position and motion of the lunar lander and the reference quasars observed at the station of Onsala in OCEL-09 are depicted. The red points stand for the positions of the lunar lander while asterisks depict the reference quasars. From Fig. 6.4, we find a series of positions of the lunar lander corresponding to the respective epochs, while the quasars are fixed. The dotted cycles are radii of two degrees around the center points of each position of the lunar lander. By these cycles, we can identify individual reference quasars close to the lunar lander at different epochs and use them in the schedule as calibrators.

Initially, the lunar lander was not sending the DOR signal all the time during the full 24 hours of a session to avoid overheating the transmitter [Haas et al., 2016]. Therefore, there were some intervals without lunar signal where only common geodetic observations were scheduled. These correspond to the larger blocks in Fig. 6.2.

6.2   Frequency Setup

Due to having different observation modes, the frequency setup for the OCEL sessions differs within each session. The frequency for the lunar observations need to cover the five DOR tones listed above. For referencing purposes, the delay-referencing observations need the same frequency setup as the lunar lander
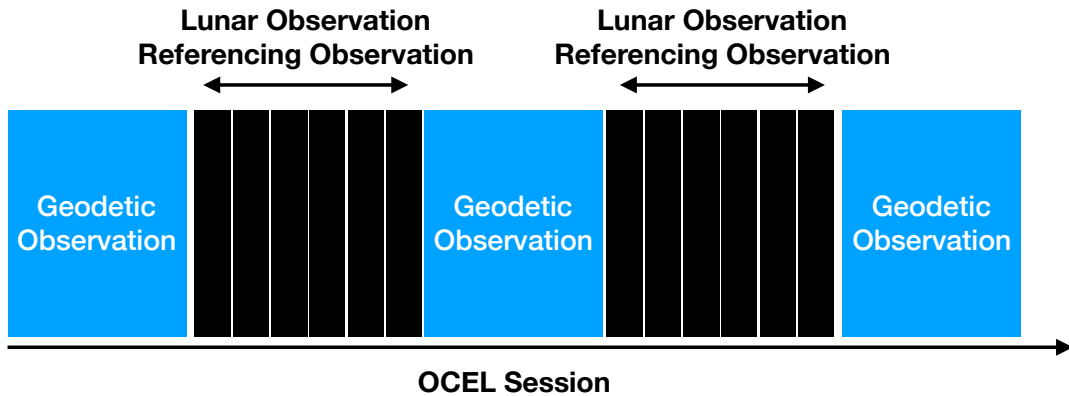
Figure 6.2: A schematic diagram of observation mode in an OCEL session.
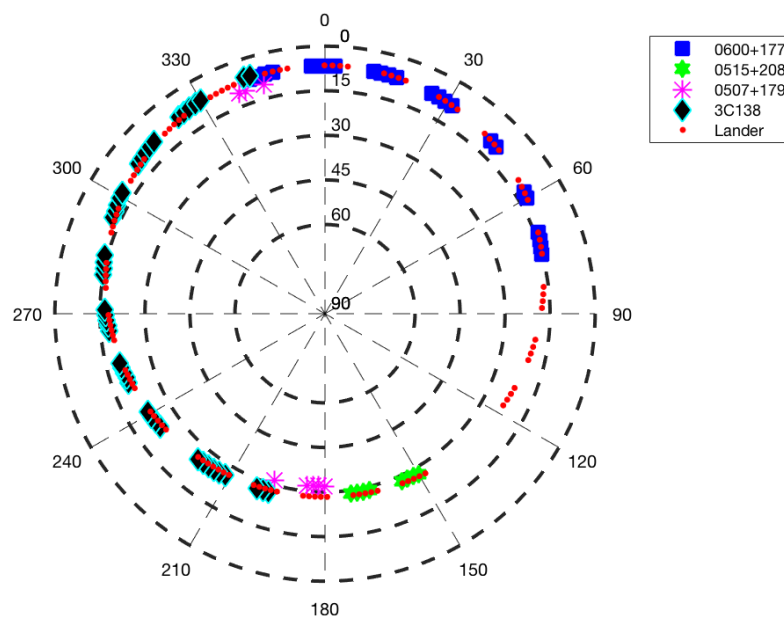
Figure 6.3: A sky plot of the station Ny-Ålesund observing the lunar lander and related quasars in OCEL-09.

observations. The geodetic observations have standard geodetic frequency setup. Besides that, the frequency setups between the different OCEL sessions also varied, for the reason that a number of different setups have been used for test. The detailed frequency setups of the OCEL sessions are listed in tab. 6.2 while the frequencies of the DOR tones of the lunar lander are presented in tab. 6.3.

In the first OCEL session a standard wide-band setup with 8 MHz channel bandwidth was planned for the geodetic observations. A special narrow-band frequency setup with also 8 MHz bandwidth aiming at the DOR-tones was planned for the delay-referencing observations and the lunar lander observations. In the second and third OCEL sessions, the frequency setup was changed to use 4 MHz bandwidths per channel for all the three observation modes. While in OCEL-04 session, the bandwidth switched from 4 MHz back to 8 MHz and a frequency setup similiar to OCEL-01 was planned. From OCEL-05 to OCEL-09, the bandwidth per channel for the geodetic observations was planned as 8 MHz and for the delay-referencing observations and the lunar lander observations were 4 MHz. In OCEL-10, the bandwidth per channel for the geodetic observations was changed to 4 MHz. In the last two session OCEL-11 and OCEL-12, a special narrow-band
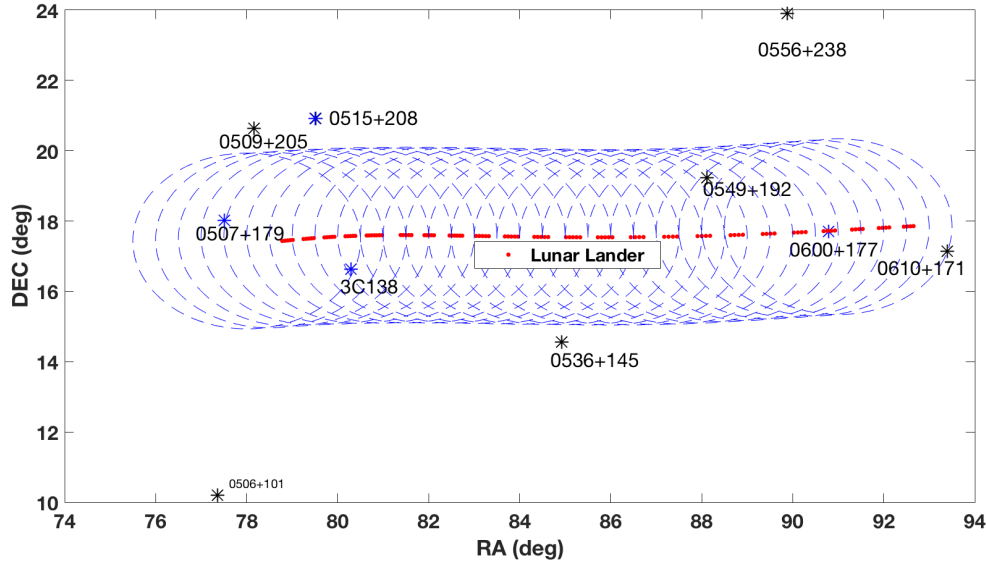
Figure 6.4: The position and motion of the lunar lander and reference quasars observed at the station of Onsala in OCEL-09.

OCEL	CH01	CH02	CH03	CH04	CH05	CH06	CH07	CH08
01	8212.99	8252.99	8465.99	8491.99	8446.99	8461.99	8465.99	8485.99
02	8448.99	8463.99	8467.99	8471.99	8486.99	8493.99	8468.99	8494.99
03	8466.99	8492.99	8448.99	8463.99	8467.99	8471.99	8486.99	8497.99
04	8212.99	8252.99	8446.99	8461.99	8465.99	8469.99	8484.99	8491.99
05	8212.99	8252.99	8448.75	8464.15	8468.00	8471.85	8487.25	8492.00
06	8212.99	8252.99	8448.75	8464.15	8468.00	8471.85	8487.25	8492.00
07	8212.99	8252.99	8448.75	8464.15	8468.00	8471.85	8487.25	8492.00
08	8212.99	8252.99	8448.75	8464.15	8468.00	8471.85	8487.25	8492.00
09	8212.99	8252.99	8448.75	8464.15	8468.00	8471.85	8487.25	8491.10
10	8212.99	8252.99	8448.75	8464.15	8468.00	8471.85	8487.25	8491.10
11	8210.05	8221.60	8448.75	8464.15	8468.00	8471.85	8487.25	8568.10
12	8210.05	8221.60	8448.75	8464.15	8468.00	8471.85	8487.25	8568.10

Table 6.2: Frequency allocations for delay-referencing and lunar lander observations, upper sideband. In most sessions Ch. 3 - 7 cover the DOR tones exactly (center frequency), shaded if channels do not match the DOR tone sequence.

frequency setup was used and a 4 MHz bandwidth per channel was used for all the three observation modes. As for the phase-cal, from OCEL-05 to OCEL-07, the phase-cal was switched off and for other OCEL sessions the phase-cal was active.

DOR tones	DOR 1	DOR 2	DOR 3	DOR 4	DOR 5
Frequency	8450.75	8466.15	8470.00	8473.85	8489.25

Table 6.3: Frequencies of the DOR tones of the lunar lander.
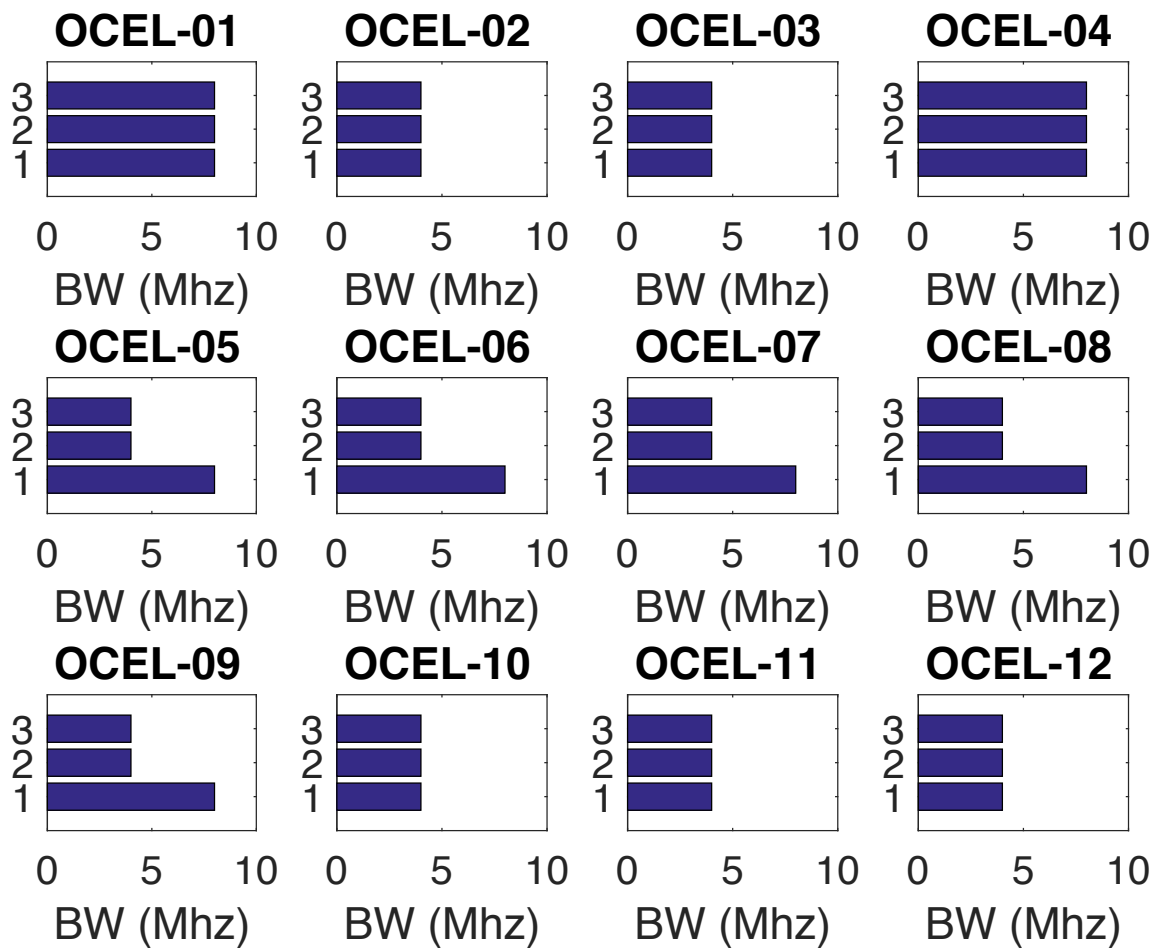
Figure 6.5: Frequency bandwidth setup of OCEL sessions. Ylabel (1/2/3) with 1 for the geodetic observations, 2 for the delay-referencing observations and 3 for the lunar lander observations.

7. Fringe-fitting of the OCEL sessions

7.1   Initial investigations

Starting with the considerations that we want to include all channels of the frequency setup, when we observe quasars, we transfer this to the DOR frequency setup and select all five DOR tone channels for the initial fringe fitting. For this we used the fringe-fitting program PIMA for its helpful diagnosis tools. So, for the first test, we used the five channels (8448.75 MHz, 8464.15 MHz, 8468.00 MHz, 8471.85MHz, 8487.25MHz) recorded for the Chang'E-3 lunar lander and delay referencing sources. In the amplitude part of the power spectrum (Fig. 7.1(b)), the lander's DOR tones appear as sharp peaks with the 3rd peak corresponding to the carrier frequency having by far the largest signal strength. Looking at the 3D delay resolution function for this setup (Fig. 7.3), we see that it displays a smooth wave form of a series of maxima. This suggests that the final group delay determination becomes rather uncertain and unreliable. In a series of tests with other baselines, we have the same behavior with this setup. It should be noted that from Fig. 7.1 and 7.2 the signal strength of the lunar lander is much higher than that of the quasar. Besides that, from the fringe amplitude it a proof that there is a great difference between the signal of the lunar lander and the quasar.
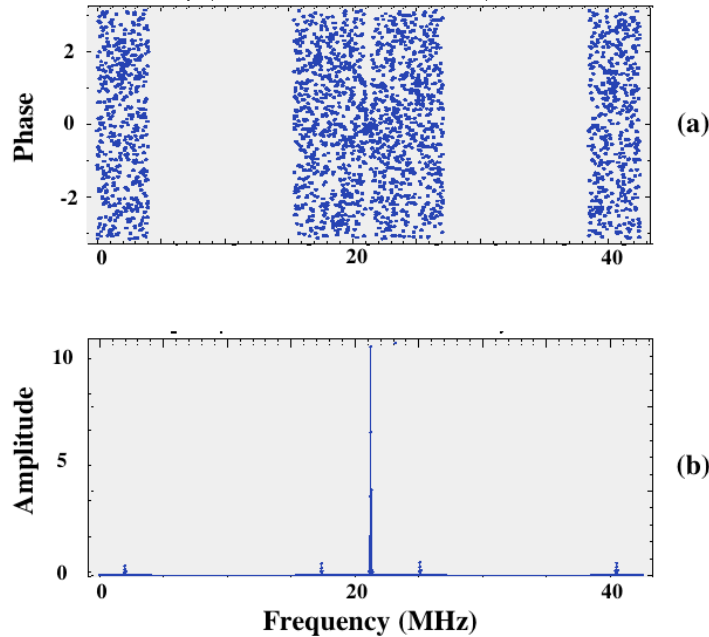
Figure 7.1: The phase and amplitude of fringe with five channels. a) X-band fringe phase w.r.t frequency for the Chang'E-3 lunar lander at baseline BD-NY in OCEL-09; b) X-band fringe amplitude w.r.t frequency for the Chang'E-3 lunar lander at baseline BD-NY in OCEL-09.

To find the reason, we performed a series of tests with different combinations. We discovered that the tone on the carrier frequency is responsible for this adverse behavior. If the frequency channel of the carrier is included, the delay resolution function would be rather smooth while with other combinations an apparent peak could be found. Most probably it is the much higher strength of the tone on the carrier frequency causing the increased intensity of this channel which leads to an awkward delay resolution function for

group delay determination. After these investigations, we decided to drop the carrier channel.
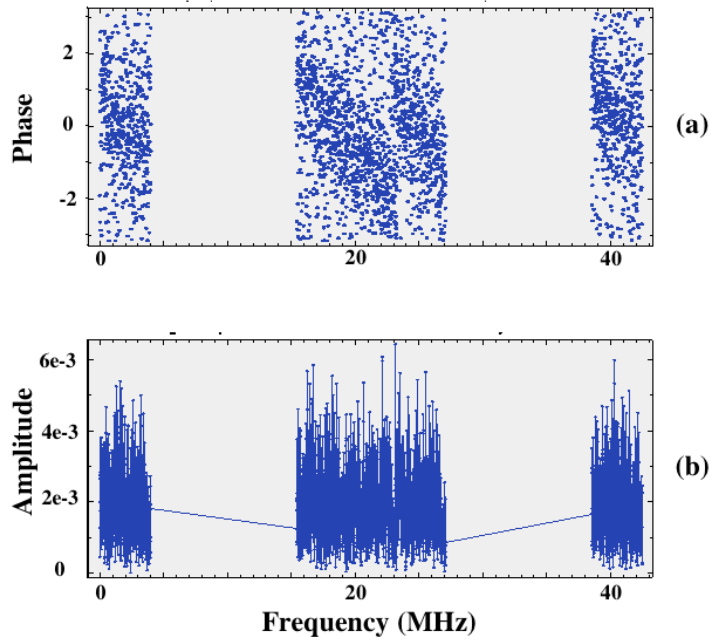
Figure 7.2: The phase and amplitude of fringe with five channels. a) X-band fringe phase w.r.t frequency for quasar at baseline BD-NY in OCEL-09; b) X-band fringe amplitude w.r.t frequency for quasar at baseline BD-NY in OCEL-09.
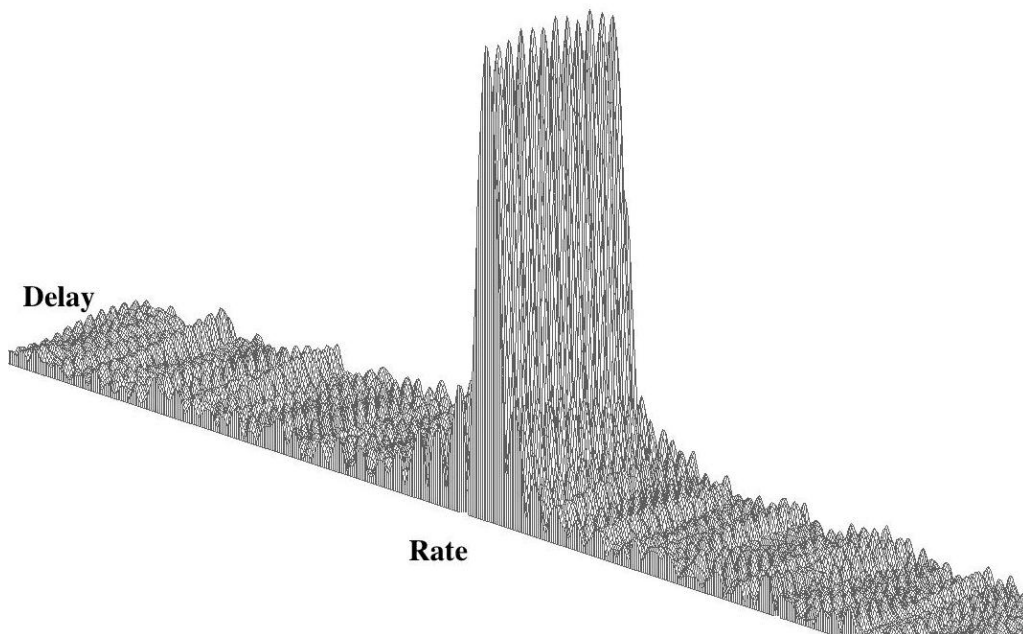
Figure 7.3: Delay resolution function for the Chang'E-3 lunar lander at baseline BD-NY in OCEL-09.

7.2 Closure Delay Tests

Fringe fitting can be performed in multiple ways with no clear indicator of which settings are the best. However, for our further investigations we have chosen delay triangle closures as a good indicator for the quality of the fringe fit. With this, we have selected the individual processing steps described below.

The closure delay is defined as the sum of the group delays around a closed triangle of baselines. It is a direct, reliable and important criterion to evaluate the quality of observations and to determine the measurement noise in geodetic VLBI (e.g., [Alef & Porcas, 1986; Liu et al., 2010; Ming & Qinghui, 2010]).

Normally, for a triangle of three stations, A, B and C, the triangle closure delay is defined for an individual wavefront by:

$$\tau_{ABC} = \tau_{AB} + \tau_{BC} + \tau_{CA} \tag{7.1}$$

where τ_{AB} is the delay observable from station A to station B, τ_{BC} is the delay observable from station B to station C, and τ_{CA} is the delay observable from station C to station A (Fig. 7.4). The latter is equivalent to $-\tau_{AC}$. Then we have the closure delay as:

$$\tau_{ABC} = \tau_{AB} + \tau_{BC} - \tau_{AC} \tag{7.2}$$
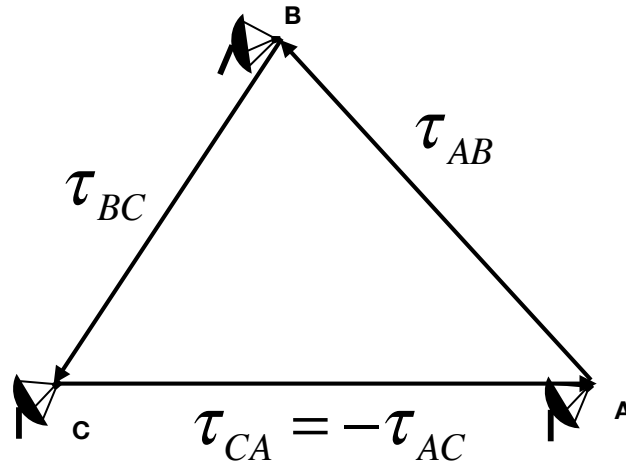
Figure 7.4: Schematic diagram of triangle closure delay.

In geodetic VLBI measurements, the group delay observables are usually referred to the epoch when the wavefront passes the first station of the baseline. These group delays are named as first-station referenced group delays or baseline-based group delays. The delays in Eq. 7.2 are geocentric group delays, which were introduced in Sec. 3.1. The triangle closure delay τ_{ABC}, for an ideal point source and no observational noise, is independent of any station-based and source based effect and should be zero. However, due to measurement noise and other influences, the closure delay is usually not zero. It is a criterion to evaluate the measurements. It should be noted that an identical reference time for group delays is of importance. In this work, we use closure delay analysis to evaluate the group delay observables from different fringe-fitting tools and in a further step to select a proper fringe-fitting tool for the OCEL sessions.

7.3   Fringe-fitting Selection

As described above, the DOR signal is a narrow bandwidth signal different from that of quasars, which is the typical radio source for geodetic VLBI. In OCEL, the lunar lander and the quasars are observed together with the same radio telescopes, which usually observe quasars. Besides that, the processing pipeline for geodetic VLBI had only been set up for natural extra-galactic radio source observations. For this reason, in OCEL [Haas et al., 2016] the need for addressing the issue of processing DOR tone signals arose with several different frequency setups being applied.

In routine processing of quasar observations in geodetic VLBI, the software correlator DiFX together with the fringe-fitting program HOPS/$fourfit$ are widely used. DiFX does not have any problem dealing with signals from artificial sources since the raw data structure remains the same [Deller et al., 2007, 2011]. However, the program HOPS/$fourfit$ is not designed for DOR tone data.

It should be mentioned here that there are other means of dealing with narrow signals in broad channels such as filtering the cross-power spectrum for the narrow tone frequency bands. During correlation, extra processing with a special zoom-band mode in setting up the DiFX correlator may deal with narrow signals [Brisken, 2013; Deller et al., 2011; Hellerschmied et al., 2018]. However, with the purpose of keeping the correlator setup directly transferable from the setup in the schedule files, it was advisable to keep the original processing chain. So, this keeps the same processing pipeline as for routine geodetic VLBI data, with determination of the DOR tone spectrum only in the fringe-fitting process part. For these purposes, we adapted the algorithm for DOR tone signal processing in space navigation into the $fourfit$ program as $fourfit$-DOR, which was described in sec. 4.2.3.

In order to test the quality of the fringe-fitting process with $fourfit$ and $fourfit$-DOR, we computed all the triangle closures observed in OCEL-09 on Jan. 20th, 2016 firstly with the original $fourfit$ program (Fig. 7.5) and then with $fourfit$-DOR (Fig. 7.6). It should be noted that for the correlation process, the FFT resolution was set to 128 spectral channels (with parameter $nChan$) and the channels selected in fringe-fitting were the channels corresponding to the DOR tones except for the carrier tone (i.e., Ch. 3, 4, 6 and 7).

The observations cluster in blocks in the way as the observations have been scheduled [Haas et al., 2016]. In both plots (Fig. 7.5 and Fig. 7.6), there are obvious mis-closures of up to 20 ns, which dominate the whole plot of the closures. At the same time, in the right hand sub-plots, the histograms do not conform to the normal distribution, which also indicates that the mis-closures dominate the whole plot. These mis-closures seem to stem from some intermittent, rather systematic errors of yet unknown reasons. Since we could not identify any particular antenna or baseline responsible for the mis-closures or perform proper outlier tests, in order to obtain numbers of un-corrupted observations, the first five blocks of observations in both Fig. 7.5 and Fig. 7.6 are extracted. Fig. 7.7 and Fig. 7.8 are the corresponding closures of the first three blocks by $fourfit$ and $fourfit$-DOR, respectively. Now, the closures of the first five blocks come close to a normal distribution according to the histograms. Then, it is obvious that most of the closures from the $fourfit$-DOR processing are much smaller than those from $fourfit$. Besides that, the WRMS error of the closure delays reduces from 586 ps to 243 ps. In addition, other un-corrupted blocks show a very similar reduction in the WRMS error. These analyses suggest in a conclusive and convincing way that $fourfit$-DOR is superior to $fourfit$ for fringe-fitting the data of DOR tones embedded in MHz-wide channel recordings and direct correlation.

7.4   DOR Tones and Frequency Channels Selection

For the common quasar VLBI observations, usually all the frequency channels in one band (X-band or S-band) are included in the fringe-fitting processing, unless there is no signal in a frequency channel. As for the OCEL sessions with four narrow bandwidth DOR tones, besides the carrier, in X-band, the situation is
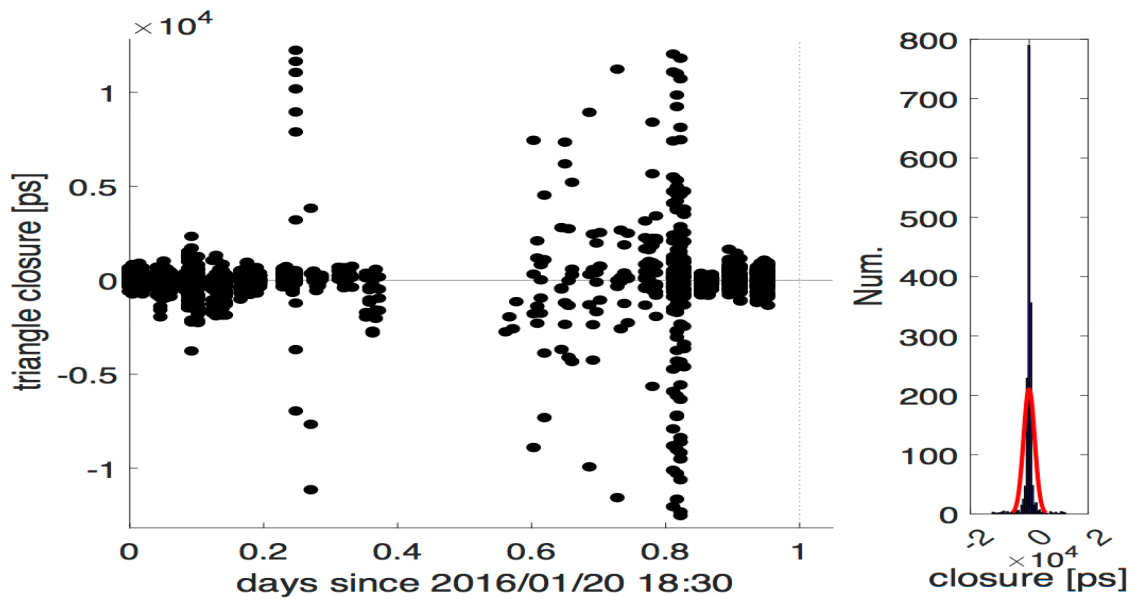
Figure 7.5: Delay triangle closures of all baselines in the OCEL-09 session with four frequency channels included and processed with the original $fourfit$ software. The red curve in the histogram plot on the right side is the respective normal distribution.
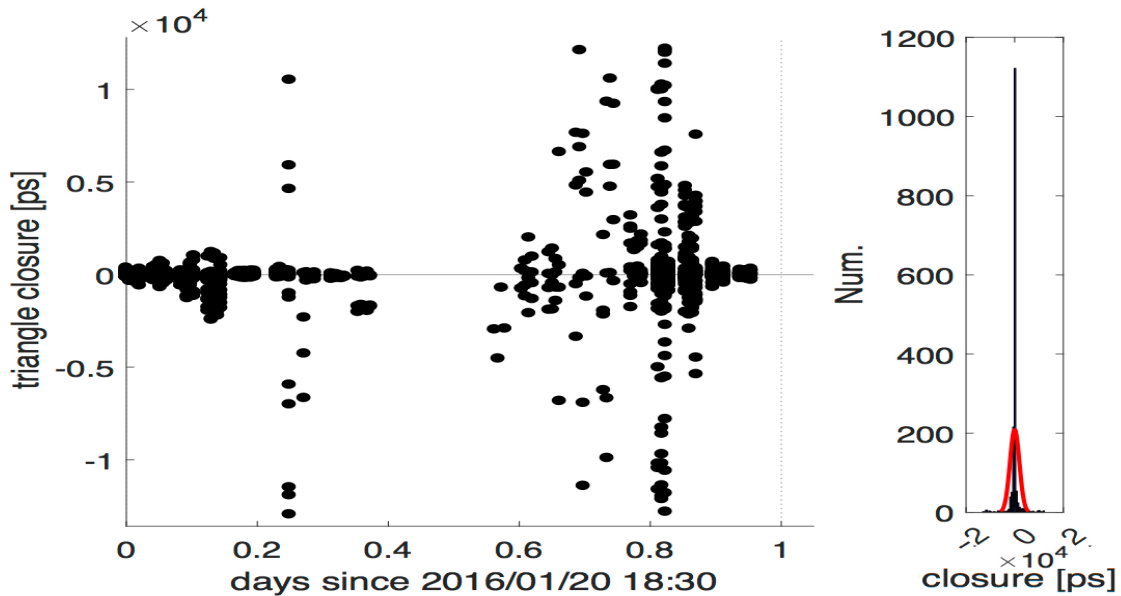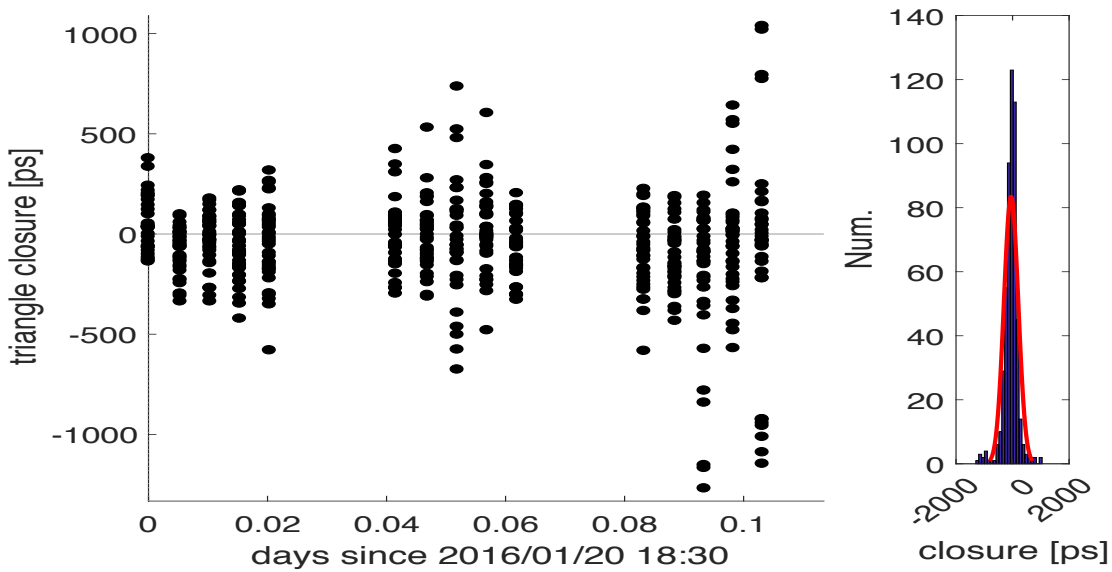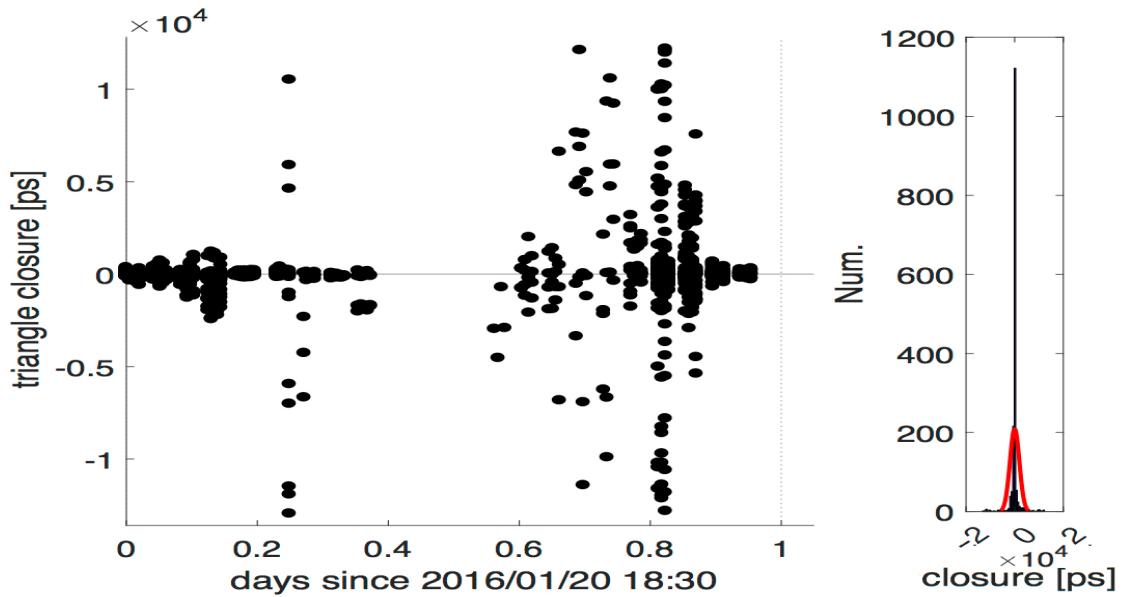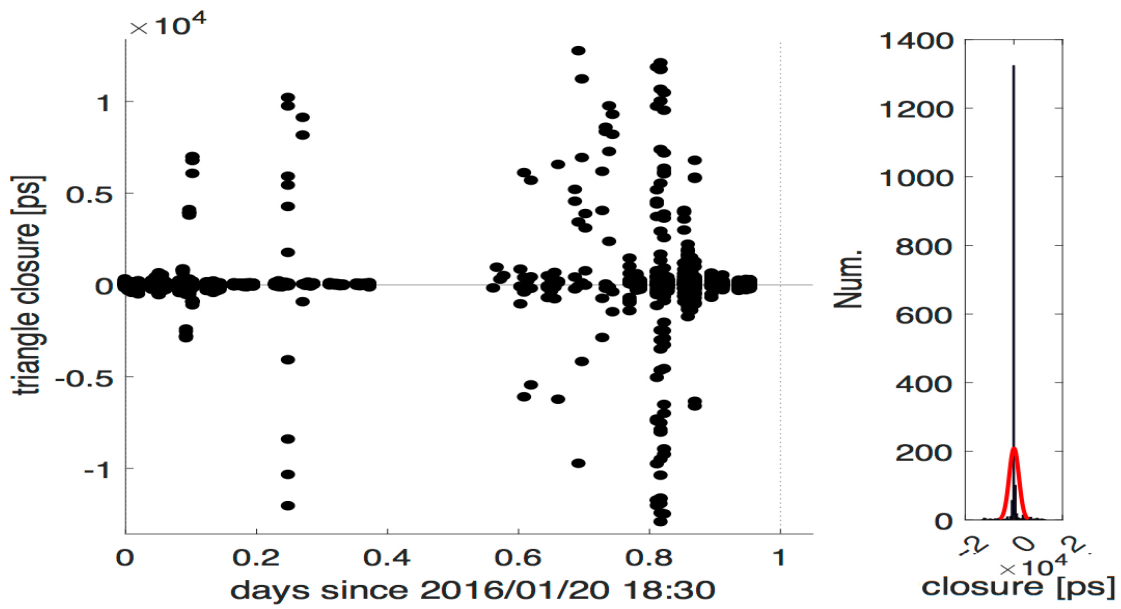

Figure 7.6: Delay triangle closures of all baselines in the OCEL-09 session with four frequency channels included and processed with the $fourfit$-DOR software. The red curve in the histogram plot on the right side is the respective normal distribution.

different from the common quasar signal. Therefore, it is of great importance to investigate which selection of frequency channels produces the best fringe-fitting results.
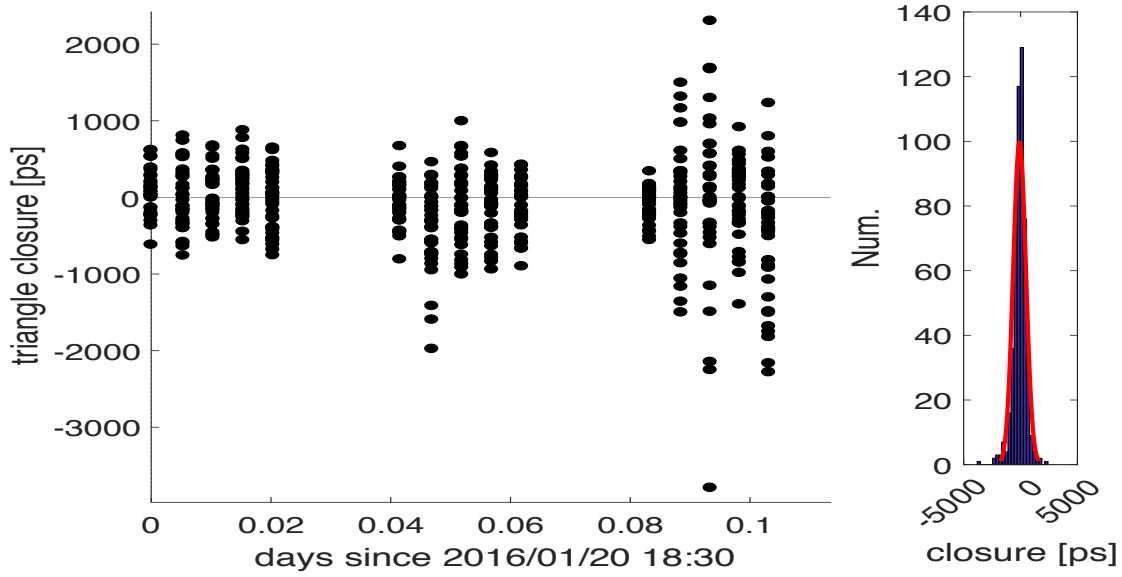
Figure 7.7: Delay triangle closures of first three blocks observations in the OCEL-09 session with four frequency channels included in the processing with the original *fourfit* software. The red curve in the histogram plot on the right side is the respective normal distribution.

Figure 7.8: Delay triangle closures of first three blocks observations in the OCEL-09 session with four frequency channels included in the processing with the *fourfit*-DOR software. The red curve in the histogram plot on the right side is the respective normal distribution.

To make a full analysis of the DOR tone selection (corresponding to the frequency channels), all tested combinations of DOR tones are listed in Table 7.1. According to the basic theory of group delay determination and Eq. 3.8, the group delay is determined by the slope of phase over frequency, for this reason at least two tones are necessary. With all the combinations of the DOR tones, we find the proper one for the OCEL

sessions to obtain more reliable group delays.

Num. of Tones	Combinations
4	(1,2,4,5)
3	(1,2,4) (1,4,5) (1,2,5) (2,4,5)
2	(1,2) (1,4) (1,5) (2,4) (2,5) (4,5)

Table 7.1: Combinations of four DOR tones. The column in left is the number of the DOR tones included and the column on the right contains the corresponding combinations of these tones. The figures between parentheses stand for the number of tones and each pair of parentheses contains one combination.

Figure 7.9: Delay triangle closures of all baselines in the OCEL-09 session with four frequencies channels included, which are corresponding to the 1st, 2nd, 4th and 5th DOR tones. The red curve in the histogram plot on the right side is the respective normal distribution.

According to the basic theory of the DOR tone fringe-fitting (in Sec. 3.7), the larger the frequency spacing between frequency channels, the more accurate the group delay will be. Therefore, the two outermost frequency channels corresponding to the 1st and 5th DOR tones should be included in the delay determination. Besides that, as discussed above, if the a priori delay model is not accurate enough, more than two frequency channels are needed for the resolution of ambiguities.

In Fig. 7.10, the triangle closures of all baselines in the OCEL-09 session with the 1st and 5th DOR tones are shown. Compared with Fig. 7.9, which is fringe-fitted with the 1st, 2nd, 4th and 5th DOR tones, the closures of two frequency channels are slightly larger. However, it can not be found whether there are ambiguities from these plots. Then we compared the group delays of two and four frequency channels as shown in Fig. 7.11. The figure shows the apparent differences at about ±25.9 ns, which is corresponding to the frequency spacing between the channels containing the 1st and 5th DOR tones. It indicates that the a priori delay model is not accurate enough and if only the outermost frequency channels are selected in

Figure 7.10: Delay triangle closures of all baselines in the OCEL-09 session with two frequency channels included, which are corresponding to the 1st and 5th DOR tones. The red curve in the histogram plot on the right side is the respective normal distribution.
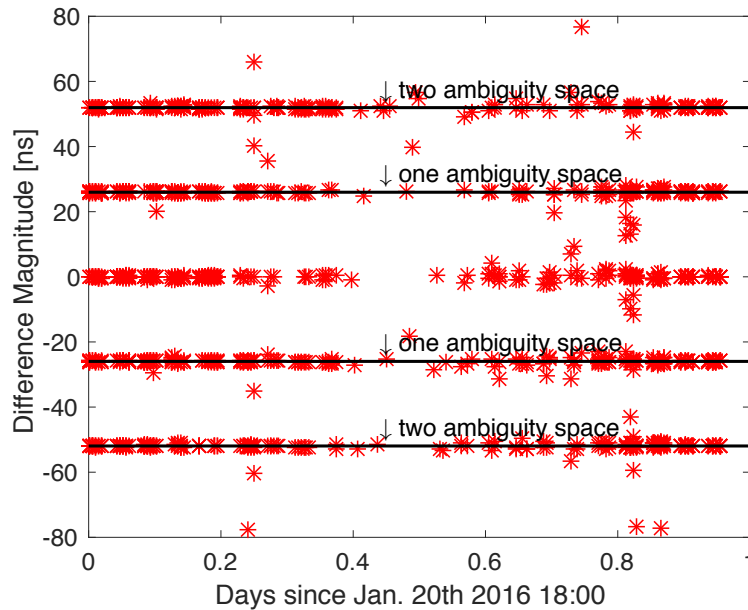
Figure 7.11: Differences between the group delays of all baselines in the OCEL-09 session with two and four frequency channels, corresponding to the results with the 1st/5th DOR tones minus that with the 1st/2nd/4th/5th DOR tones.

fringe-fitting, the ambiguities show up. Therefore, we need to select more frequency channels in fringe-fitting. As for whether to include two inner frequency channels corresponding to the 2nd and 4th DOR tones or only include one of them, we performed a number of tests and found out that including both of the inner frequency channels is sightly better in triangle closures than only including one of them. Besides that,

including both of the inner frequency channels increases the SNR and the reliability of the results.

As a summary, according to the results and discussions, the frequency combination of the 1st, 2nd, 4th and 5th channel is the most suitable choice for the fringe-fitting of the OCEL sessions.

7.5   FFT Resolution Selection

As discussed above, proper FFT resolution reflected by the number of channels per spectral window has to be set in the correlation process for optimal fringe fitting. We performed an analysis and found out a proper number of channels per spectral window for the OCEL sessions in this section.

As mentioned in Sec. 3.1, the parameter $nChan$ is the number of channels per spectral window, which is set in the $.v2d$ control file for correlation. Since $nChan$ must be a number of 2^n, the $nChan$ of 32, 64, 128 or 256 can be used in the correlation. It should be noted that the $nChan$ of 32, 64, 128 and 256 are corresponding to the number of correlated frequency lags of 64, 128, 256 and 512.

To find the relationship between FFT resolution and group delay accuracy, and to select the best FFT resolution for correlation, the OCEL-09 session was correlated with a series of different FFT resolutions ($nChan = 32, 64, 128, 256$), fringe-fitted with $fourfit$-DOR and the group delays are analyzed.
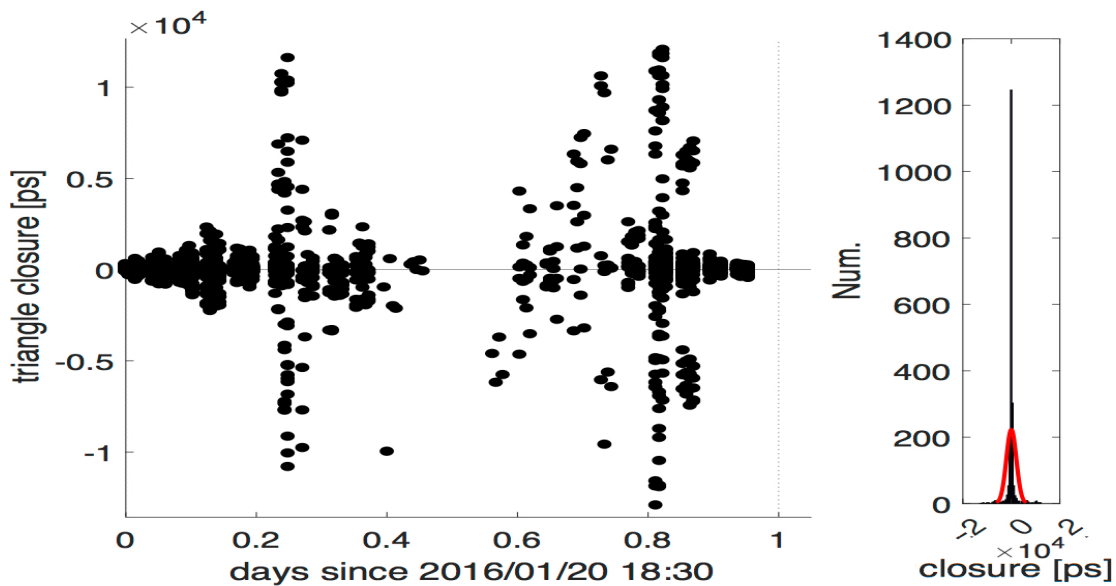
Figure 7.12: Delay triangle closures of all baselines in the OCEL-09 session with the $nChan$ parameter of 32 in correlation. The red curve in the histogram plot on the right side is the respective normal distribution.

In the left plot of Fig. 7.12, the observations of the lunar lander are again distributed in blocks w.r.t time, which agrees with the observation schedule. The plot is dominated by large mis-closures of up to 10 ns, and it is also indicated by the histograms not meeting the normal distribution. However, the majority of the triangle closures fits at the level of roughly 1~2 ns. This behavior happens in all cases with different $nChan$ parameters set for the correlation. In order to obtain numbers of data which are not corrupted by the large mis-closures, we take the 1st, 2nd, 3rd, and 5th block out of all observations and compare the results of different $nChan$ parameters. As shown in fig 7.13, 7.14, 7.15 and 7.16, the triangle closures of the four blocks fit at the level of about 1 ns. Besides that, the histograms are close to normal distributions.
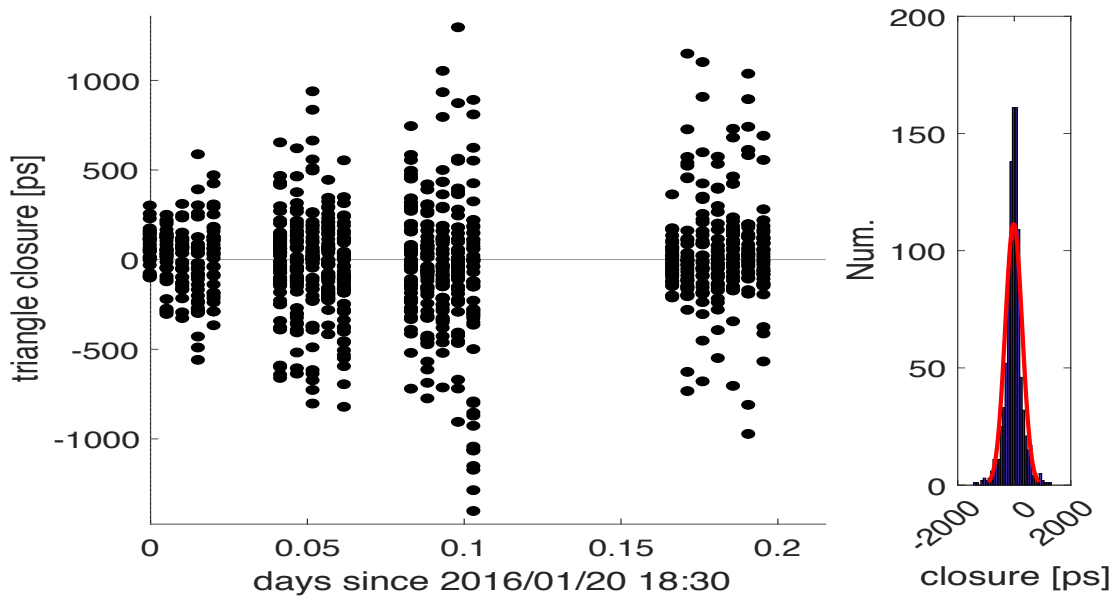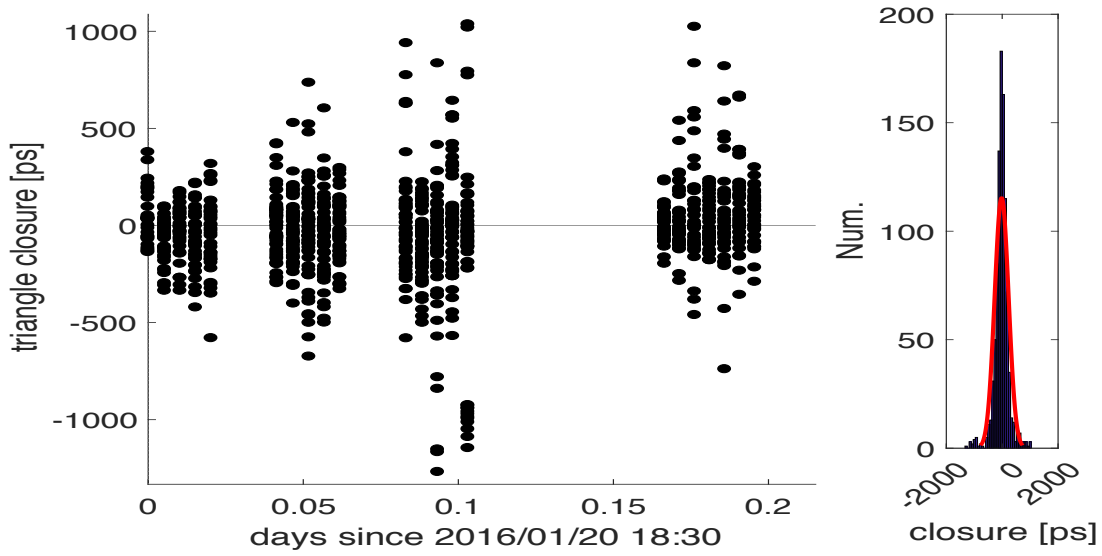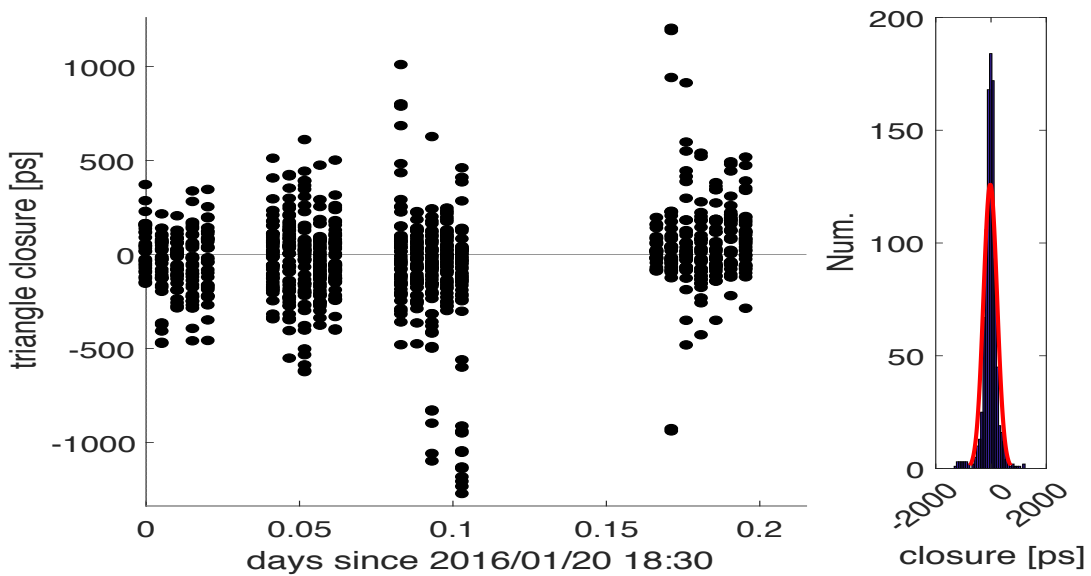
Figure 7.13: Delay triangle closures of four blocks in the OCEL-09 session with the *nChan* parameter of 32 in correlation. The red curve in the histogram plot on the right side is the respective normal distribution.
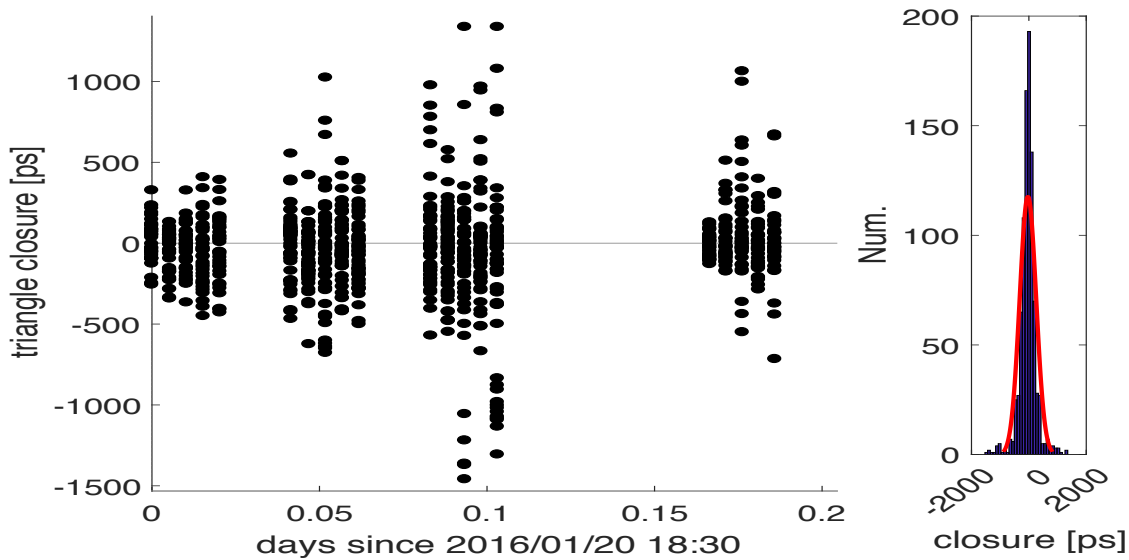
Figure 7.14: Delay triangle closures of four blocks in the OCEL-09 session with the *nChan* parameter of 64 in correlation. The red curve in the histogram plot on the right side is the respective normal distribution.

Looking at the delay triangle closures of four blocks in the OCEL-09 session with the *nChan* parameter of 32 shown in Fig. 7.13 and 64 in Fig. 7.14, there are obvious decreases of the triangle closures in each block from the case of the *nChan* parameter of 32 to 64. For instance, the triangle closures of the first block in Fig. 7.14 all stay in the range of ± 500 ps, while there are some triangle closures of the first block in Fig. 7.13 are larger than that. Similar things happened from the case of the *nChan* parameter of 64 to 128 (in Fig. 7.15). However, compared the cases of the *nChan* parameter of 128 and 256 (in Fig. 7.16), the

Figure 7.15: Delay triangle closures of four blocks in the OCEL-09 session with the *nChan* parameter of 128 in correlation. The red curve in the histogram plot on the right side is the respective normal distribution.

triangle closures are close. To investigate the influences of the *nChan* parameter on delay triangle closures, the standard deviations of the closure delays of 4 observation blocks in the OCEL-09 session with different *nChan* parameter setups are computed.

Figure 7.16: Delay triangle closures of four blocks in the OCEL-09 session with the *nChan* parameter of 256 in correlation. The red curve in the histogram plot on the right side is the respective normal distribution.

In Fig. 7.17, the standard deviations of the closure delays of 4 observation blocks in the OCEL-09 session with different *nChan* parameter setups are shown. Apparently there is a trend that the standard deviation of
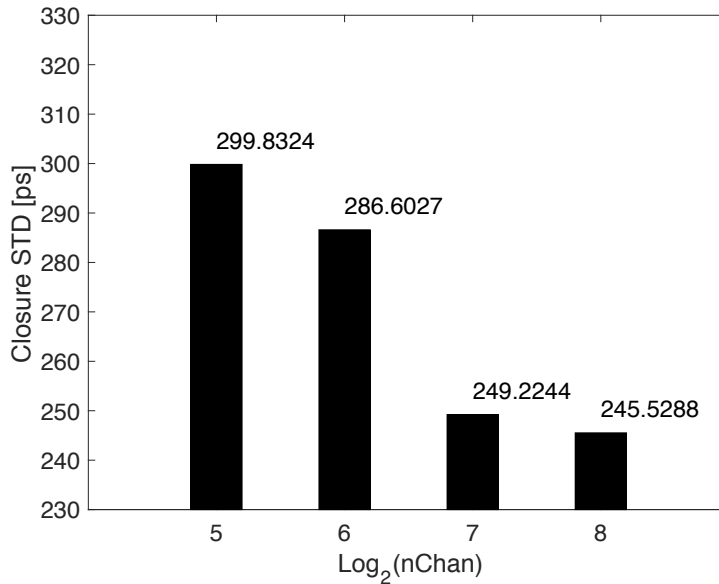
Figure 7.17: Closure delays standard deviations of 4 observation blocks in the OCEL-09 session with different *nChan* parameter setups, in which the y-axis is the closure delays standard deviations in ps and the x-axis is the logarithm of the *nChan* parameter to the base of 2, corresponding to the *nChan* parameter of 32, 64, 128 and 256 respectively.

the closure delays reduces with the *nChan* parameter number increasing. This agrees with the theory that a larger number of channels per spectral window is corresponding to a higher FFT resolution achieving higher accuracy. However, when the FFT resolution is high enough, further improvement of the accuracy of the group delay results is limited. As for increasing the *nChan* parameter number from 32 to 64, corresponding to the logarithm of 5 and 6 in, the standard derivation of the closure delays decreases by 13.2 ps from 299.8 ps to 286.6 ps. Increasing the *nChan* parameter number from 64 to 128 corresponds to a further decrease of the standard derivation by another 37.4 ps, while a further increase of the *nChan* parameter number from 128 to 256 only leads to an improvement of 3.7 ps in the standard derivation. This is one order of magnitude lower than the improvement of the *nChan* parameter number from 32 to 64 and from 64 to 128. Considering a closure delay is to evaluate the noise of the group delays involving three baselines, the results should be divided by a factor of $\sqrt{3}$ for the noise of a single baseline. Then the improvement for a single baseline is only $1 \sim 2$ ps when increasing the *nChan* parameter number from 128 to 256, which is insignificant for the analysis of the OCEL sessions.

The results suggest that 128 channels per spectral window are enough for the OCEL sessions and the improvement of the accuracy of the group delay results by a larger number of *nChan* parameter is limited and insignificant for the OCEL sessions. However, considering the 50.6 ps and 37.4 ps improvements from 32 and 64 to 128 channels per spectral window, choosing the *nChan* parameter number as 128 is absolutely necessary. Therefore, 128 channels per spectral window is suitable and selected for processing all OCEL sessions.

7.6 Summary of OCEL group delay determinations

In the OCEL project, there are totally twelve sessions from OCEL-01 to OCEL-12. The raw data of the OCEL sessions were correlated at the Max Planck Institute for Radio Astronomy (MPIfR) in Bonn, Germany. In the meantime, we also correlated the OCEL-05 to OCEL-09 sessions on a standalone Linux desktop PC for preliminary tests. There are no significant differences between the results from the standalone Linux desktop and the MPIfR correlator. To keep the correlations of all OCEL sessions consistent, we use the correlation

outputs from the MPIfR correlator for further calculations and analysis. As we discussed and analyzed above, the *nChan* parameter was set as 128 in *.v2d* file in correlation for both lunar and quasar data.

Since we do not use the geodetic observations in our analysis, only the delay-referencing observations and the lunar lander observations are fringe-fitted and analyzed. The correlation outputs are sorted in two groups for the delay-referencing scans and the lunar lander scans. The delay referencing scans were fringe-fitted with *fourfit* and the lunar lander scans were fringe-fitted with *fourfit*-DOR. It should be noted that the fringe-fitting results of the delay referencing observations from *fourfit* and *fourfit*-DOR are identical. In addition, the frequency channels applied in fringe-fitting are the four channels aiming at the 1st, 2nd, 4th and 5th DOR tones. PIMA was also used for checking the delay resolution function.
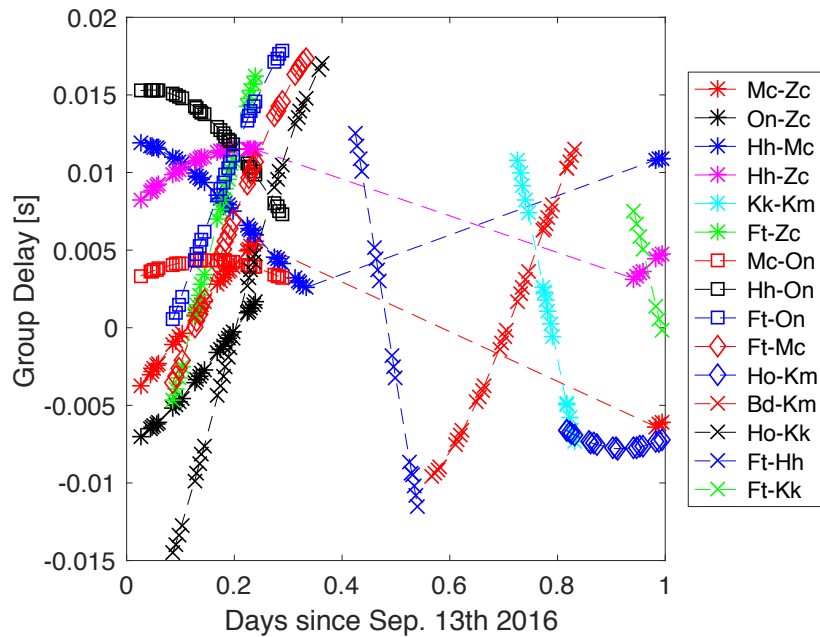
Figure 7.18: Results of group delay determination of the lunar lander observations of 16 baselines in the OCEL-11 session. The IVS 2-character station abbreviations are used to indicate the individual stations: Bd – (Badary 32 m), Ft – (Fortaleza 14.2 m), Hh – (HartRAO 26 m), Ho – (Hobart 26 m), Kk – (Kokee Park 20 m), Km – (Kunming 40 m), Mc – (Medicina 32 m), On – (Onsala 20 m), Zc – (Zelenchukskaya 32 m).

In Fig. 7.18, the group delays of the lunar lander observations from 16 baselines in OCEL-11 session are shown for demonstrating their magnitude. 437 out of 502 observations are depicted, the rest are observations from baselines with much fewer observations. The group delays of each baseline vary considerably due to the relative motion of the Moon and the antennas on Earth. In addition, atmospheric effects following the geometric change also contribute to the variations.

The residual group delays w.r.t. the a priori delay model used in the correlation of the 16 baselines in the OCEL-11 session are shown in fig 7.19. Most of the residual group delays have smooth and reasonable trends. However, for instance at the baseline of Ft-Hh, there are relatively large jumps even in short time periods. Theoretically, according to our fringe-fitting algorithm and software, ambiguities should not be present, but there may still be a chance of some of them being caused by a relatively low signal-to-noise ratio (SNR). In Fig. 7.20, the SNR of the lunar lander observations at the 16 baselines in OCEL-11 session are shown. We can find that the observations at the baseline of Ft-Hh have relatively low SNR (around 10), which indicates that this is probably the reason for the jumpy behaviour in Fig. 7.19. Similarly, we notice that for parts of the observations at the baselines of Ho-Kk and Ft-On, the observations have a low SNR level of around 10. Corresponding to that, the residual group delays of the observations at the baselines Ho-Kk and Ft-On have
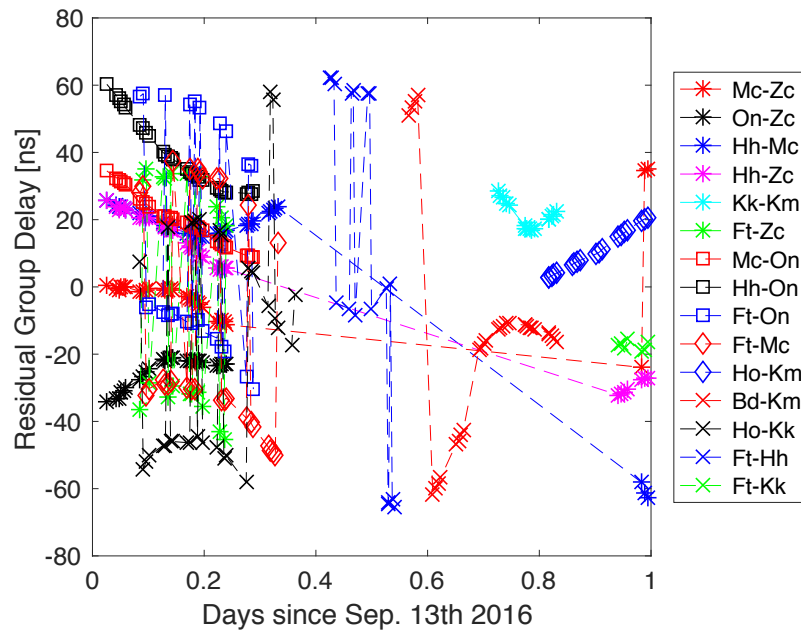
Figure 7.19: Results of residual group delay determination of the lunar lander observations w.r.t the a priori delay for correlation in OCEL-11 session. Residual group delays of 16 baselines from OCEL-11 are shown in plot.
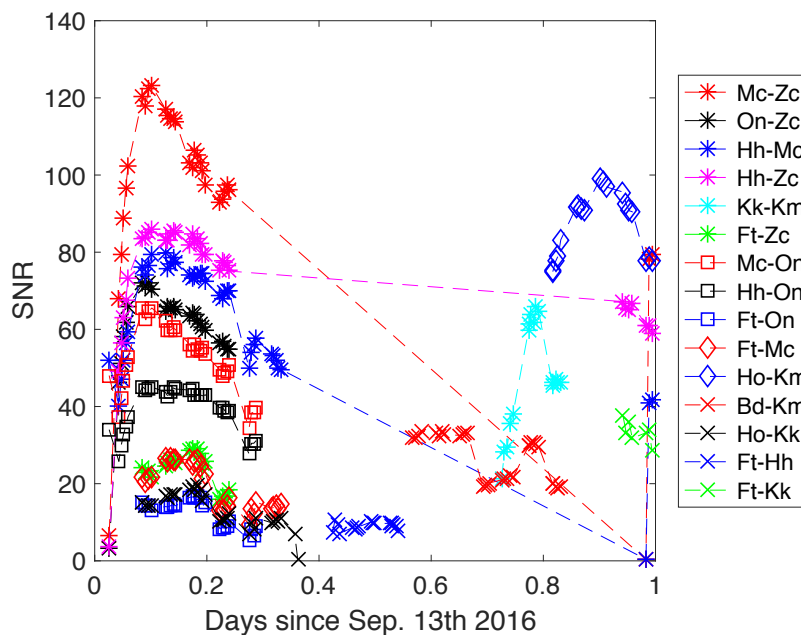

Figure 7.20: Signal-to-noise ratio of the lunar lander observations in OCEL-11 session. SNR of 16 baselines from OCEL-11 are shown in plot.

a similar behaviour that a number of residual group delays are in an arbitrary distribution instead of forming a trend shown in Fig. 7.19. For this reason, a SNR check is necessary for data reduction before analysis.

As described in Sec. 6, the ocel sessions differed mainly by the frequency setup and observing baselines distribution. But the observing mode and the observing devices remained the same. Therefore, the group delays from each session stayed at the same level of accuracy.

8. Estimation of the Chang'E-3 Lunar Lander Position with VLBI

With the observed group delays determined from OCEL and the theoretical model built up, the position estimation of the Chang'E-3 lunar lander was performed. In this section, the analysis setup and results are described and discussed.

8.1   Analysis Setup

Firstly a brief description of the general data and method is reviewed here. The processing strategy adopted in this study mainly consists of three steps:

- Step 1 Correlation.
  The correlation of the reference quasar and the lunar lander observations were performed with DiFX-2.4.0 using a FFT resolution of 128 spectral channels per window (referred to Sec. 3.1 and Sec. 7.5).

- Step 2 Fring-fitting.
  The fringe-fitting (post-correlation) for determination of the multi-band group delays for the quasar and the lunar lander observations were performed separately. The lunar lander observations were fringe-fitted with the program *fourfit*-DOR. Besides that, only four frequency channels aiming at the corresponding four DOR tones without the carrier tone, were included in fringe-fitting process (referred to Sec. 4.2 and Sec. 7.4). For the quasar observations, the fringe-fitting was carried out with *fourfit* in a standard geodetic VLBI fringe-fitting analysis setup but with including only four frequency channels to be consistent with that of the lunar lander observations.

- Step 3 Parameter estimation.
  After the correlation and fringe-fitting, the group delays are obtained. As shown in Fig. 8.1, for the data analysis firstly the a priori information was setup in the control file, which contains the a priori coordinates of the Chang'E-3 lunar lander, EOP file and etc. Before loading the group delays, outlier tests and triangle closure delay analysis were performed to eliminate outliers. This step mainly consists of two parts (3a and 3b), one is with the quasar only observations and the other is with the lunar lander only observations. The data analysis pipeline is shown in Fig. 8.1.

  Step 3a Parameter estimation with delay referencing quasar observations.

  In the analysis, the reference quasar observations are used in a delay referencing way. The idea of delay referencing is to use the observations of quasars, which are nearby the lunar lander in an angular sense, to compute calibrations for the lunar lander observations. The total lunar lander delay will be composed of the initial lunar lander delay τ^{L} and a delay correction for the lunar lander $\Delta\tau^{\mathrm{L}}$

$$\tau^{\mathrm{L}}_{\mathrm{Correct}} = \tau^{\mathrm{L}} - \Delta\tau^{\mathrm{L}} \tag{8.1}$$

in which

$$\Delta\tau^{\mathrm{L}} = \Delta\tau_{\mathrm{Clock}} + \Delta\tau_{\mathrm{Atm,h}} + \Delta\tau_{\mathrm{Atm,w}} + \Delta\tau_{\mathrm{Ion}} \tag{8.2}$$

where τ_{Clock} is the clock contribution; $\Delta\tau_{\mathrm{Atm,h}}$ is the hydrostatic correction; $\Delta\tau_{\mathrm{Atm,w}}$ is wet component of the atmospheric corrections and $\Delta\tau_{\mathrm{Ion}}$ is the ionospheric corrections. The terms of clocks and

zenith wet delays are estimated from the delay referencing quasar observations. The term $\Delta\tau_{\text{Atm,h}}$ is the hydrostatic correction computed in typical way from the hydrostatic correction in zenith direction according to the modified Saastamoinen formula [Davis et al., 1985] for the epoch of the lunar observation instead of being estimated. The parameters of clocks and troposphere wet zenith delays are estimated as continuous piece-wise linear offsets in two-hour temporal resolution.

For the term $\Delta\tau_{\text{Atm,w}}$ of wet component of the atmospheric corrections, is computed as

$$\Delta\tau_{\text{Atm,w}} = \Delta\tau_{\text{Atm,w}}^{z} \cdot m_w(\varepsilon) \tag{8.3}$$

in which $m_w(\varepsilon)$ is the mapping function computed for the elevation of the lunar lander observation; $\Delta\tau_{\text{Atm,w}}^{z}$ is the zenith wet component of the atmospheric corrections at each station, can be computed from [Petit & Luzum, 2010]

$$\Delta\tau_{\text{Atm,w}}^{z}(t) = \frac{\Delta\tau_{\text{Atm,w}}^{z}(t_{n+1}) - \Delta\tau_{\text{Atm,w}}^{z}(t_n)}{t_{n+1} - t_n} \cdot (t - t_{n+1}) + \Delta\tau_{\text{Atm,w}}^{z}(t_{n+1}) \tag{8.4}$$

where t_n is the epoch before and t_{n+1} the epoch after the lunar lander observation. The zenith wet component is taken from the estimates of the reference delay quasar observations. The mapping function of the hydrostatic component $m_h(\varepsilon)$ is computed for the elevation of the lunar lander observation.

The contributions of clocks are obtained in the same way. The term of the clock contribution τ_{Clock} consists of the difference of the two clock offsets to be computed from the estimates according to Eq. 8.5.

$$\Delta\tau_{\text{Cl}}(t) = \tau_{\text{Cl}_b}(t) - \tau_{\text{Cl}_a}(t) \tag{8.5}$$

In the analysis, a reference station is chosen. Then the continuous piece-wise linear offsets of clocks, rate and quadratic terms of polynomials of clocks are estimated as parameters with the delay referencing quasar observations. With a number of tests, we verified that the quadratic terms of polynomials of clocks are close to insignificant level and clocks and the corresponding rates are enough for the further analysis.

As described in Sec. 3.2.2, the ionospheric corrections are computed from

$$\text{STEC} = \text{VTEC} * \text{M}(zd) \tag{8.6}$$

where STEC is the slant TEC values; VTEC is the vertical TEC values interpolated from the VTEC value in GIM file; M(zd) is the mapping function related to the zenith distance zd [Petit & Luzum, 2010].

Step 3b Parameter estimation with the lunar lander observations.

Besides these parameters from the estimation of the delay referencing quasar observations, the positions of the VLBI radio telescopes from the ITRF2014 solution [Altamimi et al., 2016] were used and transformed with standard correction models. The Earth Orientation Parameters (EOP) were extracted from the files (IERS 14 C04 time series [Bizouard & Gambis, 2018]) of the IERS Bulletin B. Including these parameters, the Earth-based parameters were fixed to their a priori values. The well-established models and correction models used and implemented in the program were referred to the modules and functions in the VieVs software [Böhm et al., 2012]. The models and functions related with the lunar lander observations were used and implemented according to the descriptions and discussions as above. After the lunar lander observations are calibrated, the position estimation of the Chang'E-3 lunar lander is performed with the lunar lander observations. The a priori coordinates of the Chang'E-3 lunar lander are used as constraint in the weighted least squares adjustment.
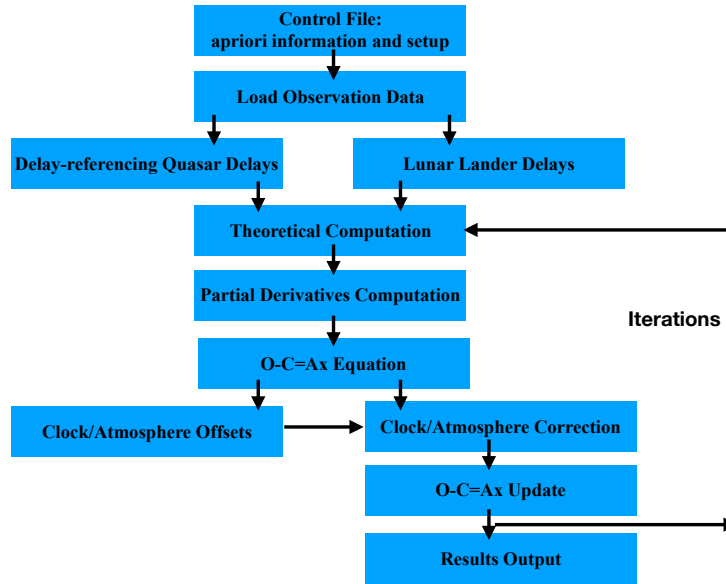
Figure 8.1: Data analysis program pipeline.

8.2 Results and Discussions

As we described the issues of the frequency setup in Sec. 6 and Sec. 6.2, a number of different setups were tested in observing the OCEL sessions. The twelve OCEL sessions could in general be sorted into two groups reflecting the different frequency setups. The first ten sessions form one group and the last two form the second group. The frequency setup for the first 10 sessions consists of three modes, one for the common geodetic quasar targets, one for the referencing quasar targets and one for the lunar lander. In the last two sessions, the frequency setup was unified to be the same for all targets.

In the approach used in this work, we only worked with delay referencing quasar observations. The common geodetic observations were not used, because they had an entirely different frequency setup which is prone to systematic deviations. Considering the station distribution, the number of observations and the geometry of the observations, OCEL-09 is representative among the twelve OCEL sessions. OCEL-09 consists of a greater number of stations participating and thus has the best measurement geometry. Besides that, the observations in OCEL-09 have a better quality than the other sessions. Therefore, the OCEL-09 session is selected to apply our models and concentrated our analysis on.

After the group delays were obtained from fringe-fitting, a data selection using a signal-to-noise ratio threshold was performed with the delay referencing quasar observations. The quasar observations, whose SNR was lower than 5, were eliminated. In general, there are 445 (out of 953) delay referencing quasar observations which could be used in the analysis. Then a parameter estimation with the quasar only observations were conducted as a first step. Fig. 8.2 illustrates the SNRs of the quasar observations used in the analysis. These SNRs are distributed in a number of blocks as the way the observations have been scheduled [Haas et al., 2016]. In the plot, the SNRs in the first few hours are higher than those in the last few hours. The main reason for the variations in SNR especially for the higher SNRs at the first two hours is that the radio sources observed during these two hours are generally stronger than those at the later part of the day. During these two hours, the source 0507+179 was used, and the other three sources used were 0515+208, 3C138 and 0600+177. The flux of quasar 0507+179 at X-band is about twice of that of the other three quasars.

In the middle part, there are no delay referencing quasar observations. The reason is that during these hours in the middle part, the lunar lander could not be observed on any baseline, and for this reason there were

no delay referencing quasar observations scheduled. Instead, standard geodetic quasar observations were scheduled. Since in our analysis the geodetic quasar observations are not used, there are no observations during these hours in the middle part.
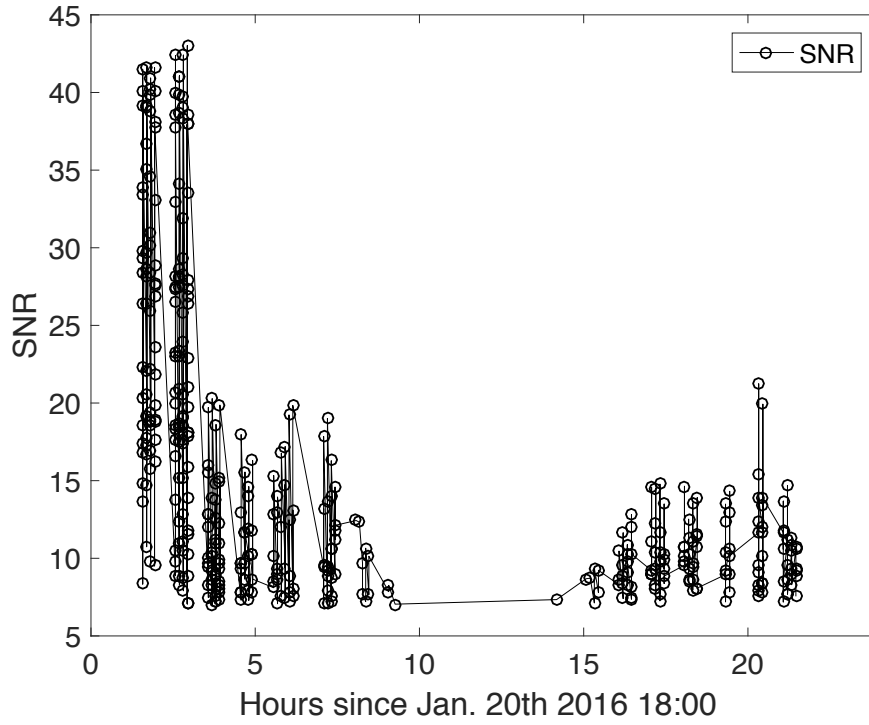

Figure 8.2: The SNRs of the quasar observations used for calibrations.

For the analysis of the delay referencing quasar observations, the standard geodetic VLBI analysis with a well-established modeling approach [Petit & Luzum, 2010] and weighted least squares adjustment is performed. The parameters of station clocks and troposphere were estimated as continuous piece-wise linear offsets in two-hour temporal resolution. In order to estimate clock offsets, a reference clock of a station has to be selected. In our analysis, the clock of the Badary station was chosen as the reference since it is the first station. The piece-wise linear offsets of clocks and rate terms of polynomials of clocks are the parameters to be estimated for clock part in the analysis with the delay referencing quasar observations. It should be noted that there are a number of obvious clock breaks, and for these we apply clock breaks offsets firstly before estimations. For the troposphere part, piece-wise linear offsets of zenith wet delay are the parameters to be estimated. As for troposphere gradients were fixed to the a priori values in the analysis. Besides that, other parameters such as, Earth orientation parameters, stations coordinates, source coordinates were not estimated but fixed to the a priori values. As for weights applied in weighted least squares adjustment, the weight matrix of observations is a diagonal matrix. In the diagonal matrix, the elements are one over the squared formal errors of the observations, formulated as

$$\boldsymbol{P} = diag\Big[\frac{1}{mi_{obs}^2}\Big] \tag{8.7}$$

where $\boldsymbol{P}$ is the weight matrix of observations; mi_{obs} is the formal errors of observations.

The post-fit residuals of the delay referencing quasar observations are shown in Fig. 8.3. The blue dots stand for the residuals and the corresponding error bars are shown in black. The observations clustering in blocks agree with the schedule. From the plot it could be found that there were more observations in the first few

hours than in the last ones. This is probably caused by the greater number of baselines at the beginning of the session.

The residuals are within the range of about tens of ps. The overall WRMS of the residuals is 35 ps. Given that the Chi-square is defined as the weighted residual sum of squares $\chi^2 = \boldsymbol{V}^T \boldsymbol{P} \boldsymbol{V} = \sum \frac{\Delta_j^2}{mi_j^2}$, in which Δ_j and mi_j are residual and corresponding uncertainty for observation j respectively. The Chi-square per degree of freedom (χ^2/v) is close to unity. The quality of the residuals indicates the accuracy of the analysis with only delay referencing quasar observations. According to the results and the accuracy of the lunar lander observations, the estimated calibration information from the analysis with only delay referencing quasar observations is enough for the subsequent position estimation of the lunar lander.
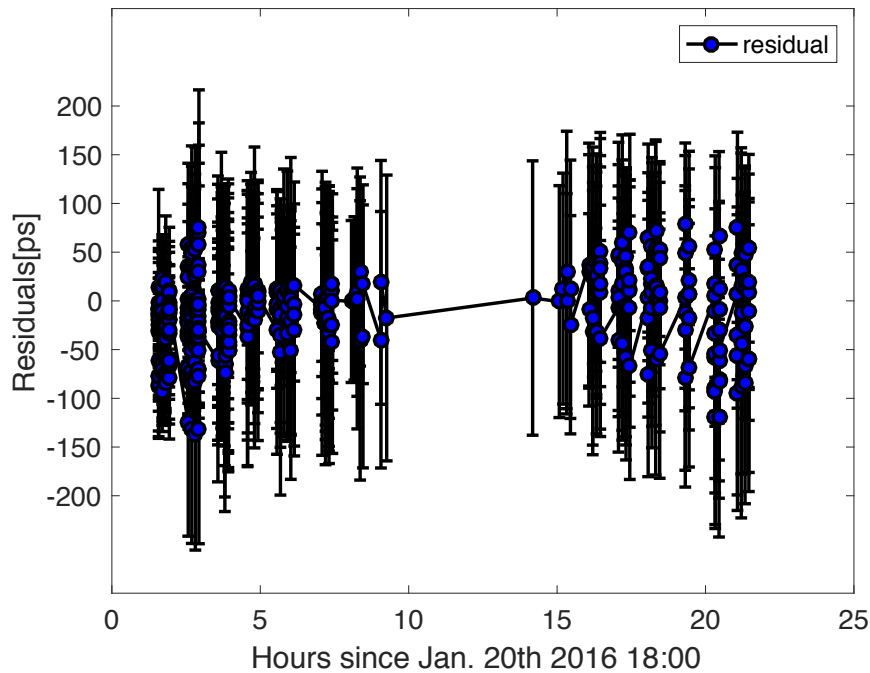
Figure 8.3: The post-fit residuals of the quasar observations. The residuals in blue are shown with 1-σ error bars in black.

After the analysis with only the delay referencing quasar observations, the analysis with only the lunar lander observations is performed. For the lunar lander observations, besides the SNR the data reduction is based on triangle closure delay tests. As for the triangle closure delay analysis, based on the investigations in Sec. 7, the observation blocks without obvious outliers have an average standard deviation of the triangle closure delays about 250 to 300 ps. With this value, we applied a 3σ limit and set 1 ns (a little bit larger than 3σ limit) as a boundary to select valid observations. The lunar lander observations involved in the triangle closure delays larger than the boundary value were eliminated.

As the a priori values, the Chang'E-3 lunar lander coordinates obtained by the Lunar Reconnaissance Orbiter (LRO) were used. The Lunar Reconnaissance Orbiter is a NASA robotic spacecraft currently orbiting the Moon in an eccentric polar mapping orbit, carrying the Lunar Reconnaissance Orbiter Camera (LROC), the Lunar Orbiter Laser Altimeter (LOLA) and other payload devices. The LROC system has a high resolution better than 50 cm, and LOLA has 5 m footprints and 10 cm vertical precision. The position estimates can be achieved with an accuracy of better than 20 m [Mazarico et al., 2012; LIU et al., 2015]. After the Chang'E-3 lunar lander landed on the Moon, LRO approached the landing site and LROC acquired a series of LROC Narrow Angle Camera (NAC) image pairs. By comparing the images of the

landing site before and after the landing, the LROC team confirmed the position of the lander and derived accurate map coordinates for the lander as listed in tab. 8.1.

Latitude	44.1214° N	0.00066°
Longitude	340.4884° E	0.00066°
Altitude	-2640 meters	-

Table 8.1: The coordinates of the Chang'E-3 lunar lander in Mean-Earth System by LRO. The rightmost column shows the uncertainties and the uncertainties of results by LRO are mainly based on the quoted accuracy of the technique.

After the analysis with only the delay referencing quasar observations, station clocks and tropospheric parameters were estimated. Then the estimated station clocks and tropospheric parameters were applied for the calibration followed by ionosphere corrections derived from TEC maps. A weighted least squares adjustment for the lunar lander observations was performed and the lunar lander position coordinates were estimated.

Based on the OCEL-09 observations and the approach presented above, the position of the Chang'E-3 lunar lander was estimated. The total number of the lunar lander observations obtained from fringe-fitting is 1184. After elimination of outliers and triangle closure delay analysis with a 3σ limit of 1 ns, the number of the remaining lunar lander observations is 688. With these observations and a fixed altitude constraint, the position was estimated to be 44.12188°N, 340.48822°E and -2640 meters (fixed) in the ME system with displacements of about 0.00021° in latitude and 0.00010° in longitude w.r.t the coordinates by LRO, translated to Cartesian coordinate corrections in the PA system w.r.t the LRO results of -12.0 m, -3.6 m and 10.4 m. In terms of 1-σ the corresponding uncertainties are 3.56 m, 1.65 m and 5.8 m in x, y, z of the PA system, respectively. The uncertainties were determined based on weighted least squares adjustment by the formulations as

$$m_i = m_0 \sqrt{\boldsymbol{N^{-1}}} \tag{8.8}$$

$$m_0 = \sqrt{\frac{\boldsymbol{V^T P V}}{n - t}} \tag{8.9}$$

$$\boldsymbol{N} = \boldsymbol{X^T P X} \tag{8.10}$$

where m_i is the uncertainty of the estimation; m_0 is the weighted root mean squared error; $\boldsymbol{P}$ is the weight matrix; $\boldsymbol{V^T P V}$ is the weighted residual sum of squares; n is the number of observations and t is the number of parameters to be estimated; X is design matrix.

The post-fit residuals of the position estimation of the OCEL-09 observations are shown in Fig. 8.4. Observations of more than twenty baselines were used in the analysis, which are distributed globally and form a reasonably good observing geometry. Although a large number of observations were conducted in the first half of the session, there are still about two hundred observations in the latter half for the analysis. So, in total, the observations used for analysis are well distributed in space and, over one day, in time. The WRMS of the post-fit residuals shown in Fig. 8.4 is 0.31 m (about 1 ns).

After the lunar lander landed on the Moon, there were a number of other efforts to determine its position by different means. This offers good opportunities to check and evaluate our position estimation results. The position determinations of the Chang'E-3 lunar lander by photographs are shown in tab. 8.2. As we described above, the quoted accuracy of LRO NAC is about 20 m in position determination, which
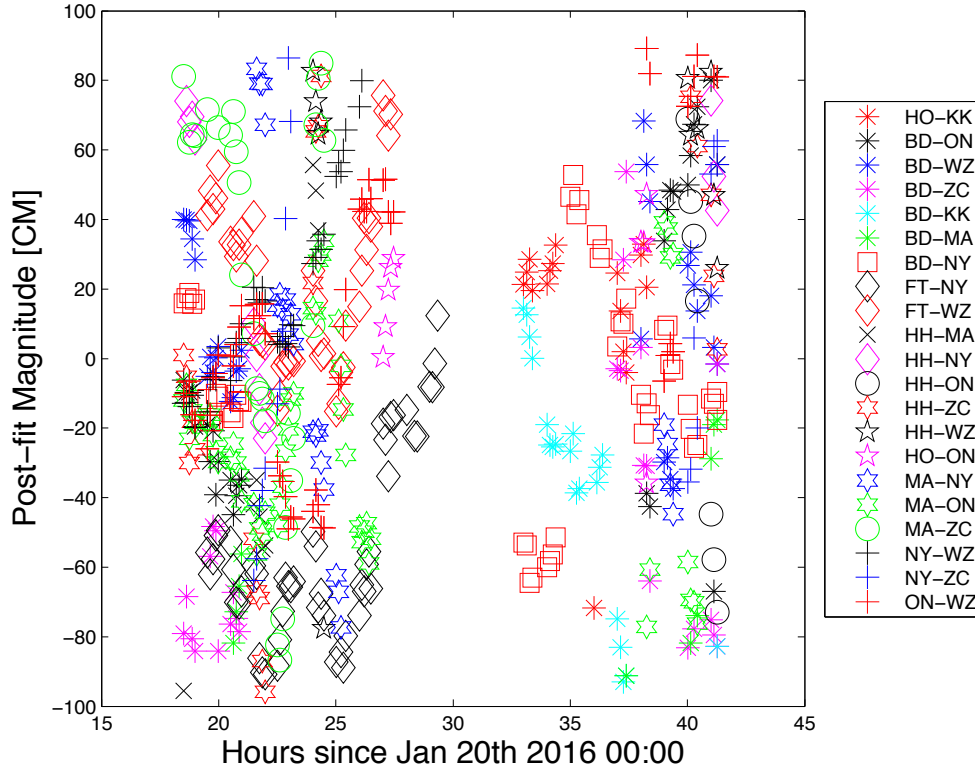
Figure 8.4: The post-fit residuals of the position estimation with OCEL-09.

is about 0.00066° in latitude and longitude on the lunar surface, and it could be slightly increased by stacking a number of photographs. Comparing our results with those from LRO based on the stacking of different numbers of photographs, we found differences in the range of 0.00002° to 0.0005° corresponding to about 0.6 m to 15 m on the lunar surface (tab. 8.2). This is just within the accuracy of the LRO position determinations.

Besides the position determinations by photographs, several VLBI measurements were conducted and used for estimation of the position of the Chang'E-3 lunar lander (tab. 8.3). On Dec. 14th and 17th 2014, two short-period (1 hour VLBI and 3 hour Unified X-band (UXB, range and range rate measurements)) experiments for observing the lunar lander were conducted with 6 Chinese station involved in VLBI and 3 Chinese stations involved in Unified X-band observations [Cao et al., 2016]. With the VLBI and UXB observations, the position of the Chang'E-3 lunar lander was estimated. The results differ from the coordinates determined by LRO by 0.0025° and 0.0023° and 2.4 m for the latitude, longitude and height, respectively.

The use of the UXB observations solved the problem of the weak sensitivity in radial direction of VLBI. However, a systematic offset in the UXB observations affected the accuracy of the position determination [Cao et al., 2016]. A similar analysis was performed in [Li et al., 2016], in which 2 hours of intensive VLBI observations and 1 hour of UXB observations with 3 stations were used and empirical systematic offsets were applied to the UXB observations. The position results of Li et al. [2016] differ from the coordinates determined from LRO by 0.0008° and 0.0008° and 8 m in latitude, longitude and height, respectively. The WRMS of the post-fit residuals of the VLBI observations in Cao et al. [2016] and Li et al. [2016] are about 0.3 m which is quite close to the WRMS above 0.31 m.

	Latitude(°)	Longitude(°)
LRO (1 photograph)	44.1214	-19.5116
(LRO team)	(0.00066)	(0.00066)
LRO (5 photograph)	44.1213	-19.5115
[LIU et al., 2015]	(0.00066)	(0.00066)
LRO (14 photograph)	44.1219	-19.5113
[LIU et al., 2015]	(0.00066)	(0.00066)
Our results	44.12188	-19.51178
	(0.00021)	(0.00010)

Table 8.2: Previous results of position determinations of the Chang'E-3 lunar lander by photograph. The numbers in brackets below the results are the corresponding $1 - \sigma$ uncertainties. The uncertainties of the results by LRO are mainly based on the quoted accuracy of the technique. The uncertainties of our results are translated from the uncertainties in Cartesian coordinates of the PA system.

In Klopotek et al. [2019], the same lunar lander group delays of OCEL-09 were used. Here, the geodetic quasar observations were used for the calibrations. The position of the lunar lander was estimated from that approach to be 44.12193°, -19.51159° and -2637.3 m. The differences between these and the coordinates by LRO are 0.00053°, 0.00001° and 2.7 m. Our results of position estimation of the Chang'E-3 lunar lander show differences of 0.00048° and 0.00018° w.r.t the coordinates by LRO.

All the OCEL sessions (except of 3 sessions without phase calibration applied) have observations with similar formal errors, station distributions etc. According to corresponding tests, the position estimation differences between them are within a range of about 10 to 20 m which agrees with the uncertainties. It should be noted that the coordinates determined by photographs from LRO are referred to the lander. The coordinates estimated from VLBI are referred to the antenna on the lander which emitted the signals. It can be seen in Fig. 9.2 that the antenna is at the side with a certain distance to the center of the lander. Besides that, the coordinates by LRO themselves have uncertainties of about 20 m. The results of the current study in terms of achieved accuracy are compatible with those of the other results related with the position of the Chang'E-3 lunar lander presented above.

At the same time, it can be found that there are significant improvements in the uncertainties of our results and those of Klopotek et al. [2019] w.r.t those in Cao et al. [2016] and [Li et al., 2016]. The main contributions come from the observing geometry and the observing arcs (or durations). In the OCEL sessions, the case of the 24 hours' duration for a single session with the global baselines of IVS provides long enough observing arcs and forms good observing geometry. The other results are only based on several hours' intensive VLBI and UXB observation with a smaller number of regional Chinese stations. On the other hand, the use of delay referencing quasar observations for calibrations also provides contributions to the improvements of the position estimations and corresponding uncertainties. There is still space to make further improvements by modifying the delay referencing with means of introducing dual-frequency observations, increasing the density of observations, and frequently switching between quasar and the lunar lander. Besides that, the modifications on the fringe-fitting of DOR tones signal and near-field delay model can also in some degree benefit for the improvement of total accuracy.

Each OCEL observing session produces a separate set of lunar lander coordinates. To increase the geometric stability, it has also been tested to combine observations from multiple sessions (e.g., OCEL-01, OCEL-05, OCEL-08 and OCEL-09) for estimating a single set of coordinates. The results were very close to those by a single session.

As reference, in a typical ΔDOR tracking in deep space navigation, the spacecraft and reference quasars are usually alternately observed for approximately one hour including 5 to 10 scans, each lasting 5 to 10minutes. Some sources of measurement errors can be reduced by making more intensive observations, using shorter

	Latitude(°)	Longitude(°)	Altitude(m)
VLBI+UXB	44.1189	-19.5093	-2637.6
[Cao et al., 2016]	(-)	(-)	(-)
VLBI+UXB	44.1206	-19.5124	-2632.0
[Li et al., 2016]	(-)	(-)	(-)
VLBI	44.12193	-19.51159	-2637.3
[Klopotek et al., 2019]	(0.00029)	(0.00015)	(-)
Our results	44.12188	-19.51178	-2640.0
	(0.00021)	(0.00010)	(-)

Table 8.3: Previous results of positioning of the Chang'E-3 lunar lander by VLBI. The numbers in brackets below the positioning results are corresponding quoted $1 - \sigma$ uncertainties. The uncertainties of our results are translated from the uncertainties in Cartesian coordinates of the PA system.

scans and by more frequent switching between spacecraft and quasar. However a slight improvement in the overall measurement accuracy can be obtained by increasing the observing duration beyond 1 hour or schedule more sessions in order to repeat the observations [Kinman, 2004].

In future investigation if considering to use current observing mode in OCEL to detect the lunar librations, we take the libration information from ephemeris for a general evaluation analysis. A widely-used ephemeris from JPL is DE421, which was released in 2008 [Folkner et al., 2008]. The DE430 was created in 2013 and is intended for use in modern data analysis. The lunar librations in the ephemeris are mainly calculated and fitted with LLR observations. For instance, LLR observations from the year of 1970 to 2007 were used for the computation of the lunar librations published in the JPL ephemeris DE421 and likewise form 1970 to 2012 for DE430. The libration information part of the JPL lunar ephemeris after DE430 are all based on DE430. Therefore, the librations after 2012 can only be obtained by extrapolations which would cause a loss in accuracy. The libration information is usually described by three Eular angles in ephemeris. Comparing the Euler angles from the DE421 and DE430 JPL ephemeris files, shifts of about 2 microradians occur as shown in Fig. 8.5 which could lead to a difference up to about 6 m on the lunar surface.
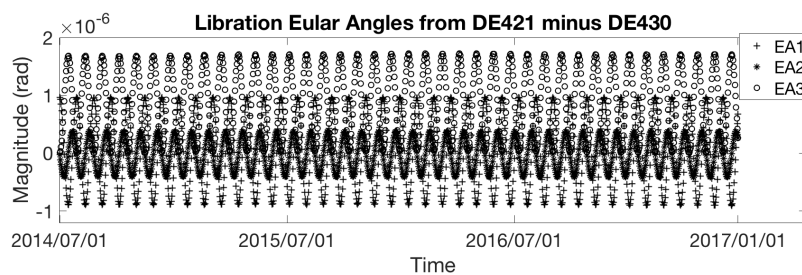
Figure 8.5: The differences of Eular angles between DE421 and DE430.

In order to perform analysis on the lunar librations with the OCEL sessions, besides to improve the total accuracy, it is suggested to schedule several sessions with a 14 to 15 days interval according to Fig. 8.5. Thus, corrections to the three Euler angles which describe the rotation of the Moon could possibly be estimated, especially the angle between the direction of the Moon center to the Equinox and the intersection line of the Moon equator and the Earth equator. Besides the Euler angles, the free libration parameters could be estimated. Combining the OCEL observations with LLR data will help to improve the estimates of all

libration parameters. With better libration modelling, all other parameters of interest such as the positions of the Chang'E-3 lander or lunar orbital parameters will also benefit.

9. Relative Position Estimation of two Transmitters on the Chang'E-3 Lunar Lander with Same Beam Interferometry

When two target sources are close enough together in an angular sense, they may be observed in the same antenna beam. Differential interferometric observables may be generated using simultaneous observations of the two target sources from two antennas. This technique, depicted in fig. 9.1 and known as same-beam interferometry (SBI), provides extremely accurate relative position measurements, as the atmosphere, ionosphere and adverse receiver effects can be removed almost entirely. The difference in time delay can be directly obtained with an accuracy of several picoseconds from the correlation phase [Liu et al., 2010]. The SBI technique is a derived case of differential VLBI, in which the angle from the Earth between two target sources is rather small to be observed in the same VLBI antenna beam.

SBI is used mostly in deep space navigation such as for several orbiting probes or a landing mission with a lander and rovers. In tracking Apollo 16 and 17, SBI was applied to multiple rovers and achieved a relative position determination accuracy of 25 meters [King Jr, 1975]. The Japanese lunar mission SELENE (Seleno-logical and Engineering Explorer) was conducted in 2007, in which a tracking system named multi-frequency same-beam differential VLBI was applied to observations between two sub-satellites. Besides Doppler measurements, the same-beam differential VLBI measurements contributed to the improvement of the final orbit consistency of the SELENE mission from several hundreds to several tens of meters [Liu et al., 2010]. In the Chang'E-3 mission, the relative position of the lunar lander and the rover was obtained with same beam VLBI measurements of the Chinese VLBI network [Liu et al., 2014].
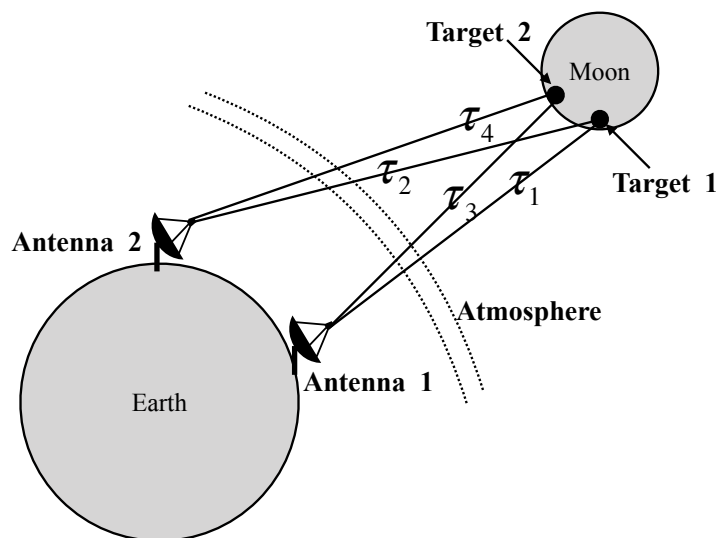
Figure 9.1: The geometry of same-beam interferometry.

The delay is mathematically equivalent to the time difference of the signal wavefront emitted by the target arriving at the two antennas on Earth. The SBI observable then is the delay difference between two targets. As shown in Fig. 9.1, the observable can be expressed by Eq. 9.1

$$\Delta\tau = (\tau_4 - \tau_3) - (\tau_2 - \tau_1) \tag{9.1}$$

This chapter describes the determination of the relative position of two transmitters on the Chang'E-3 lunar lander. A directional antenna and a TT&C (Telemetry, Tracking & Control) antenna are carried on the Chang'E-3 lunar lander as shown in Fig. 9.2. The directional antenna transmits the Data Communication signal and the TT&C antenna transmits the DOR signal at X-band. The frequency for the Data Communication signal is 8496 MHz, and the frequency of the DOR carrier is 8470 Mhz with 4 tones at ±3.85 MHz and ±19.25 MHz w.r.t the carrier frequency.
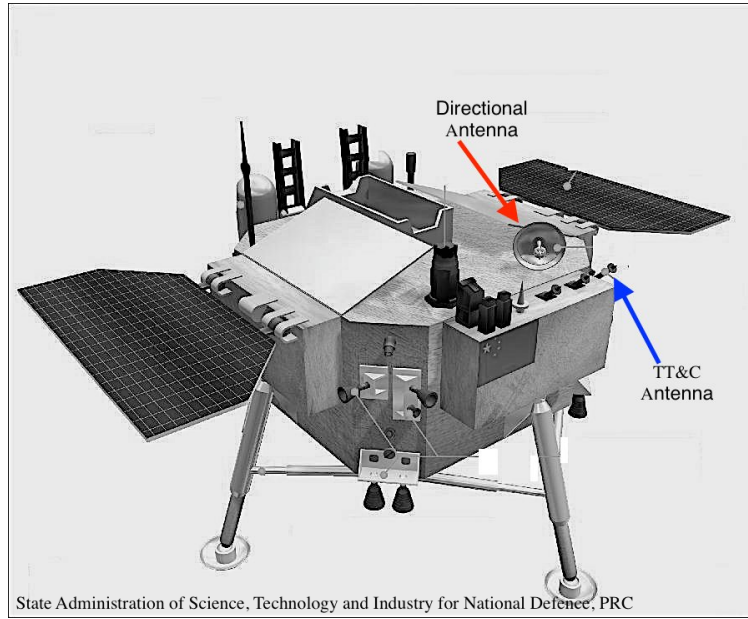
Figure 9.2: A schematic diagram of the Chang'E-3 lunar lander with two antennas labelled. The red arrow points to the directional antenna and the blue arrow points to the *TT&C* antenna.

9.1 Relative Position Measurement Model

To estimate the relative position between the directional antenna and the TT&C antenna, a relative position measurement model needs to be built up. Firstly, we simplify the geometry of the same-beam VLBI measurements, in which the observing antennas on Earth are labelled Antenna 1 and 2, and the antennas transmitting signal on the lunar lander are target 1 and 2 (Fig. 9.3). The distances from the target 1 to the two antennas are ρ_1 and ρ_2, and the distances from the target 2 to the two antennas are ρ_3 and ρ_4. According to Eq. 9.1, the observable can then be expressed as:

$$c\Delta\tau = (\rho_4 - \rho_3) - (\rho_2 - \rho_1) \tag{9.2}$$

where c is the speed of light. The delay of the observation is also subject to errors including clock errors, instrumental errors, atmosphere errors and random errors. Assuming that the sum of the impacts is τ_{error}, then Eq. 9.2 can be written as:

$$c\Delta\tau = (\rho_4 - \rho_3) - (\rho_2 - \rho_1) + (\Delta\tau_{error1} - \Delta\tau_{error2}) \tag{9.3}$$
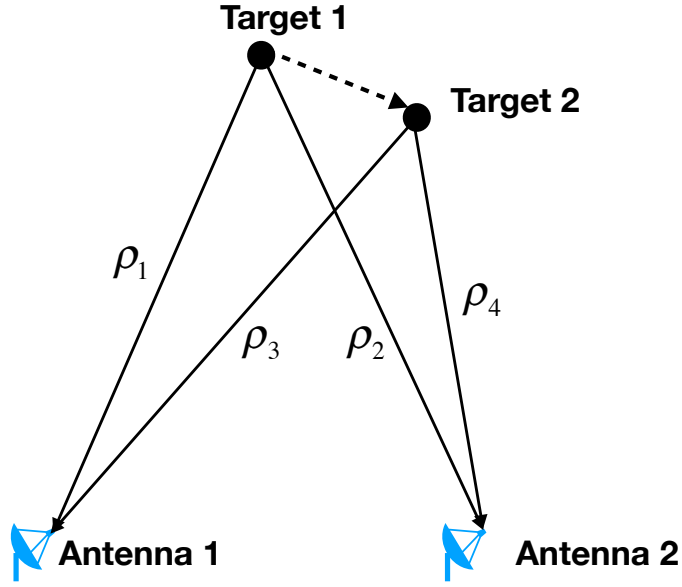
Figure 9.3: A schematic diagram of simplified geometry of the same-beam VLBI measurements.

Since ρ_1, ρ_2, ρ_3 and ρ_4 are the distances from the sources to each antenna, they can be expressed in BCRS as:

$$\rho_1 = \sqrt{(\boldsymbol{D}_1)^2}$$
$$\rho_2 = \sqrt{(\boldsymbol{D}_2)^2}$$
$$\rho_3 = \sqrt{(\boldsymbol{D}_3)^2} \tag{9.4}$$
$$\rho_4 = \sqrt{(\boldsymbol{D}_4)^2}$$

$$\begin{aligned}
\boldsymbol{D}_1 &= \boldsymbol{X}_{e1} - \boldsymbol{X}_1 \\
\boldsymbol{D}_2 &= \boldsymbol{X}_{e1} - \boldsymbol{X}_2 \\
\boldsymbol{D}_3 &= \boldsymbol{X}_{e2} - \boldsymbol{X}_1 \\
\boldsymbol{D}_4 &= \boldsymbol{X}_{e2} - \boldsymbol{X}_2
\end{aligned} \tag{9.5}$$

where X_{e1}, X_{e2}, X_1 and X_2, are the coordinate vectors of each source and each antenna, respectively, in BCRS. $\boldsymbol{D}_1$, $\boldsymbol{D}_2$, $\boldsymbol{D}_3$ and $\boldsymbol{D}_4$ are the vectors from each antenna to the respective source. The relative position vector from source 2 to source 1 is defined as:

$$\boldsymbol{X}_{e21} = \boldsymbol{X}_{e2} - \boldsymbol{X}_{e1} \tag{9.6}$$

According to the discussions in Sec. 5.2, the partial derivatives of the distances w.r.t the coordinate vector of the sources can be expressed as:

$$\frac{\partial \rho_1}{\partial \boldsymbol{X}_{e1}} = \frac{\boldsymbol{D}_1}{\rho_1}$$
$$\frac{\partial \rho_2}{\partial \boldsymbol{X}_{e1}} = \frac{\boldsymbol{D}_2}{\rho_2} \tag{9.7}$$

$$\frac{\partial \rho_3}{\partial \boldsymbol{X}_{e2}} = \frac{\boldsymbol{D}_3}{\rho_3}$$
$$\frac{\partial \rho_2}{\partial \boldsymbol{X}_{e2}} = \frac{\boldsymbol{D}_4}{\rho_4}$$
$$(9.8)$$

Then the partial derivatives of the distances w.r.t the relative position vector from source 2 to source 1 can be expressed as:

$$\frac{\partial (\rho_2 - \rho_1)}{\partial \boldsymbol{X}_{e21}} = \frac{\boldsymbol{D}_2}{\rho_2} - \frac{\boldsymbol{D}_1}{\rho_1}$$
$$\frac{\partial (\rho_4 - \rho_3)}{\partial \boldsymbol{X}_{e21}} = \frac{\boldsymbol{D}_4}{\rho_4} - \frac{\boldsymbol{D}_3}{\rho_3}$$
$$(9.9)$$

It should be noted that during the calculations, BCRS, GCRS, LCRS and the moon-fixed systems are involved, which are described in Sec. 2.2.

9.2 Determination of Relative Position between the Antennas on the Chang'E-3 Lunar Lander

In the Chang'E-3 mission, besides the lunar lander, a rover was placed on the surface of the Moon. The same-beam VLBI technique was used to observe the lander and the rover simultaneously and monitor the relative position between the lander and the rover with the differential phase delay by SBI. In the meantime, the SBI technique could also be applied to the directional communications and the TT&C antenna on the lander to obtain corresponding SBI observations.
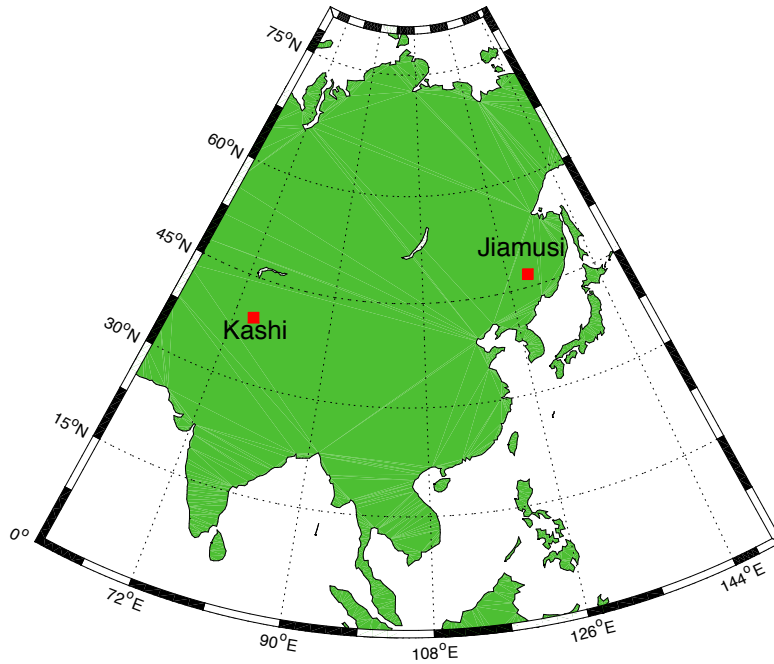
Figure 9.4: Geographical distribution of stations from the baseline of Jiamusi-Kashi.

From Jan. 28th to Feb. 1st, 2018, four experiments were conducted using the directional antenna and TT&C antenna on the baseline of Jiamusi-Kashi with same-beam VLBI. The geographical distribution of the stations

Jiamusi-Kashi is shown in Fig. 9.4. The Jiamusi station (66 meter antenna) in northeastern China and the Kashi station (35 meter antenna) in northwestern China are two deep space stations of the Chinese Deep Space Network (CDSN) which was designed and constructed to support China's Lunar Exploration Program (CLEP) [Ouyang et al., 2004]. The CDSN currently only includes three deep space stations, besides Jiamusi and Kashi, the third is the Zapala station (35 meter antenna) in Argentina [Zheng et al., 2008; Zhou et al., 2015]. The two stations started to be deployed in 2013 for the Chang'E-3 mission during the second stage of the CLEP and the Zapala station started from 2017 during the third stage of CLEP. The four SBI experiments were only conducted with the single baseline of Jiamusi-Kashi.

Useful observations could be taken from UTC 09:54:00 to 11:51:00 on Jan. 28th and from 10:54:00 to 12:07:00 on Jan. 29th, during which time there is an observation every second. The observations and the corresponding quality are discussed in detail below. Other data could not be used because some system and equipment problems occurred and led to the loss of data during the experiments. Especially, the data communication signal was heavily affected.

As we described in Sec. 3.7, there are four DOR tones at the frequencies of ± 3.85 MHz and ± 19.25 MHz w.r.t the carrier frequency at 8470 MHz. In the same-beam VLBI experiments, a 2 MHz bandwidth frequency channel aiming at the DOR tone of 19.25 MHz w.r.t the carrier frequency was used to receive the DOR signal from the TT&C antenna and the Data communication signal from the directional antenna was received with another 2 MHz bandwidth frequency channel aiming at 8496 MHz.

With the SBI technique, the signals from the two antennas on the lunar lander were received and recorded continuously at the same time. Then the data were correlated and fringe-fitted (with the typical means and tools used in deep space navigation in BACC) to obtain phase delay observables and differential phase delays. The basic idea of differential phase delay computation is:

$$\Delta \tau_{phase} = \tau_{phase}^2 - \tau_{phase}^1 \tag{9.10}$$

with

$$\tau_{phase}^1 = \frac{\phi_1}{2\pi f_1} \tag{9.11}$$

$$\tau_{phase}^2 = \frac{\phi_2}{2\pi f_2} \tag{9.12}$$

where τ_{phase}^1 and τ_{phase}^2 are the phase delays of the two antennas respectively; f_1 and f_2 are the frequencies received at the two antennas; ϕ_1 and ϕ_2 are the phases of the fringe frequency, respectively. Essentially, post-correlation involves extracting the phase as a function of time (phase tracking) to obtain the delay and delay rate observables.

In Fig. 9.5, the phase delays of the DOR signal from the TT&C antenna on the baseline Jiamusi-Kashi on Jan. 28th are shown, in which we can find two obvious jumps of the phase delays out of a smooth overall variation caused by the apparent rotations of this base vector. If we look into the observations, we find a data loss for a ten second period for each jump. These jumps actually represent ambiguities between the delays before and after the signal disruptions. The center frequency of the down-link signal is 8489.25 MHz and the corresponding ambiguity spacing of this frequency is 117.7 ps. The two sources are very close to each other (within 1 meter) having accurate enough a priori information of the sources and the antennas on the Earth, and differential VLBI reduces most of the systematic errors. Therefore, the variations in phase are relatively slow and the differential phase delay is accurate enough. Typically after obtaining the differential phase delay observations, about one-hour observation is enough for an accurate determination of the integer number of the ambiguities.

Besides the phase delays of the DOR signal, we obtained the corresponding phase delays of the Data communication signal shown in Fig. 9.6. We can also find the jumps of the phase delays by the ambiguities at the same epochs as the DOR signal, which agrees with the explanations above. However, the last part of the delays of the data communication signal are strongly corrupted and not usable. The overall scale of the phase delays of the DOR signal is within 1 ns and the short term variations of the phase delays are only within a
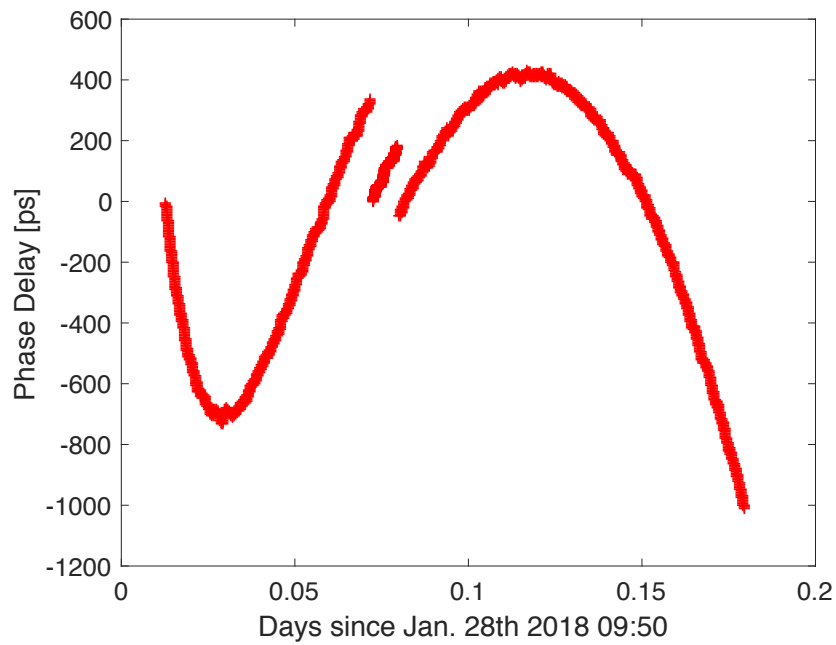
Figure 9.5: The phase delays of the baseline Jiamusi-Kashi receiving DOR signal from the *TT&C* antenna on Jan. 28th. The phase delay magnitude in y-axis is for convenience converted to time from the phase delay.
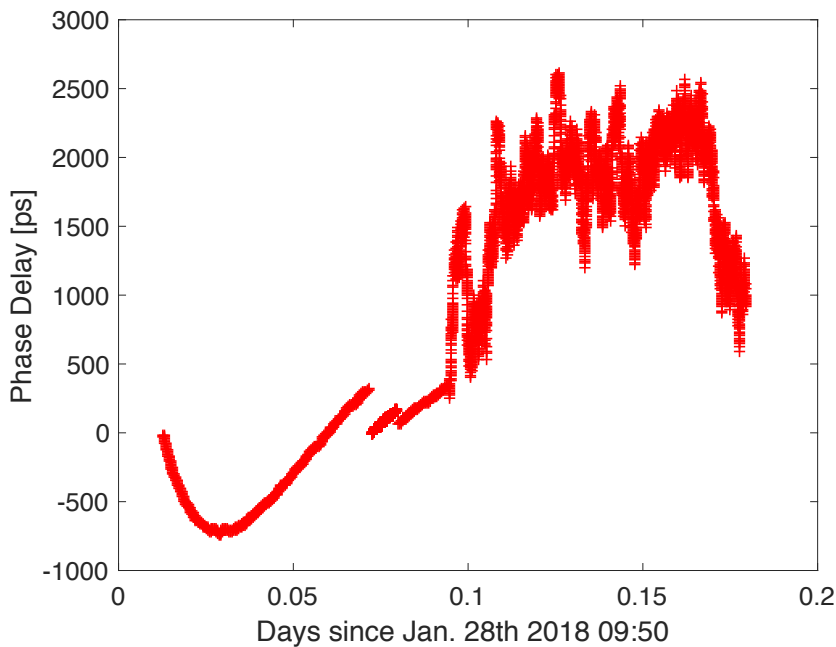

Figure 9.6: The phase delays of baseline Jiamusi-Kashi receiving Data communication signal from the directional antenna on Jan. 28th. The phase delays are converted to time delays for easier interpretation.

few tens of ps or below. As for the data communication signal, the phase delay variations at the beginning have a similar characteristics as that of the DOR signal, but the latter part is obviously corrupted and the variations of the phase delays are two orders of magnitude larger. For this reason, we did not consider these delays and consequently also the differential delays in the later analysis.
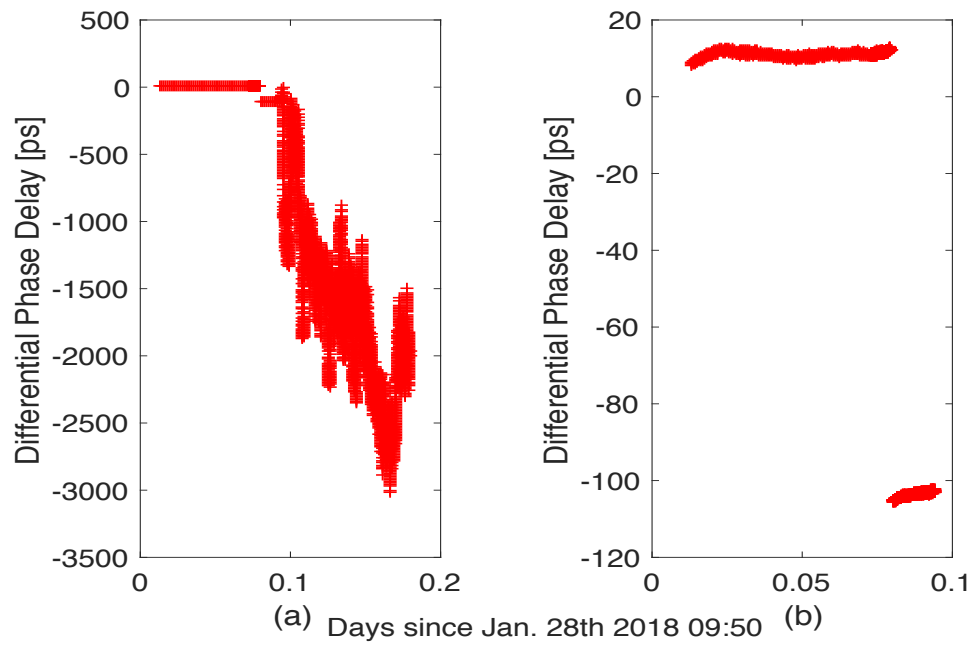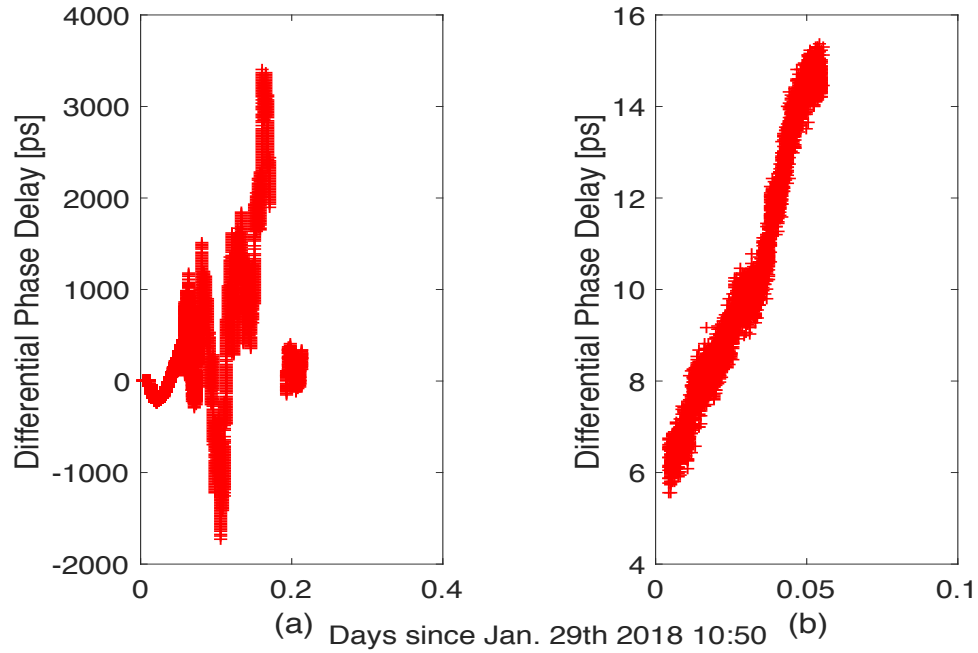
Figure 9.7: Differential phase delays between the directional antenna and the *TT&C* antenna on the baseline Jiamusi-Kashi on Jan. 28th. The differential phase delays are converted to time delays for easier interpretation. Plot (a) shows the overall differential phase delays; Plot (b) shows the usable differential phase delays.
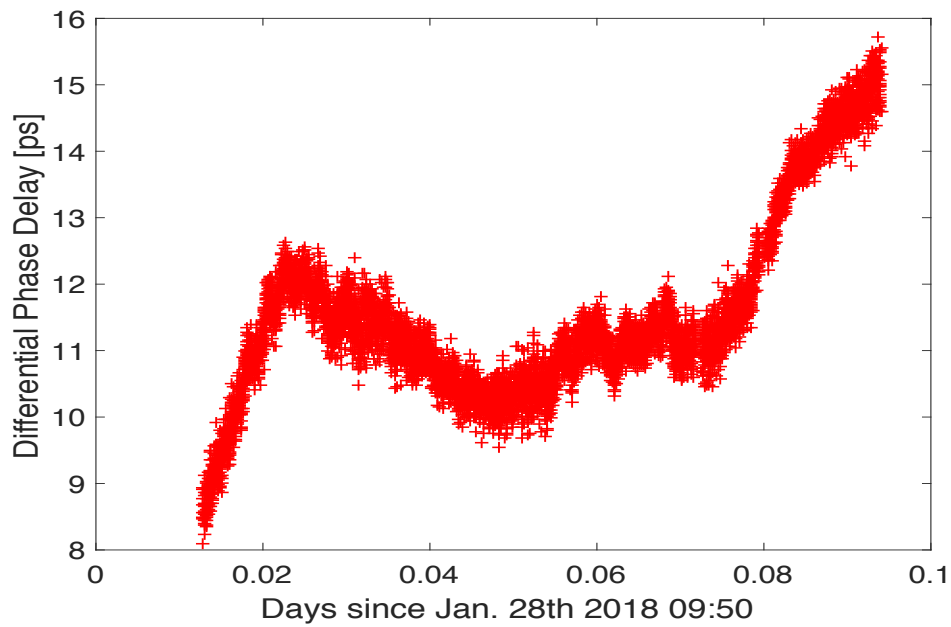
Figure 9.8: The differential phase delays with ambiguities resolved between the directional antenna and the *TT&C* antenna at the baseline of Jiamusi-Kashi on Jan. 28th. The differential phase delays are converted to time delays for easier interpretation.

In Fig. 9.7, plot (a) and (b) are the overall differential phase delays and the usable differential phase delays after eliminating the affected data. The corrupted delays of the data communication signal are reflected in the

differential phase delays in plot (a) and lead to differential phase delays which are two orders of magnitude larger. After elimination of the affected data and the data of the same epochs, we depict the differential phase delays in plot (b). Here, we see a jump caused by the ambiguities. With the ambiguities resolved, the differential phase delays are obtained for further analysis (Fig. 9.8). The overall scale of the differential phase delays is within ten ps. The random errors of the differential phase delays quoted by the data provider are at the level of about 0.2 ps.

As for the observations on Jan. 29th, the plot (a) and (b) in fig 9.9 are the overall phase delays from the two antennas respectively. Similar to the delays on Jan. 28th, the jumps of the phase delay led by ambiguities occur in both the DOR signal and the data communication signal. And the data communication signal was also badly affected and caused a partial corruption in the phase delay determination. The overall differential phase delays and the usable differential phase delays are shown as plot (a) and (b) respectively in fig 9.10. After data cleaning, in plot (b) the overall scale of the differential phase delays is similar to that of Jan. 28th.
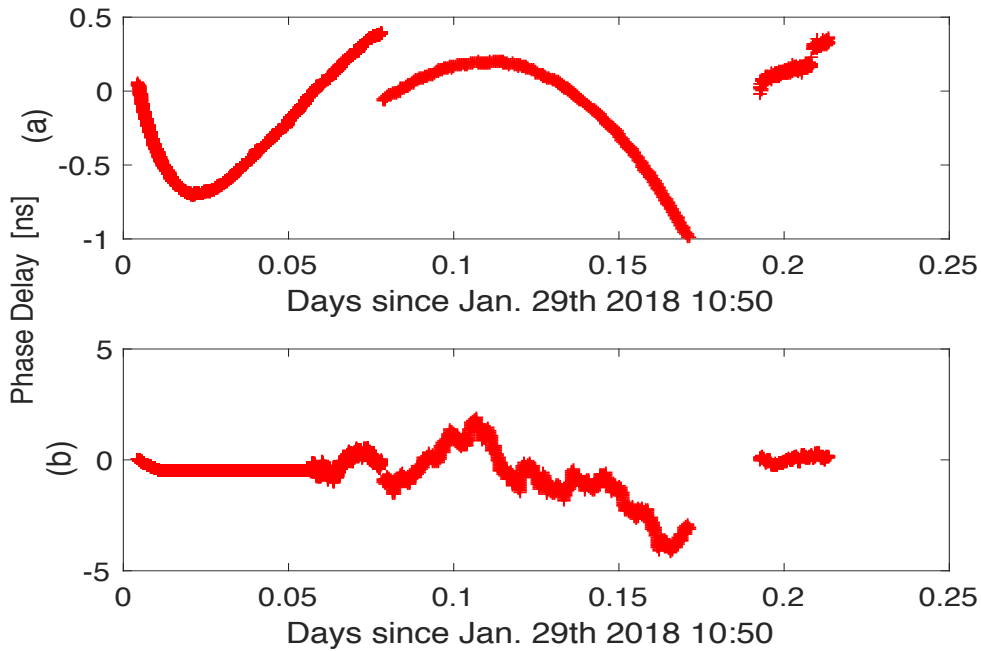
Figure 9.9: The phase delays of the baseline Jiamusi-Kashi on Jan. 29th. Plot (a) shows the overall phase delays receiving DOR signal from the $TT\&C$ antenna; Plot (b) shows the overall phase delays receiving Data communication signal from the directional antenna. The phase delays are converted to time delays for easier interpretation.

As the model built in Sec. 9.1, the differential phase delays between the directional antenna and the TT&C antenna, which are fixed on the lunar lander resulting in a fixed distance, are related to the relative position. With the differential phase delays we obtained above, the relative position between the two antennas can be estimated. From Eq. 9.1 to 9.9 the basis of relative positioning with SBI are shown. Then the parameters to be estimated are the vector between the position vectors of the two antennas in the Earth Centered Earth Fixed system (ECEF) as

$$\boldsymbol{R} = \boldsymbol{R}_t - \boldsymbol{R}_d \tag{9.13}$$

where $\boldsymbol{R}$ is the relative position vector in ECEF to be estimated; $\boldsymbol{R}_t$ and $\boldsymbol{R}_d$ are the position vectors in ECEF of two antennas respectively. The reason to use ECEF as the reference system is that the a priori

Figure 9.10: The differential phase delays between the directional antenna and the *TT&C* antenna at the baseline of Jiamusi-Kashi on Jan. 29th. Plot (a) shows the overall differential phase delays; Plot (b) shows the usable differential phase delays. The differential phase delays are converted to time delays for easier interpretation.

relative position vector was defined and measured in ECEF. Therefore, the relative position vector to be estimated is referred to ECEF as well. Then the observation equation can be expressed as

$$\Delta\tau = \boldsymbol{L}(\boldsymbol{R}) + \boldsymbol{\epsilon} \tag{9.14}$$

in which $\boldsymbol{R}$, $\Delta\tau$ and $\boldsymbol{\epsilon}$ are the relative position vector, differential phase delays and noises respectively. $\boldsymbol{L}(\boldsymbol{R})$ is a function related the differential phase delay and the relative position vector. After linearization, it is formulated as

$$\Delta\tau = \boldsymbol{H}\boldsymbol{R} + \boldsymbol{\epsilon} \tag{9.15}$$

where $\boldsymbol{H}$ is the design or Jacobi matrix containing the partial derivatives. Based on Eq. 9.9, the partial derivatives of the differential phase delay (translated to distance by multiplying by the speed of light c) w.r.t the relative position vector in ECEF can be written as

$$\frac{\partial(c\Delta\tau)}{\partial\boldsymbol{R}} = \frac{1}{\boldsymbol{M}_T}\left(\left(\frac{\boldsymbol{D}_4}{\rho_4} - \frac{\boldsymbol{D}_3}{\rho_3}\right) - \left(\frac{\boldsymbol{D}_2}{\rho_2} - \frac{\boldsymbol{D}_1}{\rho_1}\right)\right) \tag{9.16}$$

$$\boldsymbol{H} = \frac{1}{c}\frac{\partial(c\Delta\tau)}{\partial\boldsymbol{R}} \tag{9.17}$$

where $\boldsymbol{M}_T$ is the transformation matrix between BCRS and ECEF. The other variables are referred to in Fig. 9.3 and Sec. 9.1.

The a priori mechanical coordinates of the two antennas on the lunar lander, measured before the lander was sent to the Moon, and the relative position vector in ECEF compose the a priori values which are shown as V_0 in Tab. 9.1. The X, Y, and Z are Cartesian coordinates in ECEF. In the estimation, these serve as a priori coordinates.

	X (m)	Y (m)	Z (m)	Distance (m)	Post-fit STD (ps)
V_0	0.482	-0.248	-0.304	0.621	–
V_1	0.138	-0.380	-0.031	0.405	1.6
V_2	0.446	-0.284	-0.327	0.621	0.3

Table 9.1: The results of the relative position estimations with the differential phase delays by SBI.

The level of accuracy of the observations is quoted with 0.225 ps, which is close to the accuracy of the observations used in the relative positioning between the Chang'E-3 lunar lander and the rover [Liu et al., 2014].

In a first approach, we directly estimate the relative position vector X, Y, and Z in ECEF with the differential phase delays. The results of the least square adjustments are listed as V_1 in Tab. 9.1. The corresponding distance is computed from the relative position vector X, Y, and Z. In the estimation, the delays from the two days are used together, and the standard deviation of the overall post-fit differential phase delays is about 1.6 ps. Compared with the a priori relative position vectors and corresponding distance, there are significant differences of about 0.2 to 0.3 meters in X, Y, and Z. The corresponding computed relative distance differs from the a priori value by 0.216 meters.
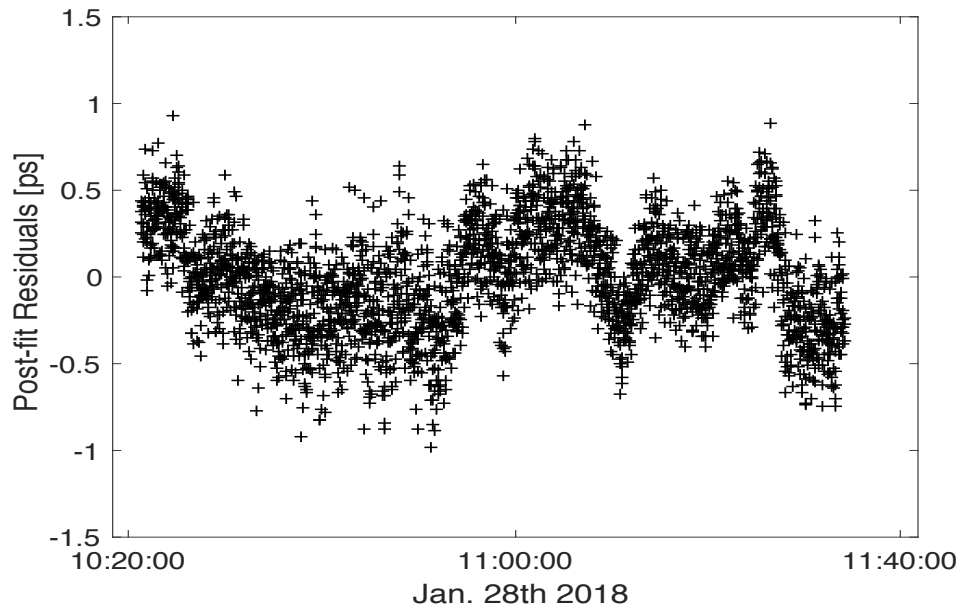
Figure 9.11: The post-fit residuals of the relative position estimation with distance constraint between the directional antenna and the $TT\&C$ antenna on the Chang'E-3 lunar lander with the differential phase delays on the baseline of Jiamusi-Kashi on Jan. 28th.

With the a priori relative position vector, we can apply constraints in the least squares adjustments to improve the stability of the estimation. Referred to the a priori value, the distance between the directional antenna and the TT&C antenna is fixed as a constraint. The constraint methods and corresponding equations as described in Sec. 5.3 are also suitable in this case. After linearizing the relationship, it is applied in the least squares adjustment. With the distance constraint, the estimations are performed for the relative position

vector starting with the a priori values of $V(0)$. The estimated results are listed as $V(2)$ in Tab. 9.1. The differences are about 0.02 to 0.04 meters in X, Y, and Z respectively, an order of magnitude smaller than those of the V_1 results without constraint. The post-fit residuals of the relative position estimation with distance constraint is shown in Fig. 9.11. The post-fit wrms scatter is about 0.3 ps, which is also an order of magnitude smaller than that in results of V_1 without constraint. However, there are remaining systematics on the order of about one picosecond of yet unknown origin.

In addition, the relative position vector between the two antennas in the PA system was estimated. By converting the relative position vector to spherical coordinates with polar angle (θ) and azimuth angle (ϕ), the relative angles between the two antennas in a Moon-fixed system PA are obtained. The relative angles in PA are estimated as -12.2° in θ and 139.1° in ϕ, with uncertainties about 0.62° and 0.41° respectively. The accuracy achieved in this analysis with SBI is compatible with that of the relative positioning between the lunar lander and the rover [Liu et al., 2014].

The good results show that the near field model developed for OCEL and the corresponding partial derivatives are also applicable to SBI. As a special case but essentially a VLBI technique, SBI is widely used in space exploration for relative position and orbit determinations. The work here can be used as a reference for further missions related to landing on the Moon. This will help to further increase the accuracy of relative position determinations between multiple targets.

10. VLBI vs. SBI

The Chang'E-3 lunar lander offers the opportunity for observing lunar targets with the VLBI technique. With the conduction of OCEL, a global VLBI Network was used for observing the lunar lander. At the same time it is also an attempt of using global geodetic VLBI observing an artificial target. In this work, we are dealing with the VLBI observations of the Chang'E-3 lunar lander, which are the VLBI observations from the OCEL sessions as well as same-beam interferometry observations with the Chinese deep space stations. The VLBI observations used in OCEL and in SBI are both originally referred to the classic geodetic VLBI technique, but in different ways and with different purposes. Here we talk about the features of VLBI and SBI especially in observing the lunar lander.

Differential one-way ranging (introduced in Sec. 3.7) as a VLBI technique is used in deep space tracking and observing artificial targets, specified in this work observing the lunar lander. For eliminating the errors by the influencing effects of clock, atmosphere and etc., ranking observations of spacecraft and quasars and using the quasar observations for calibrations is similar to Delta DOR. Furthermore, the same-beam interferometry is designed for measuring the relative positions of two spacecraft observed in the same beam. In SBI observations, two artificial targets are tracked simultaneously in the same beam and the final observable is the difference of the DOR measurements of two targets. These contain information on the relative position and its rate of change. Therefore, DOR, Delta-DOR and SBI are essentially VLBI techniques. SBI is a special case of Delta-DOR.

The necessary condition to apply the SBI technique is that two spacecraft targets should be close enough in an angular sense to be observed in the same beam-width of an Earth-based radio antenna. The systematic errors that scale with angular and temporal separations are greatly reduced, allowing to exploit the full precision of carrier-phase measurements. In SBI, the signals of the two spacecrafts targets are simultaneously received and recorded. Thus, simultaneous phase delay measurements are obtained and further on, the differences of these phase delay measurements are obtained. However, in Delta-DOR and the specific case of OCEL, the mode of SQS (or QSQ) is applied, in which observing is performed by switching between the spacecraft target and the reference quasar. The switching time between the spacecraft target and the reference quasar, which SBI does not have, may lead to errors in the observations. Therefore, the measurement accuracy of SBI is higher than that of delay-referencing (or phase-referencing) VLBI. The fundamental measurements of SBI are the same as those in VLBI, which are the phase of the VLBI fringe frequency, leading to the differential phase delay. It should be noted that in SBI to compute the phase differences of the fringe frequency, the phases of the two targets need to be converted to the same reference frequency (could be the signal frequency of one of the two targets) unless they are identical anyway.

In some cases, such as observing the targets on the lunar surface, a single-frequency signal with narrow bandwidth is used in SBI, such as in Sec. 9. Thus, the way to resolve the ambiguities in SBI is different. The approach to determine the group delays first and with them to resolve the ambiguities as for classic VLBI is not applicable. As for performing SBI observing the two targets on the lunar surface, the targets are respectively close and the signal is strong enough. Therefore, a duration of 1 to 2 hours' simultaneous observing is enough for resolving the integer number of ambiguities. After that, the relative position of the two targets on the lunar surface can be estimated. In the SELENE project, the resolution of ambiguities was introduced through multi-frequency observations, which is similar to the method we used in fringe-fitting the OCEL observations in Sec. 4.2.

Besides the observing mode and setup, also the target parameters of the data analyses are different. In the OCEL project, the observable calculated from fringe-fitting is the group delay of the lunar lander observations. With these group delays, the position of the lunar lander was estimated. In contrast to this, the observable used in Sec. 9 is the differential phase delay between two antennas of the lunar lander providing

relative position information. Geodetic VLBI with a large network had a good observing geometry with a global distribution of stations and long observing duration. SBI has the features of intensive observations, single baseline, short arcs and real-time. In deep space explorations and observing artificial targets with geodetic VLBI, this is usually used for position and orbit determinations. The SBI is applied for relative position and relative motion monitoring and combination with other measuring techniques.

The concept of differential tracking for angularly close sources is well established and has been applied in numerous missions and projects. It has also been proved in this work besides the position determinations of the lunar lander, the observing geometry with global stations distribution of the IVS network contributes to the improvement of position accuracy. SBI observations are used for relative position determinations. Both the observations of geodetic VLBI in OCEL and by SBI are in general VLBI observations of the Chang'E-3 lunar lander, but in different ways. With the explorations of the Moon and the development of VLBI, it is expected that the concept of OCEL and the SBI technique are combined in further investigations. They will be used to further study the Moon, for instance, on lunar librations and lunar reference frame realizations.

11. Conclusions and Outlook

This thesis is concerned with VLBI observations of the Chang'E-3 lunar lander. Besides the development of a chain of processing, the estimation of the position of the Chang'E-3 lunar lander and the relative position of two antennas on the Chang'E-3 lunar lander were performed with VLBI observations.

The Chang'E-3 lunar lander is equipped with an X-band transmitter enabling VLBI observations of the Moon from Earth. In a project called *Observing the Chang'E-3 Lunar Lander with VLBI* (OCEL), the lunar lander was observed with a globally distributed network of VLBI radio telescopes of the International VLBI Service for Geodesy and Astrometry (IVS). It opened a new window for applying geodetic VLBI to artificial radio sources. The main task of the OCEL study was separated in two parts, the determination of the group delays of the lunar lander observations and the position estimation of the lunar lander.

Starting the geodetic VLBI processing workflow with the determination of the group delays, investigations have been carried out to process Differential One-way Ranging (DOR) tones with an improved fringe fitting scheme. With these investigations, a complete chain of processing of the VLBI data for the OCEL sessions with proper methods were newly developed. The performance is assessed by triangle closure delay analysis as a main criterion. Thus, group delays of VLBI observations of DOR tones can now be obtained routinely which is the first achievement of this thesis.

The second part is the estimation of the position of the lunar lander with these group delays. New is that a near-field model was designed for VLBI delays of observations of the lunar lander and that the corresponding partial derivatives were derived and implemented. Compared with the most up-to-date near field model, the performance of our model is consistent at the picosecond level for the lunar lander. The position estimated with a constraint of the radial component is about 10 meters different from the values determined by the photogrammetric Lunar Reconnaissance Orbiter (LRO) mission. The results of the current study in terms of achieved accuracy are compatible with those of other recent results related the position of the Chang'E-3 lunar lander with VLBI. Besides that, due to the contribution coming from the globally distributed IVS network, respectively the long observing arc and delay referencing calibrations, the OCEL results show a better performance in terms of uncertainties compared to short-duration VLBI and VLBI plus range and range rate from Doppler measurements with a network of a few regional stations. In further investigations and more intensive scans, more frequently switching between delay referencing quasar and the lunar lander are expected. At the same time, modifications and refinements on fringe-fitting and near field model may be possible.

In 2018, a second beacon on the lander was switched on for a few hours and the lunar lander was observed again with the Chinese deep space network in same-beam VLBI mode. In a preliminary investigation, we used a number of these VLBI observations on the Jiamusi-Kashi baseline to estimate the relative position of the two antennas on the lunar lander. Differential phase delays were used as observables. The geometric delay model and the corresponding partial derivatives were derived and applied using the near field model developed for OCEL. The estimated relative position vector differs from the a priori vector by about 0.02 to 0.04 m. In addition, the relative angles (polar angle and azimuth angle) in a Moon-fixed system PA between the two antennas on the Chang'E-3 lunar lander are estimated. The accuracy achieved is compatible with the relative positioning between the lunar lander and the rover. The good results show that the near field model developed for OCEL and the corresponding partial derivatives are also applicable to SBI. As a special case but essentially a VLBI technique, SBI is widely used in space exploration for relative position and orbit determinations. The work here can be used as a reference for further missions related to landing on the Moon. This will help to further increase the accuracy of relative position determinations between multiple targets.

The Chang'E-3 lunar lander opened new a window for observing targets on the lunar surface with VLBI after those of the 1970s. The development of the VLBI technique and the global VLBI network of the IVS provided a good opportunity to conduct the OCEL project. The knowledge and experience gained will be of benefit for any follow-up projects and similar programs in the future. Continuation of this study will focus on

improving each step of the analysis in project OCEL but at the same time achieve further potential scientific goals, such as the motion of the Moon, the lunar librations, or the inner structure of the Moon. Using the phase delay as observable may be a way to improve the accuracy in subsequent studies. Referring to the well-established spacecraft tracking missions with ΔDOR, instead of to repeat genuine VLBI observations, it is expected to improve the overall accuracy of the results by employing intensive observations, use shorter scans and switch more frequently between spacecraft and quasars.

The demands on the radio telescopes will be challenging but they agree with the technical developments of geodetic VLBI towards the VLBI Global Observing System (VGOS). On the other hand, the investigations of same-beam VLBI observations of the Chang'E-3 lunar lander offered some clues for the use of differential phase delay and relative position determinations of multiple targets fixed on the Moon. With these, the lunar librations, the lunar structure and other lunar properties can be investigated by observing these targets on the Moon with VLBI in further scientific studies. Since more space exploration missions centered on the Moon and including several Moon landing projects are scheduled in the following years, many more scientific results will be achieved by observing multiple targets on the Moon with VLBI.

Abbreviations

Δ-DOR	Delta Differential One-way Ranging
ALSEP	Apollo Lunar Surface Experiment Package
BCRS	Barycentric Celestial Reference System
CLEP	Chinese Lunar Exploration Project
CODE	Center for Orbit Determination in Europe
CRF	Celestial Reference Frame
CRS	Celestial Reference System
CVN	Chinese VLBI Network
DiFX	Distributed FX
DOR	Differential One-way Ranging
DSN	Deep Space Network
EOP	Earth Orientation Parameters
ESA	European Space Agency
FFT	Fast Fourier Transformation
GCRS	Geocentric Celestial Reference System
IAG	International Association of Geodesy
IAU	International Astronomical Union
ICRF	International Celestial Reference Frame
ICRS	International Celestial Reference System
IERS	International Earth Rotation and Reference Systems Service
ITRF	International Terrestrial Reference Frame
ITRS	International Terrestrial Reference System
IVS	International VLBI Service for Geodesy and Astrometry
JPL	Jet Propulsion Laboratory
MPIfr	Max Planck Institute for Radio astronomy
ME	Mean Earth
NASA	National Aeronautics and Space Administration
NRAO	National Radio Astronomy Observatory
OCEL	Observing the Chang'E-3 Lunar Lander with VLBI
PA	Principal Axis
RLT	Relativistic Light Time
RF	Radio Frequency
RMS	Root Mean Square
SNR	Signal to Noise Ratio
TAI	International Atomic Time
TCB	Barycentric Coordinate Time
TCG	Geocentric Coordinate Time
TDB	Barycentric Dynamical Time
TEC	Total Electron Content
TRF	Terrestrial Reference Frame
TRS	Terrestrial Reference System
TT	Terrestrial Time
UTC	Coordinated Universal Time
UT	Universal Time
VEX	Venus Express
VGOS	VLBI Geodetic Observing System
VieVS	Vienna VLBI Software
WRMS	Weighted Root Mean Square

List of Figures

List of Tables

References

Alef, W. & Porcas, R. (1986). Vlbi fringe-fitting with antenna-based residuals. *Astronomy and Astrophysics*, 168, 365–368.

Altamimi, Z., Rebischung, P., Métivier, L., & Collilieux, X. (2016). Itrf2014: A new release of the international terrestrial reference frame modeling nonlinear station motions. *Journal of Geophysical Research: Solid Earth*, 121(8), 6109–6131.

Ash, M. E. (1972). *Determination of earth satellite orbits.* Technical report, Massachusetts Institute of Tech Lexington Lincoln LAB.

Bates, J. R., Lauderdale, W., & Kernaghan, H. (1979). Alsep termination report.

Berry, D. S. & Broder, J. S. (2005). Ccds concept paper: Delta-dor.

Bizouard, C. & Gambis, D. (2018). *International Earth Rotation and Reference Systems Service Earth Orientation Parameters EOP (IERS) 14 C04.*

Boehm, J. & Schuh, H. (2004). Vienna mapping functions in vlbi analyses. *Geophysical Research Letters*, 31(1).

Böhm, J., Böhm, S., Nilsson, T., Pany, A., Plank, L., Spicakova, H., Teke, K., & Schuh, H. (2012). The new vienna vlbi software vievs. In *Geodesy for Planet Earth* (pp. 1007–1011). Springer.

Böhm, J., Werl, B., & Schuh, H. (2006). Troposphere mapping functions for gps and vlbi from ecmwf operational analysis data. *J. Geophys. Res*, 111(B2), B02406–1.

BOOK, G. (2013). Delta-dor—technical characteristics and performance.

Border, J., Donivan, F., Finley, S., Hildebrand, C., Moultrie, B., & Skjerve, L. (1982). Determining spacecraft angular position with delta vlbi-the voyager demonstration. In *Astrodynamics Conference* (pp. 1471).

Bretagnon, P. & Brumberg, V. (2003). On transformation between international celestial and terrestrial reference systems. *Astronomy & Astrophysics*, 408(1), 387–400.

Brisken, W. (2013). Guide to the difx software correlator, version 2.2.

Brown, D., Hildebrand, C., & Skjerve, L. (1980). Wideband delta vlbi for deep space navigation. In *PLANS'80-Position Location and Navigation Symposium* (pp. 389–396).

Campbell, J. & Witte, B. (1978). Grundlage und geodätische anwendung der very long baseline interferometry (vlbi). *Zeitschrift für Vermessungwesen*, 103, 10–20.

Cannon, W. (1978). The classical analysis of the response of a long baseline radio interferometer. *Geophysical Journal International*, 53(3), 503–530.

Cao, J., Zhang, Y., Hu, S., Huang, Y., & Chen, M. (2016). An analysis of precise positioning and accuracy of the ce-3 lunar lander soft landing. *Geomat Inf Sci Wuhan Univ*, 41(2), 274.

Capitaine, N., Gambis, D., McCarthy, D., Petit, G., Ray, J., Richter, B., Rothacher, M., Standish, M., & Vondrak, J. (2002). Iers technical note, 29. In *Proceedings of the IERS Workshop on the Implementation of the New IAU Resolutions.*

Cappallo, R. (2017). *fourfit user's manual.* Technical report, Tech. rep., MIT Haystack Observatory (https://www. haystack. mit. edu/tech . . . .

Chapront, J. & Francou, G. (2006). Lunar laser ranging: measurements, analysis, and contribution to the reference systems. *The International Celestial Reference System and Frame*, (pp. $\tilde{9}$7).

Christophe, B., Andersen, P., Anderson, J., Asmar, S., Bério, P., Bertolami, O., Bingham, R., Bondu, F., Bouyer, P., Bremer, S., et al. (2009). Odyssey: a solar system mission. *Experimental Astronomy*, 23(2), 529–547.

Cotton, W. (1995). Fringe fitting. In *Very Long Baseline Interferometry and the VLBA*, volume 82 (pp. 189).

Counselman, C., Hinteregger, H., King, R., & Shapiro, I. (1973). Lunar baselines and libration from differential vlbi observations of alseps. *The moon*, 8(4), 484–489.

Counselman III, C. (1975). Precision selenodesy and lunar libration through vlbi observations of alseps.

Davidson, D. A. (1980). *A least squares adjustment for long baseline interferometry*. Department of Surveying Engineering, University of New Brunswick.

Davis, C. H. (1857). *Theory of the motion of the heavenly bodies moving about the sun in conic sections*.

Davis, J., Herring, T., Shapiro, I., Rogers, A., & Elgered, G. (1985). Geodesy by radio interferometry: Effects of atmospheric modeling errors on estimates of baseline length. *Radio science*, 20(6), 1593–1607.

Deller, A., Brisken, W., Phillips, C., Morgan, J., Alef, W., Cappallo, R., Middelberg, E., Romney, J., Rottmann, H., Tingay, S., et al. (2011). Difx-2: a more flexible, efficient, robust, and powerful software correlator. *Publications of the Astronomical Society of the Pacific*, 123(901), 275.

Deller, A. T., Tingay, S., Bailes, M., & West, C. (2007). Difx: a software correlator for very long baseline interferometry using multiprocessor computing environments. *Publications of the Astronomical Society of the Pacific*, 119(853), 318.

Duev, D. A., Calvés, G. M., Pogrebenko, S. V., Gurvits, L. I., Cimo, G., & Bahamon, T. B. (2012). Spacecraft vlbi and doppler tracking: algorithms and implementation. *Astronomy & Astrophysics*, 541, A43.

Dunnington, G. W., Gray, J., & Dohse, F.-E. (2004). *Carl Friedrich Gauss: titan of science*. MAA.

Eubanks, T. (1991). A consensus model for relativistic effects in geodetic vlbi. In *Proc. of the USNO workshop on Relativistic Models for Use in Space Geodesy* (pp. 60–82).

Folkner, W., Border, J., & Nandi, S. (1992a). Demonstration of orbit determination using same-beam interferometry for magellan and pioneer 12. In *Astrodynamics Conference* (pp. 4519).

Folkner, W., Engelhardt, D., Border, J., & Mottinger, N. (1992b). Orbit determination for magellan and pioneer 12 using same-beam interferometry. In *Astrodynamics 1991* (pp. 909–918).

Folkner, W. M., Border, J. S., Nandi, S., & Zukor, K. S. (1993). Precise tracking of the magellan and pioneer venus orbiters by same-beam interferometry. part 2: Orbit determination analysis.

Folkner, W. M., Williams, J. G., & Boggs, D. H. (2008). The planetary and lunar ephemeris de 421. *JPL IOM 343R-08-003*.

Fricke, W., Schwan, H., Lederle, T., Bastian, U., Bien, R., Burkhardt, G., Du Mont, B., Hering, R., Jährling, R., Jahreiß, H., et al. (1988). Fifth fundamental catalogue (fk5). part 1: The basic fundamental stars. *Veroeffentlichungen des Astronomischen Rechen-Instituts Heidelberg*, 32, 1–106.

Fukushima, T. (1994). Lunar vlbi observation model. *Astronomy and Astrophysics*, 291, 320–323.

Gauss, C. F. (1809). *Theoria motus corporum coelestium in sectionibus conicis solem ambientium*, volume 7. Perthes et Besser.

Godard, B., Budnik, F., Morley, T., & Lozano, A. L. (2012). Relativistic acceleration of planetary orbiters. In *Proceedings 23th International Symposium on Space Flight Dynamics–23th ISSFD, Pasadena, CA, USA*.

Goossens, S., Matsumoto, K., Liu, Q., Kikuchi, F., Sato, K., Hanada, H., Ishihara, Y., Noda, H., Kawano, N., Namiki, N., et al. (2011). Lunar gravity field determination using selene same-beam differential vlbi tracking data. *Journal of Geodesy*, 85(4), 205–228.

Haas, R., Halsig, S., Han, S., Iddink, A., Jaron, F., La Porta, L., Lovell, J., Neidhardt, A., Nothnagel, A., Plötz, C., et al. (2016). Observing the chang'e-3 lander with vlbi (ocel). In *First International Workshop on VLBI Observations of Near-field Targets* (pp. 41).

Han, S., Nothnagel, A., Zhang, Z., Haas, R., & Zhang, Q. (2019). Fringe fitting and group delay determination for geodetic vlbi observations of dor tones. *Advances in Space Research*, 63(5), 1754–1767.

Hellerschmied, A., McCallum, L., McCallum, J., Sun, J., Böhm, J., & Cao, J. (2018). Observing apod with the auscope vlbi array. *Sensors*, 18(5), 1587.

Hellings, R. (1986). Relativistic effects in astronomical timing measurements. *The Astronomical Journal*, 91, 650–659.

Hildebrand, C., Border, J., Donivan, F., Finley, S., Moultrie, B., Newhall, X., Skjerve, L., Yunck, T., Bletzacker, F., & Smith, C. (1982). Progress in the application of vlbi to interplanetary navigation. In *Very long baseline interferometry techniques* (pp. 55–72).

Huang, J., Ji, J., Ye, P., Wang, X., Yan, J., Meng, L., Wang, S., Li, C., Li, Y., Qiao, D., et al. (2013). The ginger-shaped asteroid 4179 toutatis: New observations from a successful flyby of chang'e-2. *Scientific reports*, 3, 3411.

Ip, W.-H., Yan, J., Li, C.-L., & Ouyang, Z.-Y. (2014). Preface: The chang'e-3 lander and rover mission to the moon. *Research in Astronomy and Astrophysics*, 14(12), 1511.

Jaron, F. & Nothnagel, A. (2019). Modeling the vlbi delay for earth satellites. *Journal of Geodesy*, 93(7), 953–961.

Jianguo, Y., Jinsong, P., Fei, L., Jianfeng, C., Qian, H., & Lihe, F. (2010). Chang'e-1 precision orbit determination and lunar gravity field solution. *Advances in Space Research*, 46(1), 50–57.

Kaula, W. M. (1963). Determination of the earth's gravitational field. *Reviews of Geophysics*, 1(4), 507–551.

Kikuchi, F., Kono, Y., Yoshikawa, M., Sekido, M., Ohnishi, M., Murata, Y., Ping, J., Liu, Q., Matsumoto, K., Asari, K., et al. (2004). Vlbi observation of narrow bandwidth signals from the spacecraft. *Earth, planets and space*, 56(11), 1041–1047.

King Jr, R. (1975). Precision selenodesy via differential very-long-baseline interferometry.

Kinman, P. (2004). Delta differential oneway ranging. *DSMS Telecommunications Link Design Handbook. California: JPL*, (pp. 19–24).

Klioner, S. A. (1991). General relativistic model of vlbi observables. In *Proc. AGU Chapman Conf. on Geodetic VLBI: Monitoring Global Change, Carter, WE (ed.), NOAA Technical Report*, number 137 (pp. 188–202).

Klioner, S. A. (2008). Relativistic scaling of astronomical quantities and the system of astronomical units. *Astronomy & Astrophysics*, 478(3), 951–958.

Klopotek, G., Hobiger, T., & Haas, R. (2017). Lunar observations and geodetic vlbi—a simulation study. In *Proceedings of the 23rd European VLBI group for Geodesy and Astrometry working meeting, Chalmers University of Technology, Gothenburg* (pp. 122–126).

Klopotek, G., Hobiger, T., Haas, R., Jaron, F., La Porta, L., Nothnagel, A., Zhang, Z., Han, S., Neidhardt, A., & Plötz, C. (2019). Position determination of the chang'e 3 lander with geodetic vlbi. *Earth, Planets and Space*, 71(1), 23.

Krarup, T. (1968). A framework for least-squares determination of the potential of the earth. *Report to the members of IAG Special Study Group*, 5, 31.

Krarup, T. (1969). A contribution to the mathematical foundation of physical geodesy. *Geod. Inst. Copenhagen, Medd., No. 44, 80 p.*, 44.

Langley, R. B. (1980). Precision geodesy and astrometry with a three station long baseline interferometer.

Lanyi, G., Border, J., Benson, J., Dhawan, V., Fomalont, E., Martin-Mur, T., McElrath, T., Romney, J., & Walker, C. (2005). Determination of angular separation between spacecraft and quasars with the very long baseline array. *The Interplanetary Network Progress Report*, 42, 162.

Li, C., Liu, J., Ren, X., Zuo, W., Tan, X., Wen, W., Li, H., Mu, L., Su, Y., Zhang, H., et al. (2015). The chang'e 3 mission overview. *Space Science Reviews*, 190(1-4), 85–101.

LI, J.-l., LIU, L., & QIAO, S.-b. (2011). Positioning analysis of observations from x-band monitoring and control system experiments in the chang'e-2 project [j]. *Journal of Geomatics Science and Technology*, 2.

Li, P., Hu, X., Huang, Y., Wang, G., Jiang, D., Zhang, X., Cao, J., & Xin, N. (2012). Orbit determination for chang'e-2 lunar probe and evaluation of lunar gravity models. *Science China Physics, Mechanics and Astronomy*, 55(3), 514–522.

Li, P., Huang, Y., Hu, X., & Shengqi, C. (2016). Positioning for the chang'e-3 lander and rover using earth-based observations. In *AGU Fall Meeting Abstracts.*

LIU, B., DI, K., WANG, B., TANG, G., XU, B., ZHANG, L., & LIU, Z. (2015). Positioning and precision validation of chang. *Chinese Science Bulletin*, 60(28-29), 2750–2757.

Liu, Q., Kikuchi, F., Matsumoto, K., Asari, K., Tsuruta, S., Ping, J., Hanada, H., & Kawano, N. (2007). Error analysis of same-beam differential vlbi technique using two selene satellites. *Advances in Space Research*, 40(1), 51–57.

Liu, Q., Kikuchi, F., Matsumoto, K., Goossens, S., Hanada, H., Harada, Y., Shi, X., Huang, Q., Ishikawa, T., Tsuruta, S., et al. (2010). Same-beam vlbi observations of selene for improving lunar gravity field model. *Radio Science*, 45(2).

Liu, Q., Koji, K., Fuyuhiko, P., Jinsong, A., Kazuyoshi Tsuruta, S., Hanada, H., & Kawano, N. (2006). Same-beam differential vlbi technology using two satellites of the selene spacecraft. *I Scientific Highlights*, (pp. 7).

Liu, Q., Zheng, X., Huang, Y., Li, P., He, Q., Wu, Y., Guo, L., & Tang, M. (2014). Monitoring motion and measuring relative position of the chang'e-3 rover. *Radio science*, 49(11), 1080–1086.

Lloyd, R. & Writer, C. I. S. (1999). Metric mishap caused loss of nasa orbiter. *CNN Interactive.*

Lohmar, F. J. (1985). Zur berechnung ionosphärischer refraktionskorrekturen für vlbi-beobachtungen aus simultanen dopplermessungen nach satelliten. *Mitteilungen Geod. Institut Rheinischen Friedrich-Wilhelms-Universitaets. Bonn*, 67.

Maddè, R., Morley, T., Abelló, R., Lanucara, M., Mercolino, M., Sessler, G., & de Vicente, J. (2006). Delta-dora new technique for esa's deep space navigation. *ESA bulletin*, 128, 68–74.

Mannucci, A., Wilson, B., Yuan, D., Ho, C., Lindqwister, U., & Runge, T. (1998). A global mapping technique for gps-derived ionospheric total electron content measurements. *Radio science*, 33(3), 565–582.

Marini, J. W. (1972). Correction of satellite tracking data for an arbitrary tropospheric profile. *Radio Science*, 7(2), 223–231.

Martín-Mur, T. J., Antreasian, P., Border, J., Benson, J., Dhawan, V., Fomalont, E., Graat, E., Jacobson, R., Lanyi, G., McElrath, T., et al. (2006). Use of very long baseline array interferometric data for spacecraft navigation.

Mazarico, E., Rowlands, D., Neumann, G., Smith, D., Torrence, M., Lemoine, F., & Zuber, M. (2012). Orbit determination of the lunar reconnaissance orbiter. *Journal of Geodesy*, 86(3), 193–207.

McCarthy, D. D. & Petit, G. (2004). *IERS conventions (2003).* Technical report, International Earth Rotation And Reference Systems Service (IERS)(Germany).

McCarthy, D. D. & Seidelmann, P. K. (2018). *Time: from Earth rotation to atomic physics.* Cambridge University Press.

Michelson, A. A. (1894). *On the application of interference methods to astronomical measurements*, volume 5. National Academy of Sciences.

Ming, C. & Qinghui, L. (2010). Study on differential phase delay closure of same-beam vlbi. In *2010 2nd International Conference on Computer Engineering and Technology*, volume 5 (pp. V5–88).: IEEE.

Moritz, H. (1970a). A generalized least-squares model. *Studia geophysica et geodaetica*, 14(4), 353–362.

Moritz, H. (1970b). *Least-squares estimation in physical geodesy.* Technical report, Ohio State University Columbus Department of Geodetic Science.

Moritz, H. (1972). *Advanced least-squares methods*, volume 175. Ohio State University Research Foundation.

Moyer, T. (2000). Formulation for observed and computed values of deep space network data types for navigation, monograph 2, deep space communications and navigation series. *Jet Propulsion Laboratory/California Institute of Technology.*

Moyer, T. D. (2005). *Formulation for observed and computed values of Deep Space Network data types for navigation*, volume 3. John Wiley & Sons.

Niell, A. (1996). Global mapping functions for the atmosphere delay at radio wavelengths. *Journal of Geophysical Research: Solid Earth*, 101(B2), 3227–3246.

Niell, A. (2000). Improved atmospheric mapping functions for vlbi and gps. *Earth, planets and space*, 52(10), 699–702.

Nothnagel, A. (2019). The correlation process in very long baseline interferometry. *GEM-International Journal on Geomathematics*, 10(1), 18.

Nothnagel, A., Artz, T., Behrend, D., & Malkin, Z. (2017). International vlbi service for geodesy and astrometry. *Journal of Geodesy*, 91(7), 711–721.

Oberg, J. (1999). Why the mars probe went off course. *IEEE Spectrum*, 36(12), 34–39.

Ouyang, Z. et al. (2004). Scientific objectives of chinese lunar exploration project and development strategy. *Advances in Earth Science*, 19(3), 351–358.

Ouyang, Z., Li, C., Zou, Y., Zhang, H., Lü, C., Liu, J., Liu, J., Zuo, W., Su, Y., Wen, W., et al. (2010). Primary scientific results of chang'e-1 lunar mission. *Science China Earth Sciences*, 53(11), 1565–1581.

Perkins, D. (1973). Alsep long term operational planning:(interim).

Petit, G., Boucher, C., & Lestrade, J.-F. (1989). First direct geodetic link between europe, africa and south america with a multi station vlbi array. *Bulletin géodésique*, 63(4), 331–341.

Petit, G. & Luzum, B. (2010). *IERS conventions (2010).* Technical report, BUREAU INTERNATIONAL DES POIDS ET MESURES SEVRES (FRANCE).

Petrov, L., Kovalev, Y., Fomalont, E., & Gordon, D. (2011). The very long baseline array galactic plane survey—vgaps. *The Astronomical Journal*, 142(2), 35.

Pieters, C., McCord, T. B., & Adams, J. B. (1976). Regional basalt types in the luna 24 landing area as derived from remote observations. *Geophysical Research Letters*, 3(11), 697–700.

Portock, B., Baird, D., Graat, E., Guinn, J., McElrath, T., Watkins, M., & Wawrzyniak, G. (2004). Mars exploration rovers cruise orbit determination. In *AIAA/AAS Astrodynamics Specialist Conference and Exhibit* (pp. 4981).

Potts, C., Raofi, B., & Kangas, J. (2004). Mars exploration rovers propulsive maneuver design. In *AIAA/AAS Astrodynamics Specialist Conference and Exhibit* (pp. 4985).

Rogers, A., Moffet, A., Backer, D., & Moran, J. (1984). Coherence limits in vlbi observations at 3-millimeter wavelength. *Radio Science*, 19(6), 1552–1560.

Rogers, A. E., Cappallo, R. J., Hinteregger, H. F., Levine, J. I., Nesman, E. F., Webber, J. C., Whitney, A. R., Clark, T. A., Ma, C., Ryan, J., et al. (1983). Very-long-baseline radio interferometry: The mark iii system for geodesy, astrometry, and aperture synthesis. *Science*, 219(4580), 51–54.

Saastamoinen, J. (1973). Contributions to the theory of atmospheric refraction. *Bulletin Géodésique (1946-1975)*, 107(1), 13–34.

Salzberg, I. (1973). Tracking the apollo lunar rover with interferometry techniques. *Proceedings of the IEEE*, 61(9), 1233–1236.

Sauser, B. J., Reilly, R. R., & Shenhar, A. J. (2009). Why projects fail? how contingency theory can provide new insights–a comparative analysis of nasa's mars climate orbiter loss. *International Journal of Project Management*, 27(7), 665–679.

Schaer, S. (1997). How to use code's global ionosphere maps. *Astronomical Institute, University of Berne*, (pp. 1–9).

Sekido, M. & Fukushima, T. (2006). A vlbi delay model for radio sources at a finite distance. *Journal of Geodesy*, 80(3), 137–149.

Shahid-Saless, B., Hellings, R. W., & Ashby, N. (1991). A picosecond accuracy relativistic vlbi model via fermi normal coordinates. *Geophysical Research Letters*, 18(6), 1139–1142.

Shambayati, S., Morabito, D., Border, J., Davarian, F., Lee, D., Mendoza, R., Britcliffe, M., & Weinreb, S. (2006). Mars reconnaissance orbiter ka-band (32 ghz) demonstration: cruise phase operations. In *SpaceOps 2006 Conference* (pp. 5786).

Shapiro, I., Robertson, D., Knight, C., Counselman, C., Rogers, A., Hinteregger, H., Lippincott, S., Whitney, A., Clark, T., Niell, A., et al. (1974). Transcontinental baselines and the rotation of the earth measured by radio interferometry. *Science*, 186(4167), 920–922.

Shapiro, I. I. (1976). 5.6. estimation of astrometric and geodetic parameters. In *Methods in Experimental Physics*, volume 12 (pp. 261–276). Elsevier.

Slade, M. A., Preston, R. A., Harris, A. W., Skjerve, L. J., & Spitzmesser, D. J. (1977). Alsep-quasar differential vlbi. *The moon*, 17(2), 133–147.

Smith, B. A., Soderblom, L. A., Johnson, T. V., Ingersoll, A. P., Collins, S. A., Shoemaker, E. M., Hunt, G., Masursky, H., Carr, M. H., Davies, M. E., et al. (1979). The jupiter system through the eyes of voyager 1. *Science*, 204(4396), 951–972.

Soffel, M., Klioner, S. A., Petit, G., Wolf, P., Kopeikin, S., Bretagnon, P., Brumberg, V., Capitaine, N., Damour, T., Fukushima, T., et al. (2003). The iau 2000 resolutions for astrometry, celestial mechanics, and metrology in the relativistic framework: explanatory supplement. *The Astronomical Journal*, 126(6), 2687.

Soffel, M., Müller, J., Wu, X., & Xu, C. (1991). Consistent relativistic vlbi theory with picosecond accuracy. In *International Astronomical Union Colloquium*, volume 127 (pp. 351–358).: Cambridge University Press.

Standish, E., Newhall, X., Williams, J., Yeomans, D., & Seidelmann, P. (1992). Explanatory supplement to the astronomical almanac. *PK Seidelmann, ed*, (pp. 279–323).

Sun, Z., Jia, Y., & Zhang, H. (2013). Technological advancements and promotion roles of chang'e-3 lunar probe mission. *Science China Technological Sciences*, 56(11), 2702–2708.

Svedhem, H., Titov, D., McCoy, D., Lebreton, J.-P., Barabash, S., Bertaux, J.-L., Drossart, P., Formisano, V., Häusler, B., Korablev, O., et al. (2007). Venus express—the first european mission to venus. *Planetary and Space Science*, 55(12), 1636–1652.

Takahashi, F. (2000). *Very long baseline interferometer*. IOS press.

Thompson, A. R. (1999). Fundamentals of radio interferometry. In *Synthesis Imaging in Radio Astronomy II*, volume 180 (pp. Ĩ1).

Thompson, A. R., Moran, J. M., Swenson, G. W., et al. (1986). *Interferometry and synthesis in radio astronomy*. Wiley New York et al.

Thornton, C. L. & Border, J. S. (2003). *Radiometric tracking techniques for deep-space navigation*. John Wiley & Sons.

Vanier, J. (1982). The active hydrogen maser: state of the art and forecast. *Metrologia*, 18(4), 173.

Vondrak, R., Keller, J., Chin, G., & Garvin, J. (2010). Lunar reconnaissance orbiter (lro): Observations for lunar exploration and science. *Space science reviews*, 150(1-4), 7–22.

Whitney, A. R. (2000). How do vlbi correlators work? In *International VLBI Service for Geodesy and Astrometry 2000 General Meeting Proceedings* (pp. 187–205).

Williams, J., Boggs, D., & Folkner, W. (2008). *DE421 lunar orbit, physical librations, and surface coordinates, JPL IOM 335-JW, DB*. Technical report, WF-20080314-001, March 14.

Xiao, L. (2014). China's touch on the moon. *Nature Geoscience*, 7(6), 391.

You, T.-H., Graat, E., Halsell, A., Highsmith, D., Long, S., Bhat, R., Demcak, S., Higa, E., Mottinger, N., & Jah, M. (2007). Mars reconnaissance orbiter interplanetary cruise navigation.

Zhao, J., Huang, J., Qiao, L., Xiao, Z., Huang, Q., Wang, J., He, Q., & Xiao, L. (2014). Geologic characteristics of the chang'e-3 exploration region. *Science China Physics, Mechanics and Astronomy*, 57(3), 569–576.

Zheng, Y., Ouyang, Z., Li, C., Liu, J., & Zou, Y. (2008). China's lunar exploration program: present and future. *Planetary and Space Science*, 56(7), 881–886.

Zhou, H., Li, H., & Dong, G. (2015). Relative position determination between chang'e-3 lander and rover using in-beam phase referencing. *Science China Information Sciences*, 58(9), 1–10.